AD NUMBER

ADB010287

LIMITATION CHANGES

TO:

Approved for public release; distribution is unlimited.

FROM:

Distribution authorized to U.S. Gov't. agencies only; Test and Evaluation; 11 NOV 1975. Other requests shall be referred to Naval Weapons Center, China Lake, CA.

AUTHORITY

usnwc ltr, 3 jul 1978

NWC TP 5788

An Analytical Study of a Boundary-Layer TVC Nozzle Concept

by
H. H. Tang, W. A. Anderson, and J. Xerikos
McDonnell Douglas Astronautics Company
for the
Propulsion Development Department

MARCH 1976

Naval Weapons Center
CHINA LAKE, CALIFORNIA 93555

Naval Weapons Center

AN ACTIVITY OF THE NAVAL MATERIAL COMMAND

R. G. Freeman, III, RAdm., USN . . . . . Commander

G. L. Hollingsworth . . . . . Technical Director

FOREWORD

This final report describes the analytical investigation of boundary-layer thrust vector control (BLTVC) technology. The work was conducted during the period 28 October 1974 through 28 July 1975 by the McDonnell Douglas Astronautics Company. The effort was sponsored by the Naval Weapons Center (NWC), China Lake, California, under Navy Contract N00123-75-C-0595 and supported by the Naval Air Systems Command under AirTask A3303300/008B/5F31330300.

Mr. M. D. Jacobson was the Navy Technical Coordinator and has reviewed this report for technical accuracy.

This report is released for information at the working level and does not necessarily reflect the views of NWC.

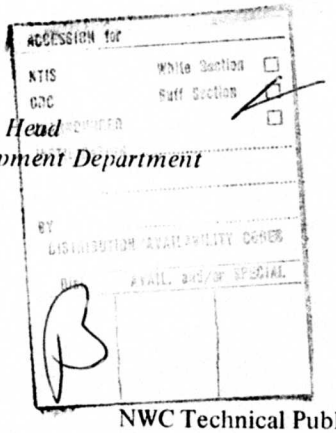

Released by
G. W. LEONARD, *Head*
Propulsion Development Department
15 March 1976

Under authority of
G. L. HOLLINGSWORTH
Technical Director

NWC Technical Publication 5788

Published by . . . . . Technical Information Department
Collation . . . . . Cover, 58 leaves
First printing . . . . . 200 unnumbered copies

UNCLASSIFIED

SECURITY CLASSIFICATION OF THIS PAGE *(When Data Entered)*

REPORT DOCUMENTATION PAGE

READ INSTRUCTIONS BEFORE COMPLETING FORM

1. REPORT NUMBER: NWC TP 5788
2. GOVT ACCESSION NO.:
3. RECIPIENT'S CATALOG NUMBER:
4. TITLE (and Subtitle): AN ANALYTICAL STUDY OF A BOUNDARY LAYER TVC NOZZLE CONCEPT
5. TYPE OF REPORT & PERIOD COVERED: FINAL rept. Oct [illegible] 1974-Nov [illegible] 1975
6. PERFORMING ORG. REPORT NUMBER: MDC-G6027
7. AUTHOR(s): H.H. Tang, W.A. Anderson and J. Xerikos
8. CONTRACT OR GRANT NUMBER(s): N00123-75-C-0595 NEW
9. PERFORMING ORGANIZATION NAME AND ADDRESS: McDonnell Douglas Astronautics Company, Huntington Beach, California 92647 — 389 310
10. PROGRAM ELEMENT, PROJECT, TASK AREA & WORK UNIT NUMBERS: AirTask A3303300/008B/5F31330300
11. CONTROLLING OFFICE NAME AND ADDRESS: Naval Weapons Center, China Lake, California 93555
12. REPORT DATE: MAR [illegible] 1976 — 117 p.
13. NUMBER OF PAGES: 114
14. MONITORING AGENCY NAME & ADDRESS *(if different from Controlling Office)*: A330-3300/008-B/5F31-3303-300
15. SECURITY CLASS. *(of this report)*: UNCLASSIFIED
15a. DECLASSIFICATION/DOWNGRADING SCHEDULE:
16. DISTRIBUTION STATEMENT *(of this Report)*: Distribution limited to U.S. Government agencies only; test and evaluation; 11 November 1975. Other requests for this document must be referred to the Naval Weapons Center.
17. DISTRIBUTION STATEMENT *(of the abstract entered in Block 20, if different from Report)*:
18. SUPPLEMENTARY NOTES:
19. KEY WORDS *(Continue on reverse side if necessary and identify by block number)*: BOUNDARY LAYER CONTROL; BOUNDARY LAYER SEPARATION; BOUNDARY LAYER THRUST VECTOR CONTROL; MISSILE STEERING; OVEREXPANDED NOZZLE
20. ABSTRACT *(Continue on reverse side if necessary and identify by block number)*:

See back of form.

DD FORM 1 JAN 73 1473/4 EDITION OF 1 NOV 65 IS OBSOLETE S/N 0102-014-6601

UNCLASSIFIED

SECURITY CLASSIFICATION OF THIS PAGE *(When Data Entered)*

389 310

(U) *An Analytical Study of a Boundary-Layer TVC Nozzle Concept,* by H.H. Tang, W.A. Anderson and J. Xerikos, McDonnell Douglas Astronautics Company. China Lake, Calif., Naval Weapons Center, March 1976, 114 pp. (NWC TP 5788, publication UNCLASSIFIED.)

(U) Experimental investigations of the feasibility of directing missile thrust by controlling ambient airflow through ports in overexpanded nozzles have been conducted by the Naval Weapons Center and an NWC-sponsored contractor, Chandler Evans, Inc. The present analytical effort studied boundary-layer thrust vector control (BLTVC) technology with the following specific objectives: (1) development of analytical or semi-empirical descriptions of the dominant phenomena that characterize the BLTVC flow field; (2) derivation of similarity parameters that affect BLTVC performance; (3) development of preliminary guidelines for flight-environment simulation with ground experiments; and (4) generation of design charts that would be useful for BLTVC performance evaluation. The results of the study include identification of areas that require investigation in order to establish a design suitable for mission applications.

1473-B

CONTENTS

NOMENCLATURE

A	Area or constant defined in Eq. 28
a	Sonic velocity
B	Constant defined in Eq. 29
C	Crocco number, $M/(\frac{2}{\gamma-1} + M^2)^{1/2}$
C_{pp}	Plateau pressure coefficient
C_{ps}	Separation-point pressure coefficient
c_p	Specific heat at constant pressure
erf η	Error function as defined in Eq. 37
F	Force
h	Enthalpy
I_1	Mass integral defined in Eq. 47
I_2	Momentum integral defined in Eq. 48
L	Separation-point distance measured from the nozzle throat
M	Mach number
M_o	Undisturbed Mach number before boundary-layer separation
$\dot{m}$	Mass flow rate
n	Velocity profile parameter (see Eq. 2)
p	Pressure
q_b	Heat transfer rate into the wall in the separated-flow region
R	Gas constant
R_{xo}	Reynolds number of the undisturbed flow before the separation point

T	Temperature
u, v	Velocities in x, y direction, respectively
V	Total velocity
X, Y	Coordinates of the reference system
x, y	Coordinates of the intrinsic system
o	Nozzle half-angle
α_e	Effective TVC deflection angle
β	Dummy variable associated with the error function
γ	Specific heat ratio
δ	Boundary layer thickness
δ_s	Height of the subsonic portion of the boundary layer
$\mathcal{E}$	Energy similarity parameter
ϵ	Nozzle expansion ratio, A/A*
η	Dimensionless coordinate, $\sigma y/x$
$\mathcal{H}$	Momentum similarity parameter
θ	Angle
θ_{12}	Prandtl-Meyer expansion angle
θ_{sh}	Shock angle
θ_s	Slip-line angle (Fig. 21)
Λ	Total enthalpy ratio of the jet, h_o/h_{oe}
λ	Molar specific heat ratio of the jet defined in Eq. 39 or $\lambda = \psi^{1/2}$ as defined following Eq. 7
$\mathcal{M}$	Mass similarity parameter
$\mathcal{M}$	Molecular weight
ν	Prandtl-Meyer angle
ξ	Dimensionless quantity, y/δ

ρ	Density
σ	Jet spreading parameter
τ	Shear stress
ϕ	Velocity ratio, u/u_c or u/u_e
ψ	Temperature ratio, T_w/T_e
Ω_c	Shear work and heat transfer across the mixing layer
Ω_d	Energy transfer by the entrained mass flow

Superscript

*	Sonic conditions

Subscripts

a	Attached side
b	Separated-flow region
c	Separated point
d	Reattaching streamline
e	Shear layer edge
g	Gas
j	Separating streamline or TVC gas
m	Coordinate shift in the mixing layer theory due to momentum conservation
o	Stagnation or undisturbed flow
p	Port side or particle
s	Subsonic portion of the boundary layer
w	Wall
x, y	Components in x and y directions, respectively
∞	Free stream

1, 2, 3, 4	At various cross sections (Fig. 21a)
2	Region after the oblique shock (Fig. 17)

INTRODUCTION

The Navy's off-axis attack missile concept, currently being developed by the Naval Weapons Center (NWC), China Lake, is directed toward a low-cost, high-density, maneuverable, air-to-ground weapon for attack aircraft with single-pass capability. Design-to-cost considerations dictate use of an inexpensive control system that is nonetheless capable of providing rapid response and high-incidence airframe maneuvers. These considerations have caused the Navy to investigate a boundary-layer thrust vector control (BLTVC) system.

The fundamental principle of BLTVC operation involves local modulation of the so-called "back pressure" about the flow-separation region in a highly overexpanded rocket exhaust nozzle. This modulation is done by selectively allowing inflow of ambient air into the back-pressure region, which in the unperturbed state is at low pressure because of viscous pumping. Natural, unforced flow of ambient-pressure air through control ports into the back-pressure region causes the separated, supersonic rocket exhaust flow to reattach to the nozzle on the side opposite controlled inflow. Since the reattached flow thence follows only a portion of the nozzle wall, the rocket exhaust can be vectored at an angle that approaches the nozzle half-angle, thus providing a side force consistent with the lateral exhaust momentum (also manifested as an asymmetrical nozzle pressure distribution). Recent Navy-funded work by Chandler Evans, Inc. (Ref. 1 and 2) has resulted in development of a viable BLTVC hardware concept. The phenomenology of this concept has been variously called fluidics, boundary-layer control, and the Coanda effect since about 1930. References 3, 4, and 5 are indicative of the historical background available.

Although analytical studies in related technology areas have been conducted by McDonnell Douglas Astronautics Company (MDAC) and others, no theoretical studies before the present one have directly addressed the evaluation of BLTVC performance. The successful conduct of such a study offered the twofold advantage of providing information for predicting system performance and also of providing a basis for critical evaluation of experimental programs. With these considerations in mind, the present study encompassed the following objectives: (1) development of analytical or semiempirical descriptions of the dominant phneomena that characterize the thrust vector control (TVC) flow field, (2) derivation of similarity parameters that affect TVC nozzle performance, (3) development of preliminary guidelines for flight-environment simulation with ground experiments, and (4) generation of design charts for use in TVC performance evaluation.

This report discusses overall flow-field conditions, presents most of the analyses of flow-field modeling, and gives computational results. BLTVC similarity and scaling studies are described; guidelines are given for nozzle-design matters such as port location and size, nozzle expansion ratio, and chamber-pressure range; and conclusions and recommendations are summarized.

It should be noted that this study used results of cold-flow and static rocket tests exclusively. These tests were conducted in a quiescent environment, and caution should therefore be exercised regarding the applicability of these data for direct evaluation of flight performance without consideration of the flow phenomena that are peculiar to BLTVC operating environments.

FLOW-FIELD CONDITIONS

To date, all BLTVC cold-flow and rocket tests have been conducted without ambient flow external to the nozzle. The difference in BLTVC performance between a cold-flow or rocket static test and a wind-tunnel or flight test may be very significant because of the presence of the ambient flow. As shown schematically in Fig. 1, the main difference between a BLTVC nozzle with and without ambient flow is the interacting flow field, which involves a two-stream jet-mixing process.

BLTVC IN A QUIESCENT EXTERNAL ENVIRONMENT

For BLTVC nozzles without external ambient flow, the injection mass does not interact strongly with the nozzle main flow in a conventional sense. However, it does trigger the highly unstable separated main flow of an overexpanded nozzle to attach on the side opposite the injection ports. This main-flow attachment process appears to do two things: (1) it provides an ejector-type action that carries the injection mass out of the nozzle adjacent to the affected boundary, and (2) it creates a large volume in the aft ends of the port sides. Consequently, a significant feedback of the ambient air into the inside rear surface on the nozzle port side occurs, and the port-side pressure approaches the ambient pressure level, p_∞, very rapidly.

The cylindrical section of the nozzle shown in Fig. 1 assists in the attachment process. The pressure is lower on the attached side when the flow does reattach. Without reattachment, the pressure, influenced by the ambient-flow feedback, rises more rapidly, and this reduces the attainable side-force level. Furthermore, hysteresis may occur in the side force during the cycle of rising and falling chamber pressure, as shown in Fig. 2. This happens because flow attachment does not occur at the same p_{oc} value when chamber pressure increases and decreases. Recent cold-flow tests employed a longer, cylindrical aft section that eliminated the hysteresis loop by minimizing the ambient-flow feedback effect. Typical results are shown later in Fig. 34.

BLTVC WITH EXTERNAL AMBIENT FLOW

For TVC nozzles that operate with external ambient flow, the mechanism that triggers the main-flow attachment process is strongly influenced by the free shear layer formed by the ambient flow. This free shear layer interacts with the free shear layer along the boundary of the main flow and causes a two-stream mixing process, as shown

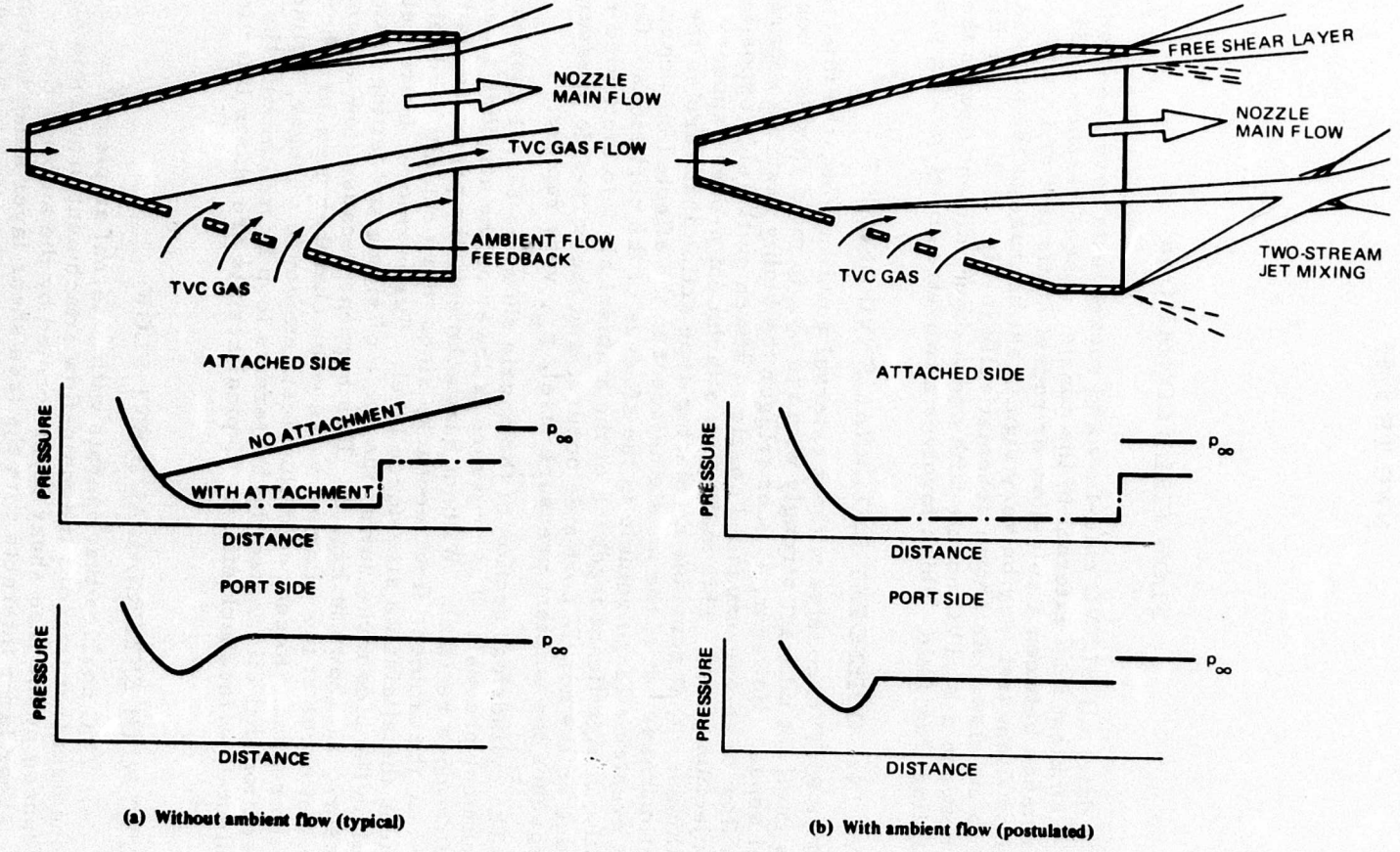

NWC TP 5788

FIG. 1. Flow Field Conditions for BLTVC Nozzle With and Without External Ambient Flow.

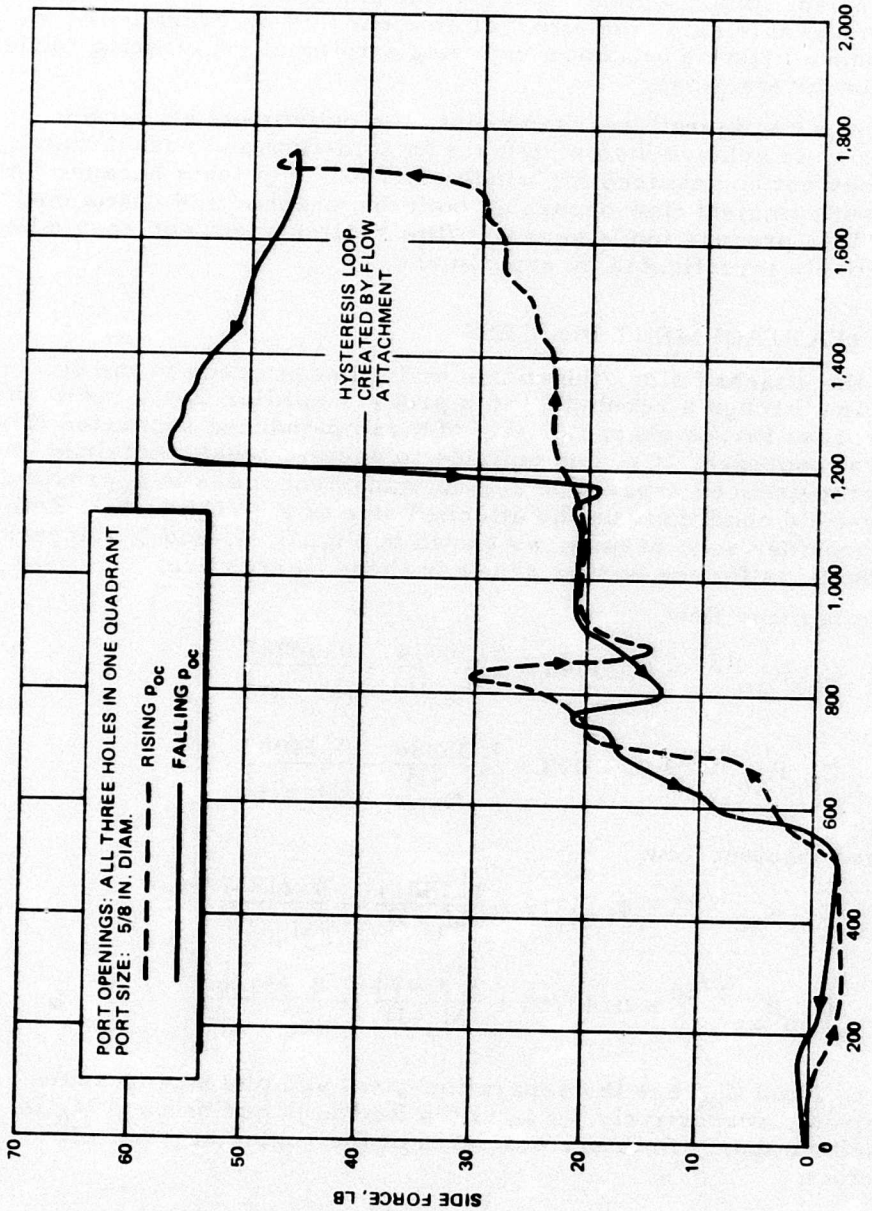

FIG. 2. Hysteresis Loop Observed in Cold-Flow Tests.

in Fig. 1. The injection mass affects the flow-field conditions in the region bounded by the two free shear layers and the inside surface of the port side. Therefore, there is no direct ambient-flow feedback, and the pressures on the port side are more uniform throughout the entire region. Since no tests that include ambient-flow simulation have been conducted to date, the effect of ambient flow on overall BLTVC performance must be estimated by using a rational engineering model of the flow interactions.

From a configurational standpoint, the cylindrical aft section, which helps to achieve high side force in cold-flow and rocket static tests, may not be required for wind-tunnel or flight tests because jet mixing with ambient flow occurs on both the attached and unattached sides. This process tends to assist flow reattachment and should be quantitatively investigated by experiment.

FLOW-REATTACHMENT PROCESS

On the attached side, the nozzle main flow attaches to the cylindrical section through a recompression process similar to the reattachment process that is characteristic of a ramp-induced separated flow. As a first approach, it seems suitable to use the results obtained in some ramp-induced separation and reattachment cases to approximate the flow-field conditions on the attached side of a TVC nozzle. Reference 6 provides such results, as shown in Fig. 3, 4, and 5. Approximate equations for the curves shown in these figures are:

For laminar flow,

$$C_{ps}R_{xo}^{1/4} = 0.20993 + \frac{0.55034}{(M_o-1)} - \frac{0.06027}{(M_o-1)^2}$$

$$C_{pp}R_{xo}^{1/4} = 0.37098 + \frac{1.03886}{(M_o-1)} - \frac{0.14985}{(M_o-1)^2}$$

For turbulent flow,

$$C_{ps}R_{xo}^{1/10} = 0.10912 + \frac{1.18214}{(M_o-1)} - \frac{0.21857}{(M_o-1)^2}$$

$$C_{pp}R_{xo}^{1/10} = 0.42755 + \frac{1.33474}{(M_o-1)} - \frac{0.35426}{(M_o-1)^2}$$

where C_{ps} and C_{pp} are the separation-point and plateau-pressure coefficients, respectively. R_{xo} is the Reynolds number and M_o is the Mach number. Both are evaluated at the beginning point of interaction.

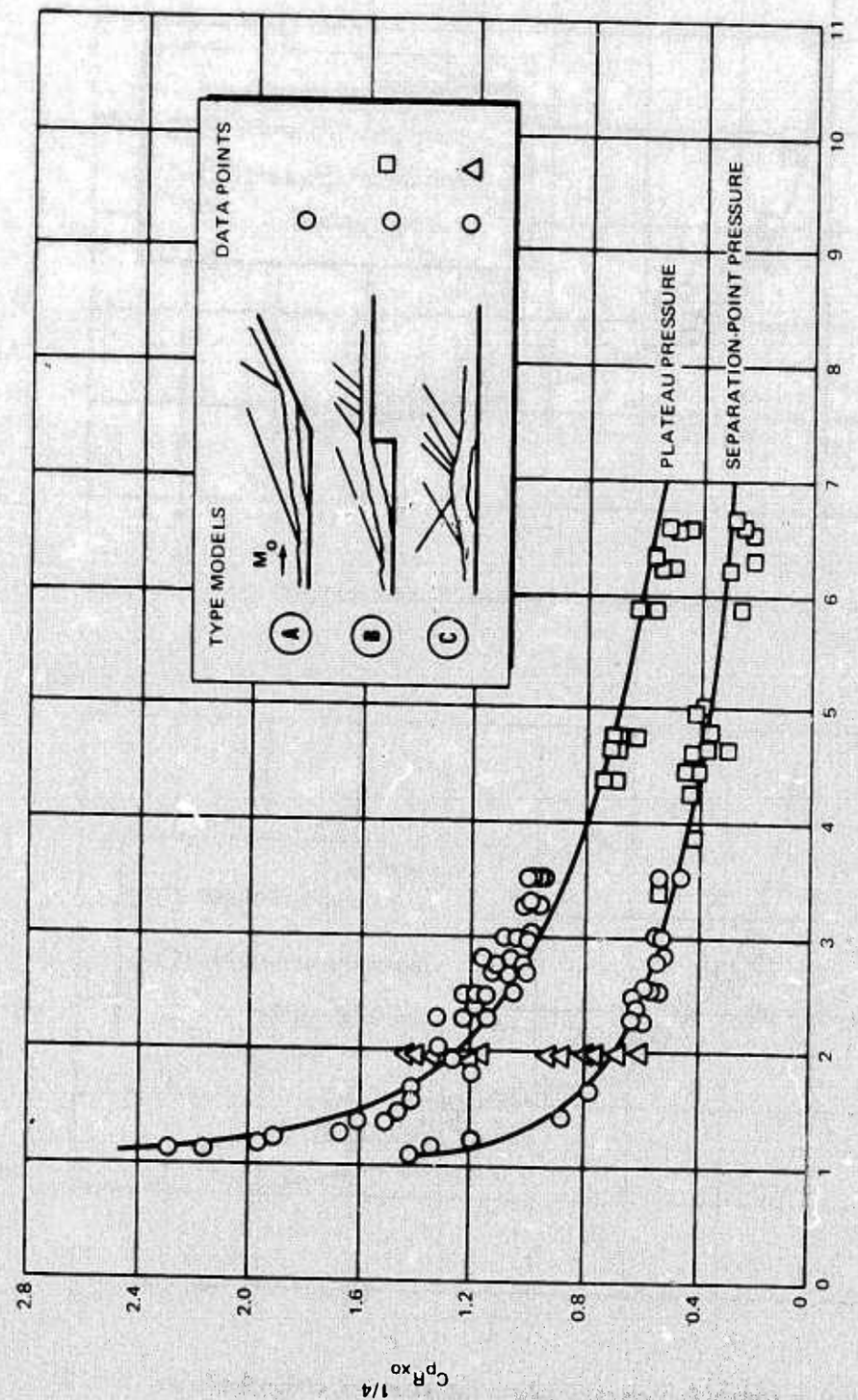

FIG. 3. Separation Point and Plateau Pressure for Insulated Laminar Flow (From Reference 6).

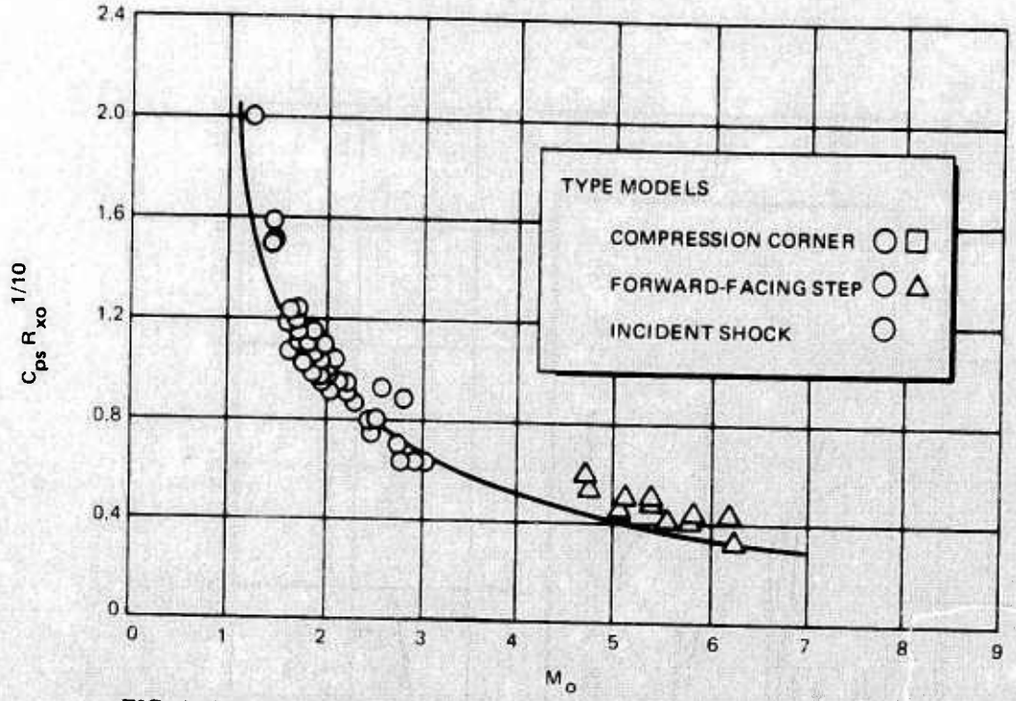

FIG. 4. Separation-Point Pressure for Insulated Turbulent Flow (From Reference 6).

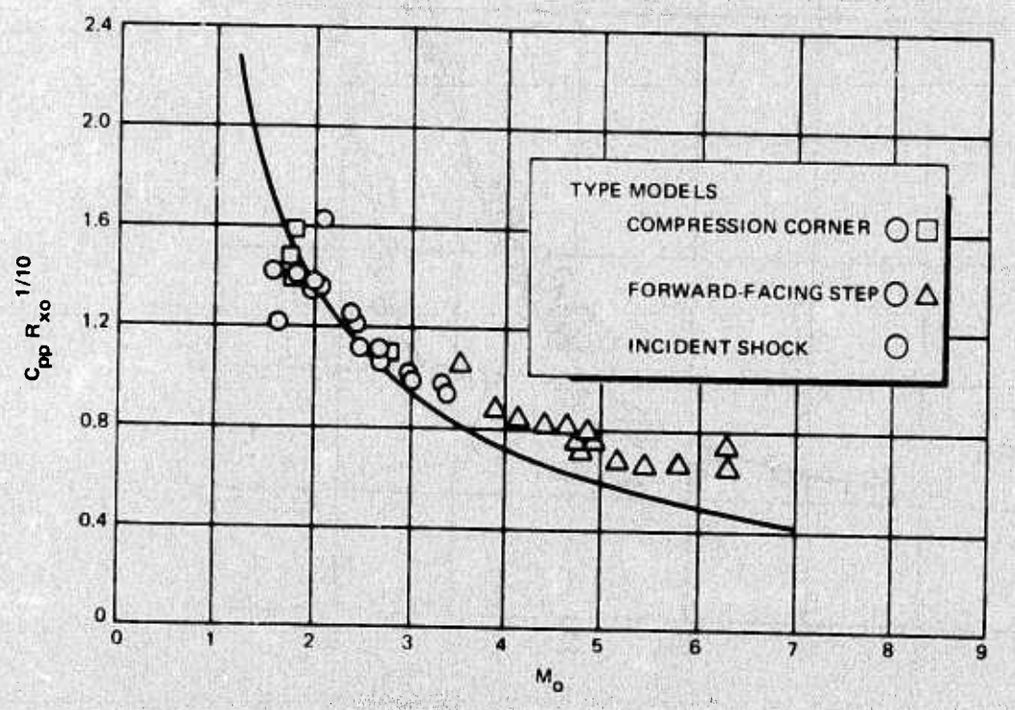

FIG. 5. Plateau Pressure for Insulated Turbulent Flow (From Reference 6).

For the purpose of expediting hand calculations, two more auxiliary charts for unit-length Reynolds number for various Mach numbers are given in Fig. 6 and 7.

Figures 6 through 12 are applicable for attached-side evaluation for all conditions. Different results may be obtained, depending on boundary-layer transition phenomena. To produce these curves, a transition Reynolds number of 10^6 has been used.

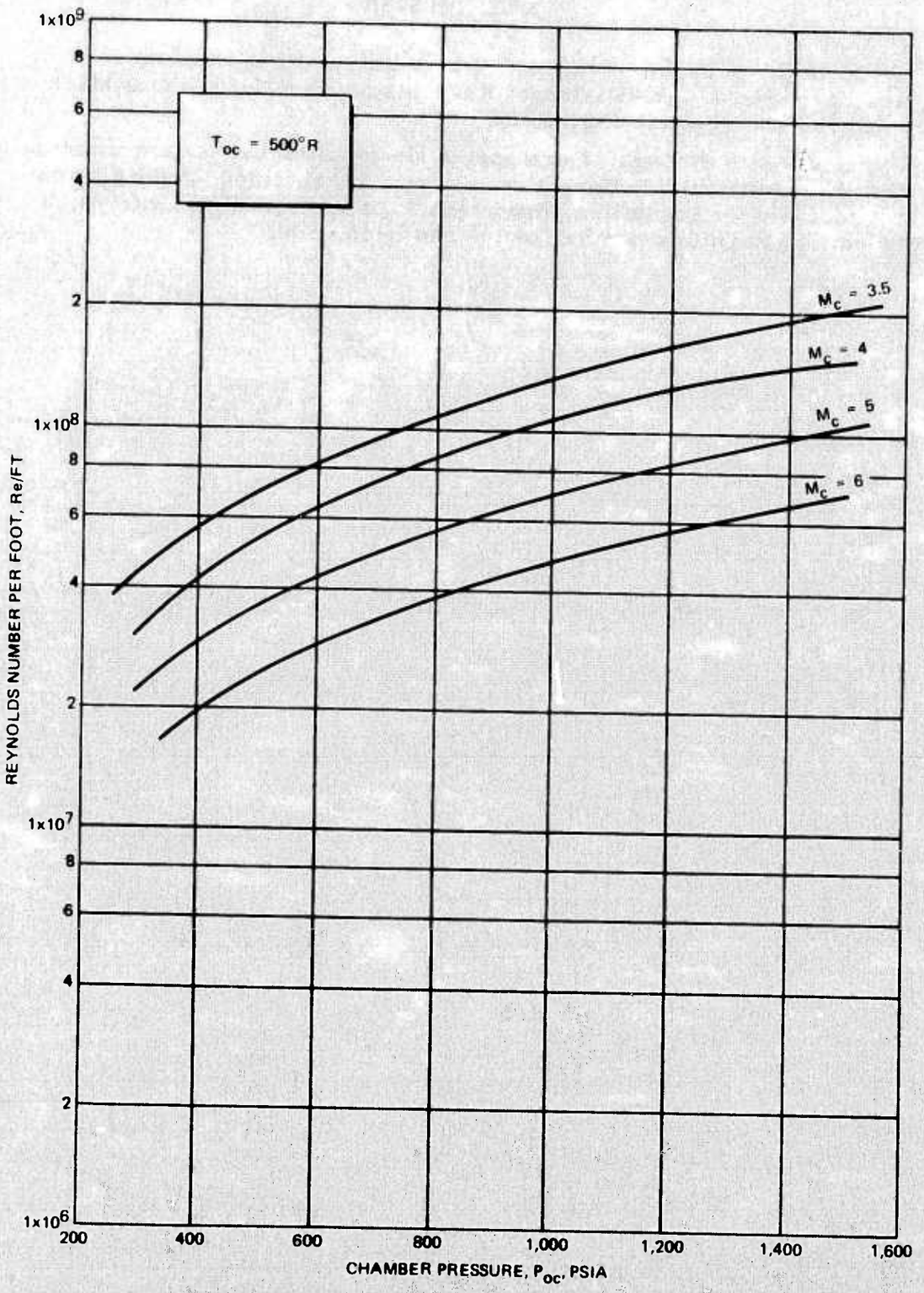

FIG. 6. Unit Reynolds Number Versus Chamber Pressure With Various Mach Numbers for γ_c = 1.4.

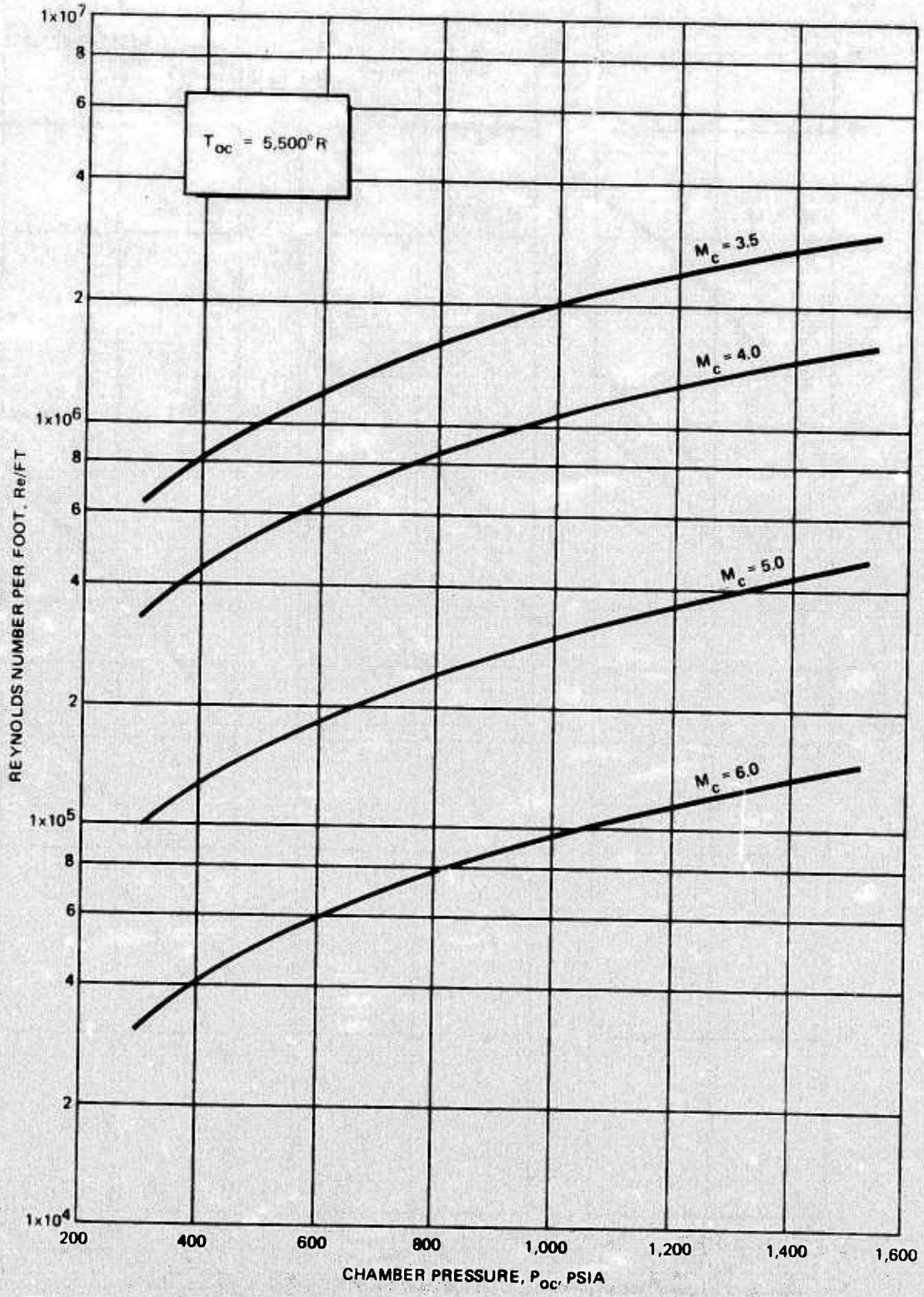

FIG. 7. Unit Reynolds Number Versus Chamber Pressure With Various Mach Numbers for γ = 1.2.

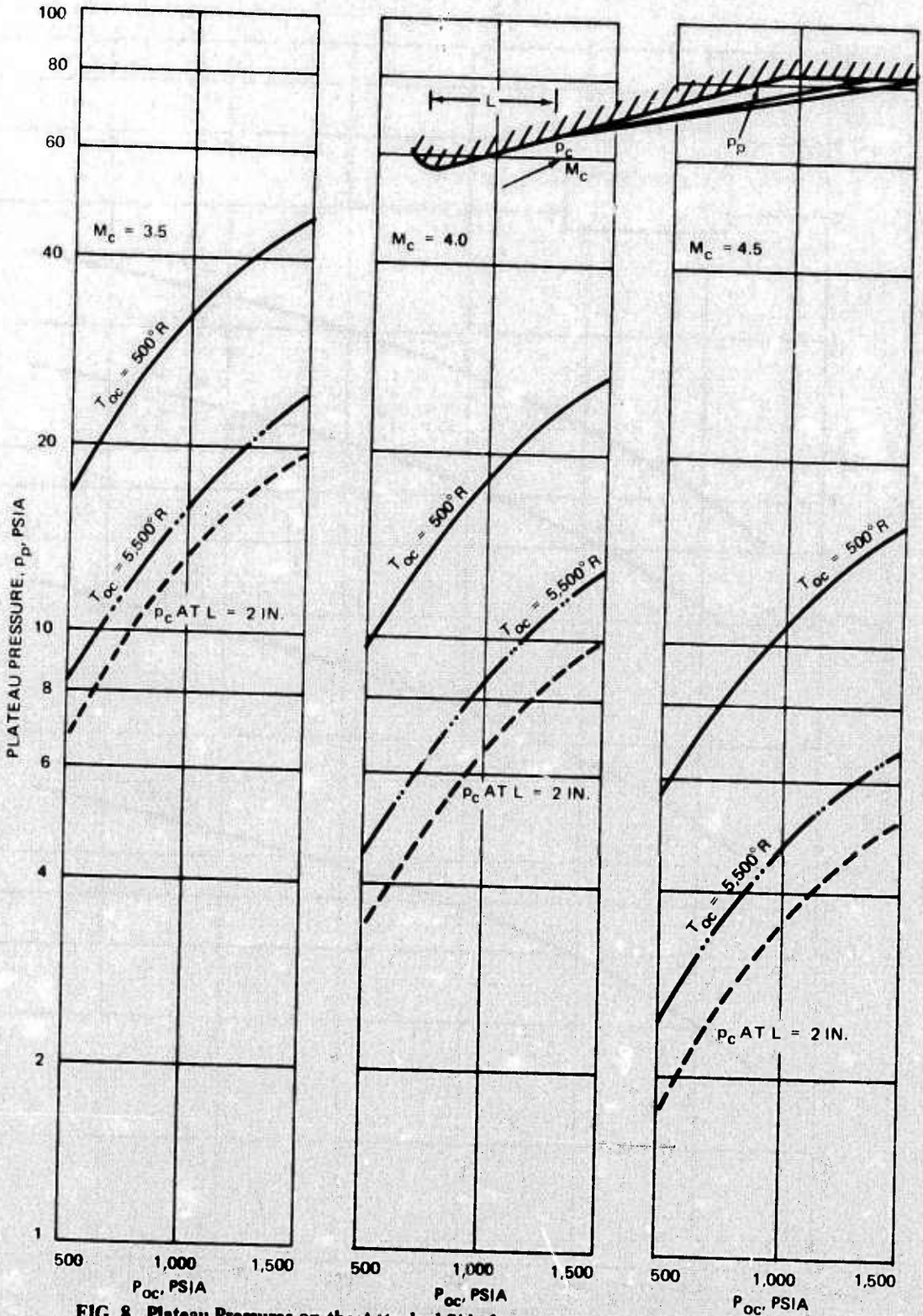

FIG. 8. Plateau Pressures on the Attached Side for $\gamma = 1.4$ and $M_c = 3.5$, 4.0, and 4.5.

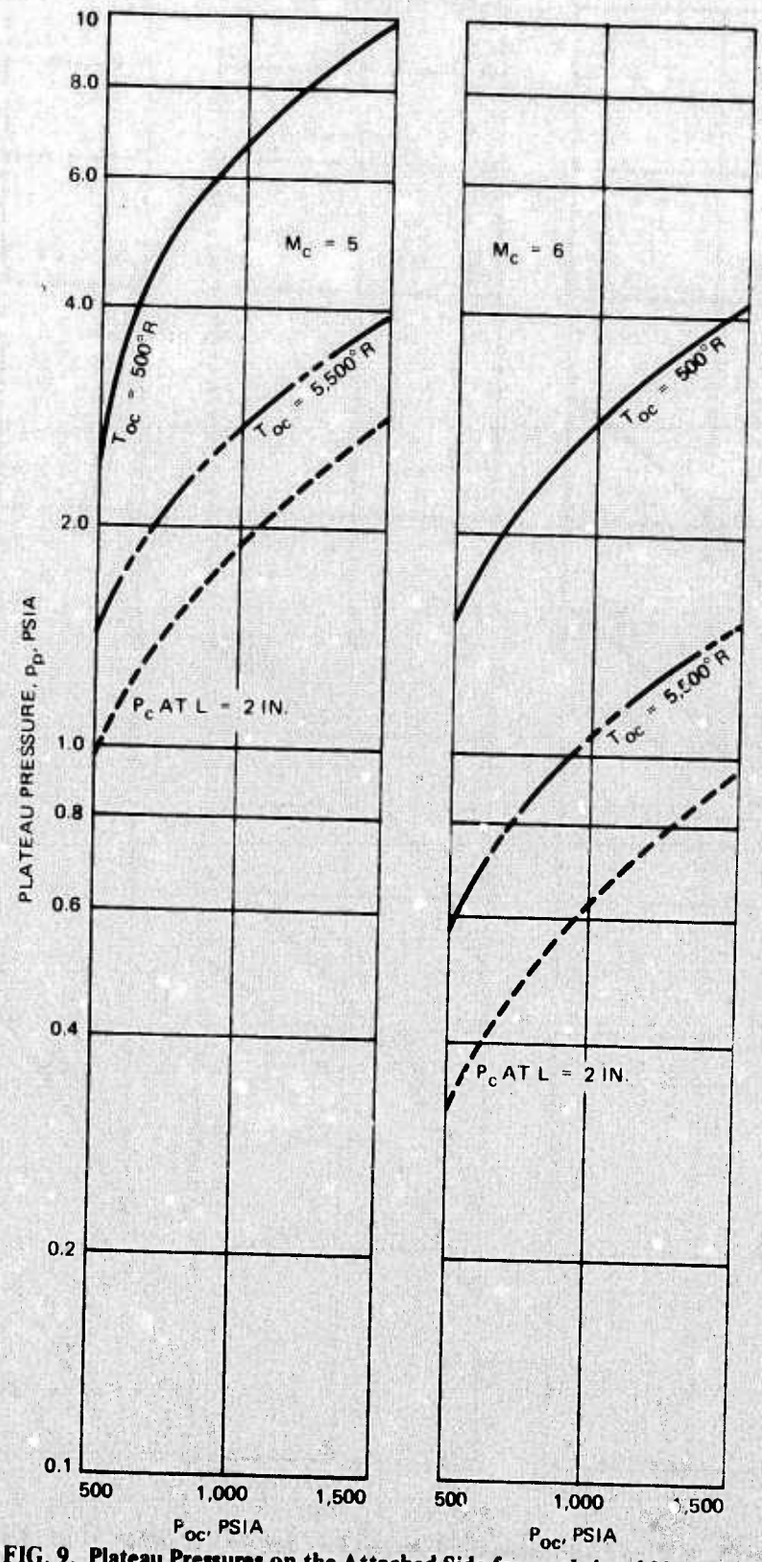

FIG. 9. Plateau Pressures on the Attached Side for γ = 1.4 and M_c = 5 and 6.

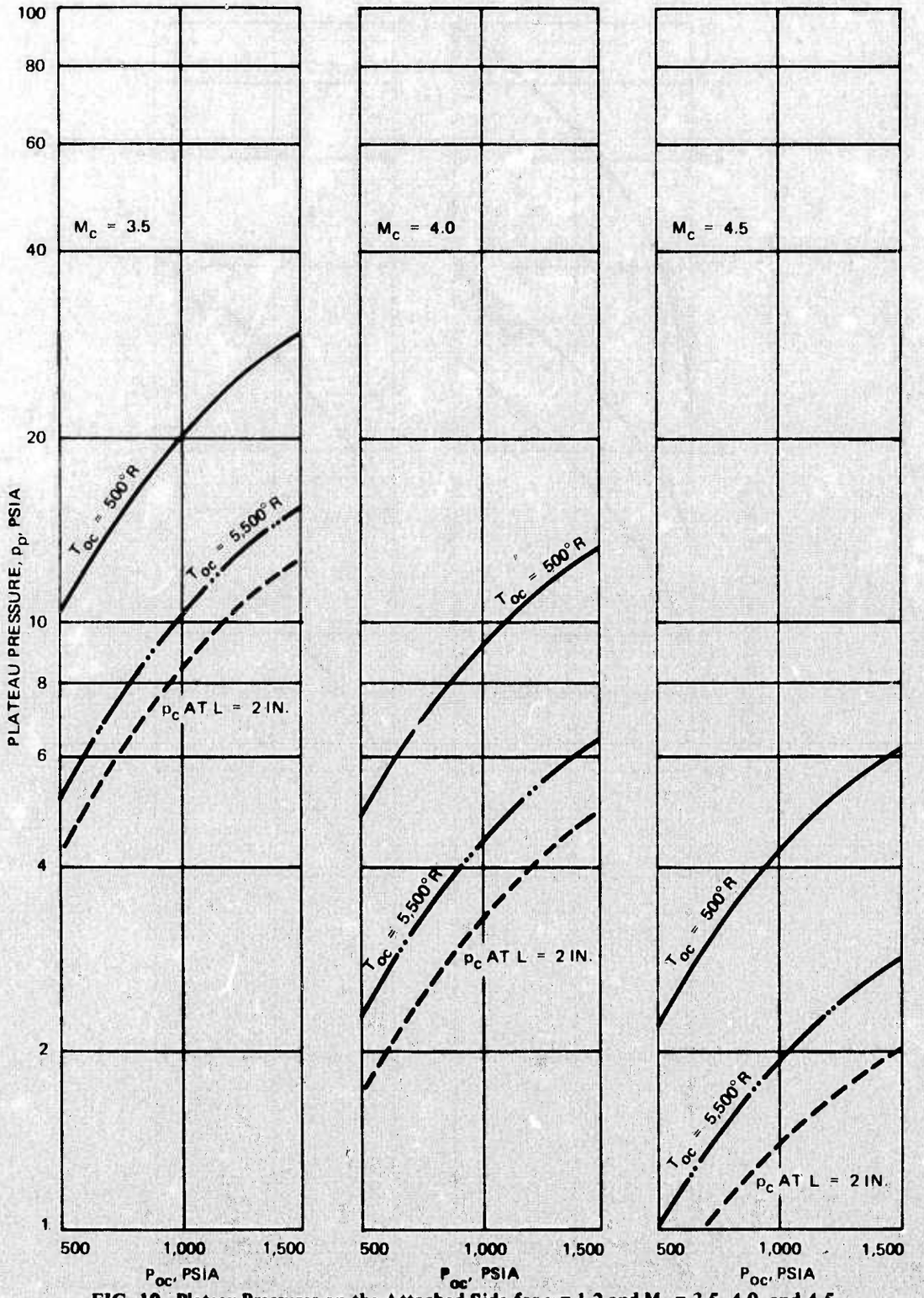

FIG. 10. Plateau Pressures on the Attached Side for $\gamma = 1.2$ and $M_c = 3.5$, 4.0, and 4.5.

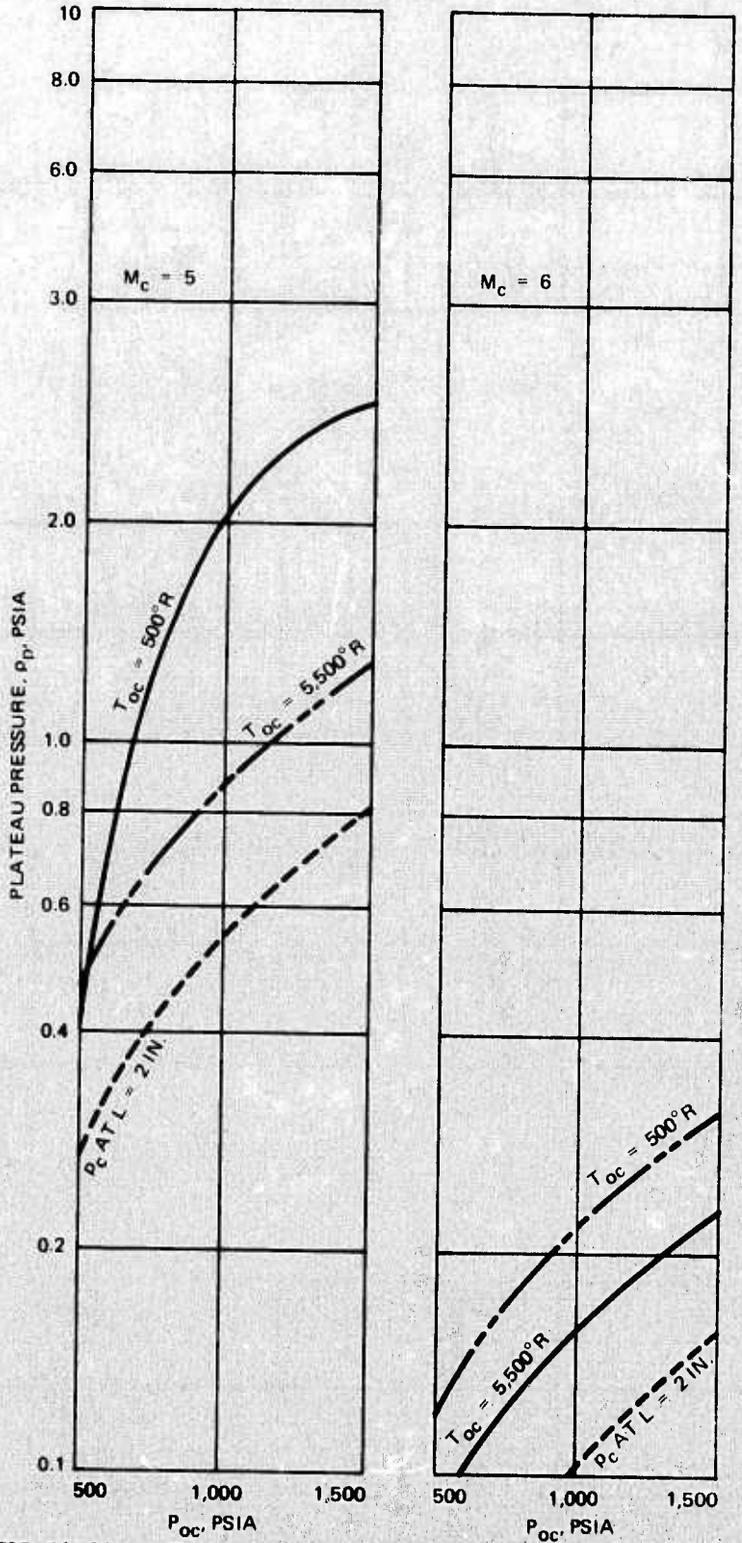

FIG. 11. Plateau Pressures on the Attached Side for γ = 1.2 and M_c = 5 and 6.

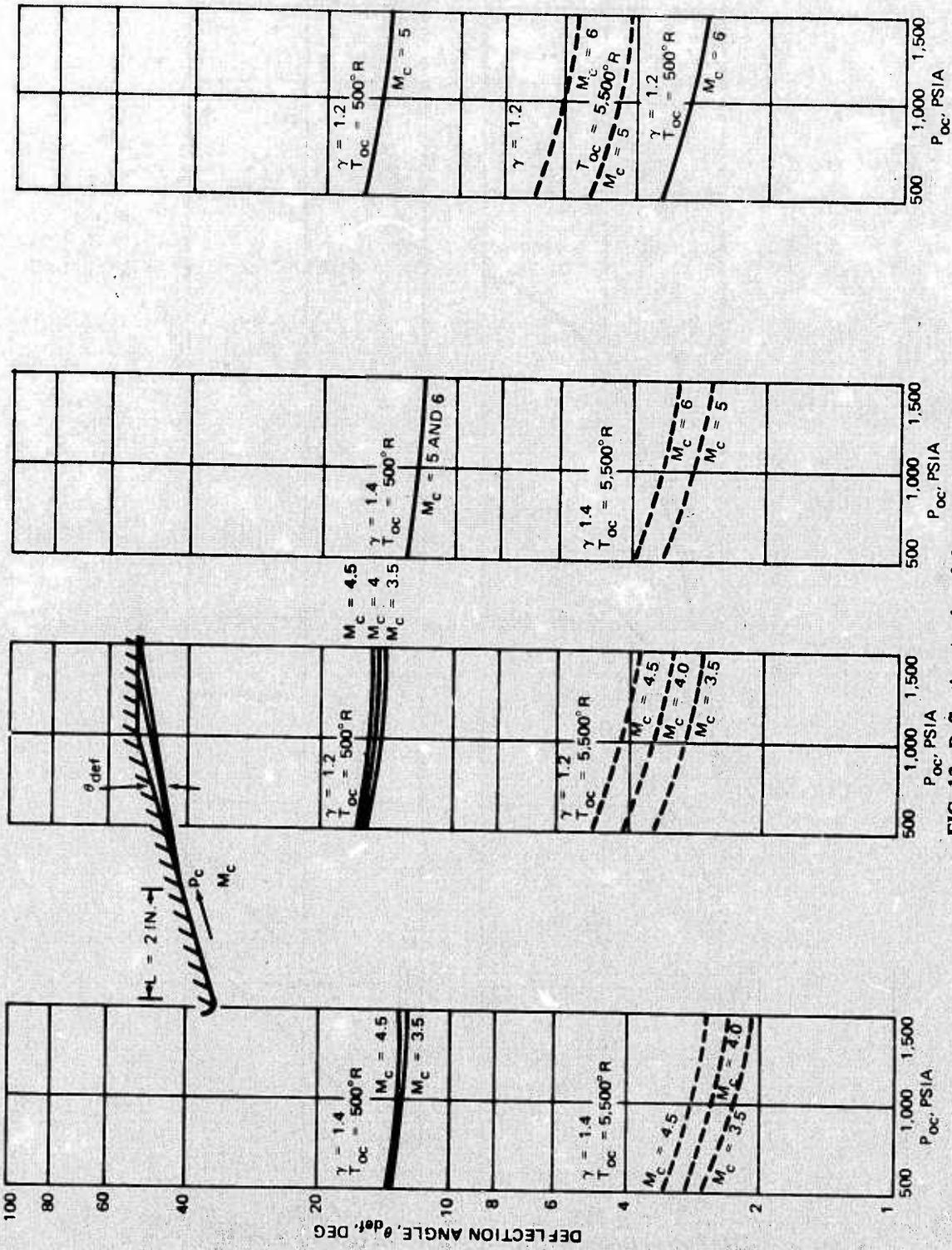

FIG. 12. Deflection Angles of the Attaching Flow.

FLOW-FIELD MODELS AND RESULTS

In this section, much of the analytical work that was done on flow-field modeling is described in detail. The results obtained from these analyses are presented here and in the Appendix, which treats two-stream jet-mixing interactions.

SEPARATION POINT

Flow-field separation is characteristically present in overexpanded nozzles. Methods to predict the separation point inside the nozzle include a correlation technique developed by Kalt and Badal (Ref. 7) and an analytical method developed by Thompson (Ref. 8). Thompson's analytical predictions do not agree well with the correlations of Kalt and Badal for 15-degree half-angle nozzles (see Fig. 13). This is probably due to some of the basic assumptions that were used in his theoretical development. For example, Thompson used a flat-plate flow model and assumed that the momentum of the fluid between the sonic line and the wall boundary is reduced to zero by the action of the pressure feedback.

Thompson's flow model, which was used in early BLTVC studies by Kampe (Ref. 9), is based on the law of momentum conservation applied to the control volume shown in Fig. 14. With this model, predictions of the separation-point location have been obtained by equating the momentum flux of the subsonic boundary to that associated with the immediate pressure gradient, i.e.,

$$\int_0^{\delta_s} \rho u^2 \, dy = (p_b - p_c)\delta_s \qquad (1)$$

where

- $u = u_c \, \phi(y/\delta)$, boundary-layer flow velocity at distance y from the wall
- δ_s = height of the subsonic portion of the boundary layer
- ρ = density
- p_c = local boundary-layer and mainstream pressure at the separation point
- p_b = pressure downstream of the separation point

It should be noted that p_b is the vortex (plateau) pressure for the attached-side separation and is equal to the base or ambient pressure for the port-side separation, i.e., $p_b \cong p_\infty$ for the present applications.

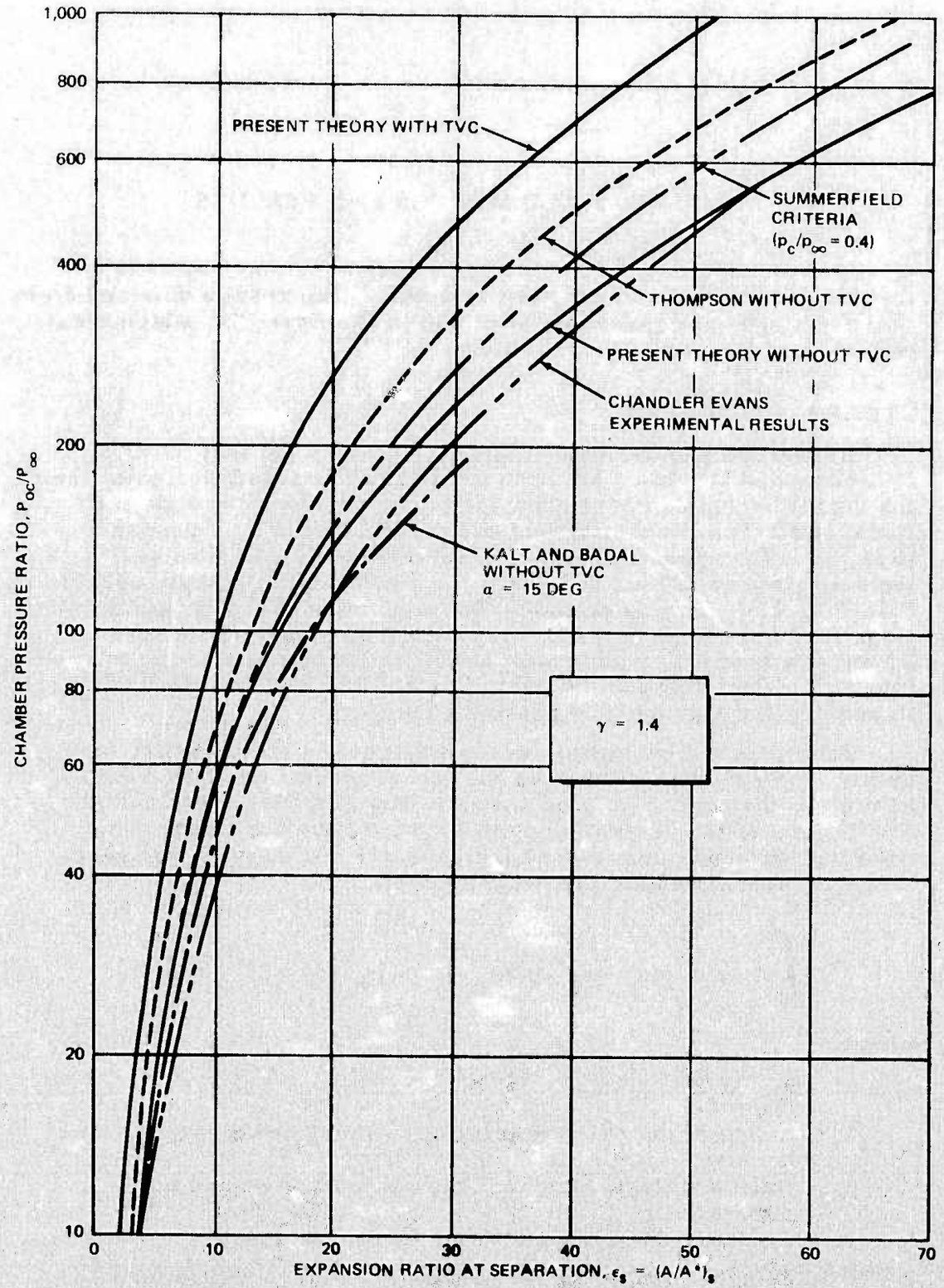

FIG. 13. Separation-Point Location Versus Chamber Pressure Ratio as Predicted by Various Methods.

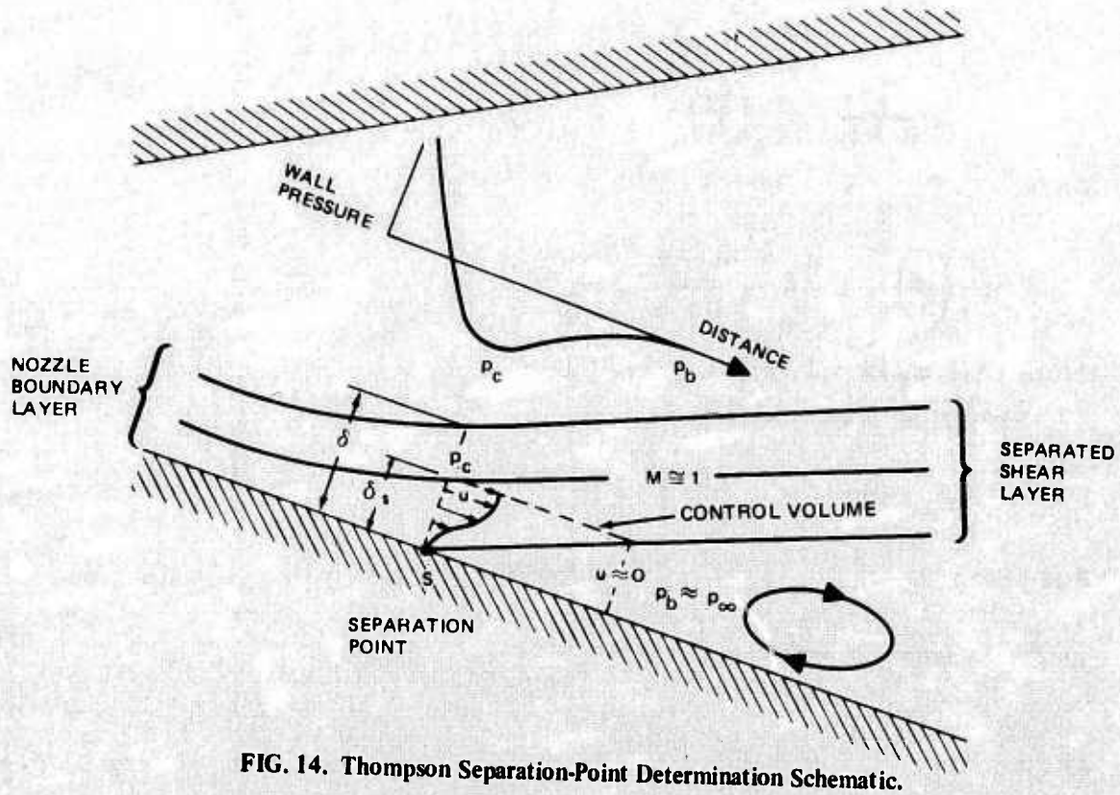

FIG. 14. Thompson Separation-Point Determination Schematic.

Equation 1 can be satisfied by using a trial-and-error method and iterating on the assumed point of separation. However, a closed-form solution can be obtained when a simple power-law velocity profile is used. The procedure, which is similar to those given in Ref. 7 and 8, is briefly as follows.

Assume

$$u = u_c \, (y/\delta)^{1/n} \tag{2}$$

$$\therefore \delta \int_0^{\delta_s/\delta} \rho_c u_c^2 \, (y/\delta)^{2/n} \, d(y/\delta) = (p_\infty - p_c)\delta_s$$

Integrating with ρ = constant results in

$$\frac{1}{\frac{2}{n} + 1} \, \delta \, \rho_c u_c^2 \left(\frac{y}{\delta}\right)^{\frac{2}{n} + 1} \Bigg|_0^{\frac{\delta_s}{\delta}} = (p_\infty - p_c) \, \delta_s \tag{3}$$

or

$$\rho_c \frac{n}{2+n} u_c^2 \left(\frac{\delta_s}{\delta}\right)^{\frac{2}{n}} = (p_\infty - p_c)$$

Since

$$\left(\frac{\delta_s}{\delta}\right)^{\frac{1}{n}} = \frac{u_s}{u_c} = \frac{u_s/a}{u_c/a} = \frac{1}{M_c}$$

(Note that $u_s/a = 1$ is being used.)

Equation 3 becomes

$$\rho_c \frac{n}{2+n} u_c^2 \left(\frac{1}{M_c}\right)^2 = (p_\infty - p_c) \tag{4}$$

But since $\rho_c u_c^2 = \gamma p_c M_c^2$, it is found that

$$\frac{n}{2+n} \gamma \frac{p_c}{p_{oc}} = \left(\frac{p_\infty}{p_{oc}} - \frac{p_c}{p_{oc}}\right) \tag{5}$$

or

$$\frac{2}{\gamma - 1} \left\{ \left[\left(\frac{n\gamma}{2+\gamma} + 1\right) \frac{p_{oc}}{p_\infty} \right]^{\frac{\gamma-1}{\gamma}} - 1 \right\} = M_c^2 \tag{6}$$

Results from Eq. 6 are shown in Fig. 13.

For axisymmetric flow with temperature variation, a more general velocity profile is used to replace the power-law profile. The velocity-profile family described in Ref. 10 by Kutateladze and Leont'ev is suitable for the analysis.

$$\frac{u}{u_c} = \frac{\psi - \left[(\psi)^{1/2} - \left\{ (\psi)^{1/2} - 1 \right\} \xi^n \right]^2}{\psi - 1} \tag{7}$$

where u = velocity, $\psi = T_w/T_e$, $\xi = y/\delta$, and n = pressure-gradient parameter. Subscripts w and e refer to wall and nozzle inviscid-flow conditions, respectively. Letting

$$\lambda \equiv \psi^{1/2} = (T_w/T_e)^{1/2}$$

Equation 7 becomes

$$\phi = \frac{u}{u_c} = \frac{\lambda^2 - \left[\lambda - \left\{\lambda - 1\right\}\xi^n\right]^2}{\lambda^2 - 1} \tag{8}$$

Equation 8 is a more general velocity profile that is used to replace the previous power-law profile in the following momentum equation.

$$\int_0^{\delta_s} \rho u^2 dy = (p_\infty - p_e)\,\delta_s \tag{9}$$

or

$$\rho_c u_c^2 \int_0^1 \frac{\rho}{\rho_c}\left(\frac{u}{u_c}\right)^2 d\left(\frac{y}{\delta_s}\right) = p_c\left(\frac{p_\infty}{p_c} - 1\right)$$

Equation 8 can be reduced to the Thompson-Kampe profile by letting $\lambda = 0$ and $n = 1/14$. This implies $T_w/T_c \to 0$ (cold-wall conditions).

Determination of ϕ

Crocco's relationship gives

$$T_o = T_w + \phi\,(T_{oc} - T_w)$$

but

$$T = T_o - \frac{1}{2}\frac{u^2}{c_p} = T_o - \frac{\gamma - 1}{2\gamma}\frac{u^2}{R}$$

$$= T_o - \frac{\gamma - 1}{2\gamma}\frac{u_c^2}{R\,T_c}\left(\frac{u}{u_c}\right)^2 T_c$$

$$= T_o - \frac{\gamma - 1}{2} M_c^2\, T_c \phi^2 \tag{10}$$

That is,

$$T = T_o - \frac{\gamma - 1}{2} M_c^2\, T_c \phi^2 \tag{11}$$

Also,

$$M^2 = \frac{u^2}{a^2} = \frac{\phi^2 u_c^2}{a_c^2 \frac{T}{T_c}} = M_c^2 \frac{\phi^2}{\frac{T_o}{T_c} - \frac{\gamma - 1}{2} M_c^2 \phi^2} \tag{12}$$

From Eq. 10 one has

$$\frac{T_o}{T_c} = \frac{T_w}{T_c} + \phi\left(\frac{T_{oc}}{T_c} - \frac{T_w}{T_c}\right) \tag{13}$$

Substituting Eq. 13 into Eq. 12 and evaluating ϕ as a function of M_c, λ, and M gives

$$\lambda^2 + \left(\frac{T_{oc}}{T_c} - \lambda^2\right)\phi - \left(\frac{\gamma - 1}{2} M_c^2 + \frac{M_c^2}{M^2}\right)\phi^2 = 0$$

or

$$\phi = \frac{-\left(\frac{T_{oc}}{T_c} - \lambda^2\right) \pm \sqrt{\left(\frac{T_{oc}}{T_c} - \lambda^2\right)^2 + 4\lambda^2\left(\frac{T_{oc}}{T_c} - \frac{M_c^2}{M^2} - 1\right)}}{-2\left(\frac{T_{oc}}{T_c} + \frac{M_c^2}{M^2} - 1\right)} \tag{14}$$

The proper root is determined by checking edge conditions with $\phi = 1$ at $M = M_c$. This gives

$$\phi = \frac{\left(\frac{T_{oc}}{T_c} - \lambda^2\right) + \sqrt{\left(\frac{T_{oc}}{T_c} - \lambda^2\right)^2 + 4\lambda^2\left(\frac{T_{oc}}{T_c} + \frac{M_c^2}{M^2} - 1\right)}}{2\left(\frac{T_{oc}}{T_c} + \frac{M_c^2}{M^2} - 1\right)} \tag{15}$$

Basic Computational Equations

Equation 9 becomes

$$\gamma M_c^2 \int_0^{\xi_s} \frac{\rho}{\rho_c} \phi^2 \, d\xi = \left(\frac{p_\omega}{p_c} - 1\right)\xi_s \tag{16}$$

but

$$\phi = \frac{\lambda^2 - \left[\lambda - (\lambda - 1)\xi^n\right]^2}{\lambda^2 - 1} \tag{17}$$

where

$$\lambda = (T_w/T_c)^{1/2} \tag{18}$$

Other equations are:

$$\frac{T_o}{T_c} = \lambda^2 + \phi\left(\frac{T_{oc}}{T_c} - \lambda^2\right) \tag{19}$$

$$\frac{T_{oc}}{T_c} = 1 + \frac{\gamma - 1}{2} M_c^2 \tag{20}$$

$$\frac{T}{T_c} = \frac{T_o}{T_c} - \left(\frac{T_{oc}}{T_c} - 1\right)\phi^2 \tag{21}$$

$$\rho/\rho_c = T_c/T = 1/(T/T_c) \tag{22}$$

$$\phi_s = \frac{\left(\frac{T_{oc}}{T_c} - \lambda^2\right) + \sqrt{\left(\frac{T_{oc}}{T_c} - \lambda^2\right)^2 + 2\lambda^2(\gamma+1)M_c^2}}{(\gamma+1)M_c^2} \tag{23}$$

$$\xi^n = \frac{\lambda - \sqrt{\lambda^2 - \phi_s(\lambda^2 - 1)}}{\lambda - 1} \tag{24}$$

The following inviscid-flow expressions are also used.

$$\frac{p_{oc}}{p_c} = \left(1 + \frac{\gamma - 1}{2} M_c^2\right)^{\frac{\gamma}{\gamma - 1}} \tag{25}$$

$$\frac{A^*}{A_c} = \left(\frac{\gamma + 1}{2}\right)^{\frac{\gamma + 1}{2(\gamma - 1)}} M_c \left(1 + \frac{\gamma - 1}{2} M_c^2\right)^{-\frac{2 + 1}{2(\gamma - 1)}} \tag{26}$$

Computational Results

The present method, based on the Kutateladze velocity profile, is used to simulate the correlation curve generated by Kalt and Badal. The results shown in Fig. 13 were obtained by using n = 1/14 for cases without TVC (which is equivalent to a 1/7 velocity profile for turbulent boundary layers) and n = 3/2 for cases with TVC. n = 3/2 corresponds to a cubic velocity profile (see Eq. 7). Experience in

separated-flow studies has shown that this is a reasonable approximation of the actual profile. Both curves were obtained by integrating the momentum flux within the shear layer from the wall up to the point where the local Mach number equals 1.35. Comparisons with several data correlations and theoretical predictions, including Thompson's results (which were obtained by terminating the integration at a local Mach number of unity), are also shown in Fig. 13.

Based on these two curves, local Mach number at the separation point can be computed for various chamber pressures. The results, shown in Fig. 15, are labeled Attached Side for conditions both with and without attachment and Port Side (With TVC) for cases with TVC. Similar results for cases with $\gamma = 1.2$ are shown in Fig. 16.

When the main flow from the nozzle separates, it may or may not reattach again on the side opposite to the port side. The reattachment phenomenon is influenced by the magnitude of the TVC gas injection. Since the cylindrical aft section has a deflection angle of 15 degrees with respect to the nozzle wall, the attaching flow undergoes a recompression process. The minimum pressure attainable at the separation point can be determined rather easily by a simple graphical method. The results, as shown in Fig. 17, were obtained as follows:

1. Local Mach number and the corresponding local pressure

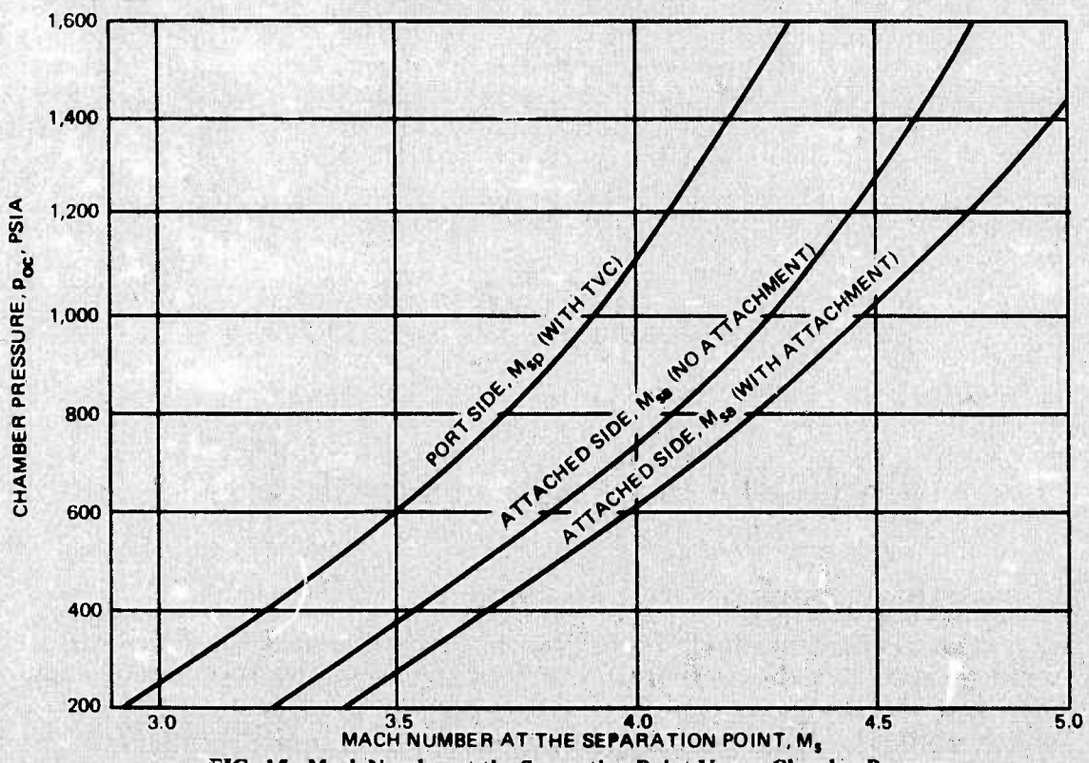

FIG. 15. Mach Number at the Separation Point Versus Chamber Pressure.

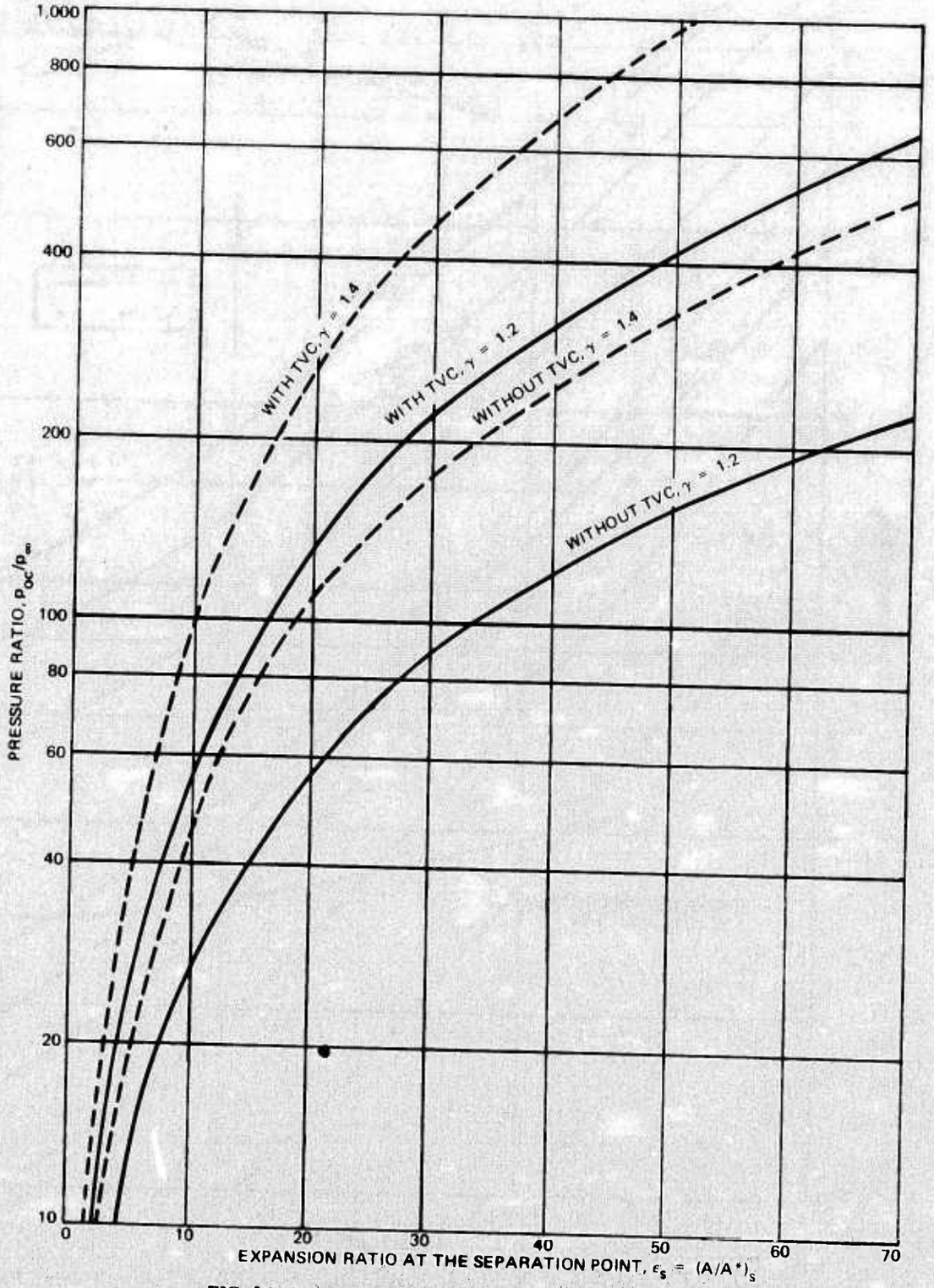

FIG. 16. Separation-Point Locations for Overexpanded Nozzles

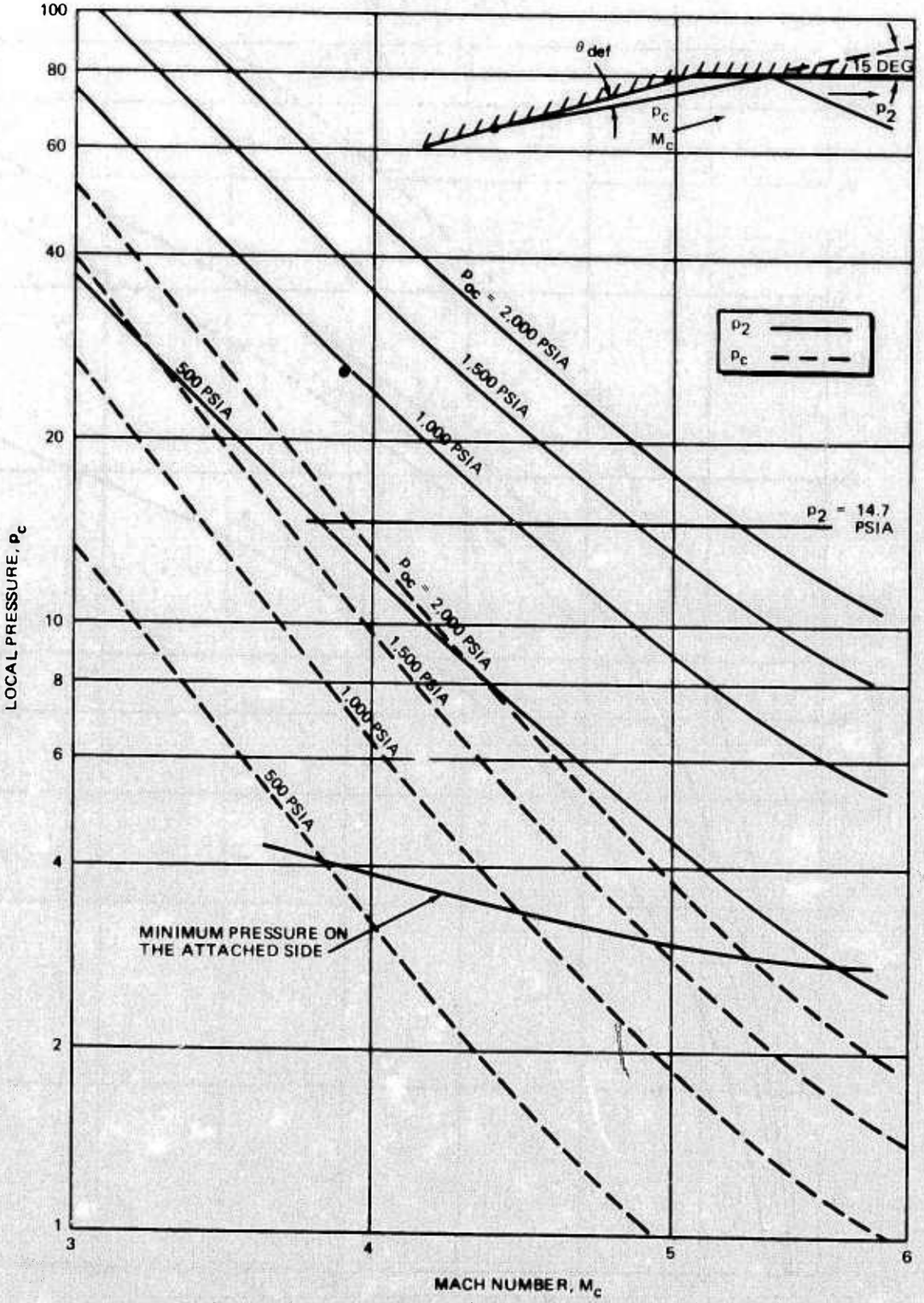

FIG. 17. Graphical Prediction for Minimum Pressures on the Attached Side with Nozzle Flow Fully Attached.

were calculated for various chamber pressures for a specified nozzle geometry. For the present calculations, a 15-degree turning angle is used, and results are shown as dashed lines in Fig. 17.

2. The downstream pressure can be obtained by the use of oblique-shock relations for M_c going through a 15-degree flow-deflection angle. The pressures downstream of the oblique shock, p_2, are shown as solid lines in Fig. 17.

3. When p_2 is equal to p_∞ (14.7 psia at sea level), the corresponding upstream pressure, p_c, represents the minimum pressure that the flow can attain without losing the attachment. This is shown in Fig. 17, and the corresponding Mach numbers are shown in Fig. 15.

Particle-Effect Considerations

Solid particles may exist in the nozzle flow. For example, carbon particles form in hydrocarbon-class fuels, and aluminum-oxide particles form in aluminized solid propellants. When the sizes, thermal-physical properties, and distributions of these particles are known, their effects on the flow-field interaction and characteristics can be estimated by considering them macroscopically. By using the same approach given in Ref. 8, Thompson's momentum equation is generalized to include the particle effects as follows:

$$\left(\int_o^{\delta_s} \rho u^2 dy\right)_g + \left(\int_o^{\delta_s} \rho u^2 dy\right)_p = \left[(p_b - p_c)\ \delta_s\right]_g + \left[(p_b - p_c)\ \delta_s\right]_p \tag{27}$$

where the subscript g denotes gas and the subscript p denotes particle.

Thermal-physical properties of particles are known to be extremely important in evaluating the energy transfer in the nozzle flow to account for phenomena such as chemical reactions along the flow path. However, they are usually much less important in evaluating the momentum transfer, which is the primary governing function in determining the separation point. Nonetheless, their effect on separation can be qualitatively examined by noting that

$$\left(\int_o^{\delta_s} \rho u^2 dy\right)_g + \left(\int_o^{\delta_s} \rho u^2 dy\right)_p \equiv A \left(\int_o^{\delta_s} \rho u^2 dy\right)_g \tag{28}$$

$$\left[(p_b - p_c)\ \delta_s\right]_g + \left[(p_b - p_c)\ \delta_s\right]_p \equiv B \left[(p_b - p_c)\ \delta_s\right]_g \tag{29}$$

That is, the effect of particles on momentum balance is represented mathematically by two parameters, A and B. These parameters can

either be greater or smaller than unity, depending on the size, distribution, and thermal-physical properties of the particles.

Substituting Eq. 28 and 29 into Eq. 27, one obtains

$$A\left(\int_0^{\delta_s} \rho u^2 dy\right)_g = B\left[(p_b - p_c)\ \delta_s\right]_g$$

Carrying through the procedure given previously, a closed-form solution similar to Eq. 6 can be obtained.

$$\frac{2}{\gamma - 1}\left\{\left[\left(\frac{A}{B}\ \frac{n\gamma}{2+n} + 1\right)\ \frac{p_{oc}}{p_\infty}\right]^{\frac{\gamma-1}{\gamma}} - 1\right\} = M_c^2 \qquad (30)$$

Typical values of A/B ratio are used to examine the overall effect of particles on the separation-point location, which in turn will affect TVC performance. Results, shown in Fig. 18, indicate that the particle effect will delay the boundary-layer separation (cases with $A/B > 1$), but not drastically.

BLTVC INJECTION FLOW RATE

The mass-addition effect of the TVC gas on the nozzle main flow will be discussed in detail in the next section. However, it is useful to know the variation of the mass-injection rate at the beginning and during the period of TVC operation.

By employing a one-dimensional nozzle-flow analysis, the mass-flow rate can be given as (Ref. 11)

$$\frac{\dot{m}\sqrt{R\ T_o}}{A\ p_o} = \sqrt{\frac{2}{\gamma - 1}\left(\frac{p}{p_o}\right)^{\frac{2}{\gamma}} - \left(\frac{p}{p_o}\right)^{\frac{\gamma+1}{\gamma}}} \qquad (31)$$

When the above equation is applied to the CEN-17 nozzle, one obtains

$p = p_p$ (port-side pressure, psia)

$p_o = p_\infty$ (ambient pressure, psia)

$\gamma = 1.4$ for air

$R = \frac{53.3}{g} = 1.655$ for air

$A = A_{port} = 0.921$ in.^{2} for three 5/8-inch-diameter holes

$T_o = T_\infty \cong 500°R$

$\dot{m}$ = (lbm/sec)

Eq. 31 is used to construct the injection-rate-versus-pressure curve given in Fig. 19. From the equations given earlier in this section, it can be determined that $p_c/p_\infty \cong 0.32$ for an overexpanded nozzle.

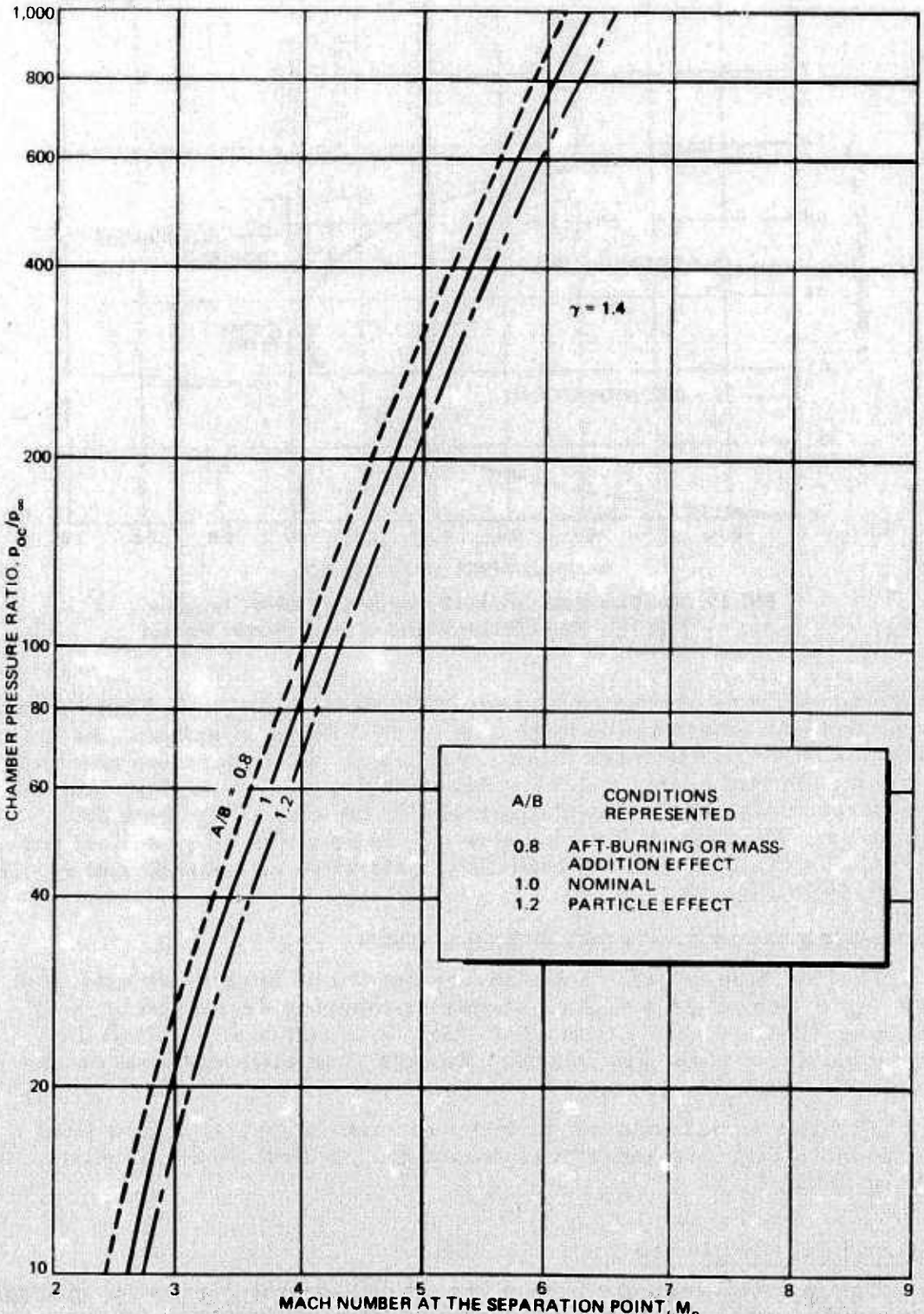

FIG. 18. Particle Effect on the Separation-Point Location Using Thompson's Method.

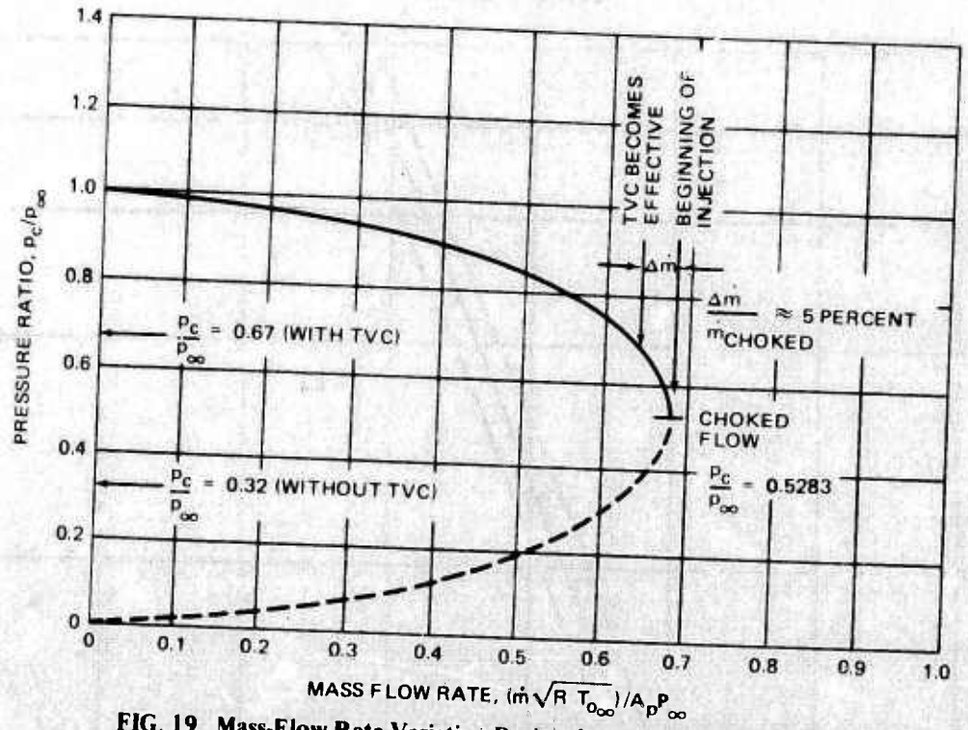

FIG. 19. Mass-Flow-Rate Variation During the Time of TVC Injection With TVC Being Effective for Overexpanded Nozzles Without Ambient Flow.

Since choked flow occurs at a pressure ratio of $p_c/p_\infty = 0.5283$, a choked-flow condition exists at the beginning of TVC mass injection. As discussed earlier, TVC mass injection will shift the separation point upstream such that $p_c/p_\infty \cong 0.67$. Accordingly, the mass flow rate will drop approximately 5%, as compared with the choked-flow value. Therefore, the choked-flow $\dot{m}$ value can be used for all practical purposes. Values of $\dot{m}$ for the cold-flow tests were computed, and results are given in Fig. 20.

TWO-STREAM JET-MIXING INTERACTION

The two-stream jet-mixing theory described here is an extension and application of the original jet-mixing theories developed by Chapman (Ref. 12) and Korst (Ref. 13). It is commonly called the Chapman-Korst base-flow model. Basic and related information can be found in Ref. 12, 13, and 14.

The flow model consists of two elements: an inviscid flow field as shown in Fig. 21a and a two-stream mixing-flow model as shown in Fig. 21b.

Inviscid Jet Boundaries

The inviscid-edge conditions are needed for describing the mixing-layer properties. To compute these conditions, a value of p_2 is

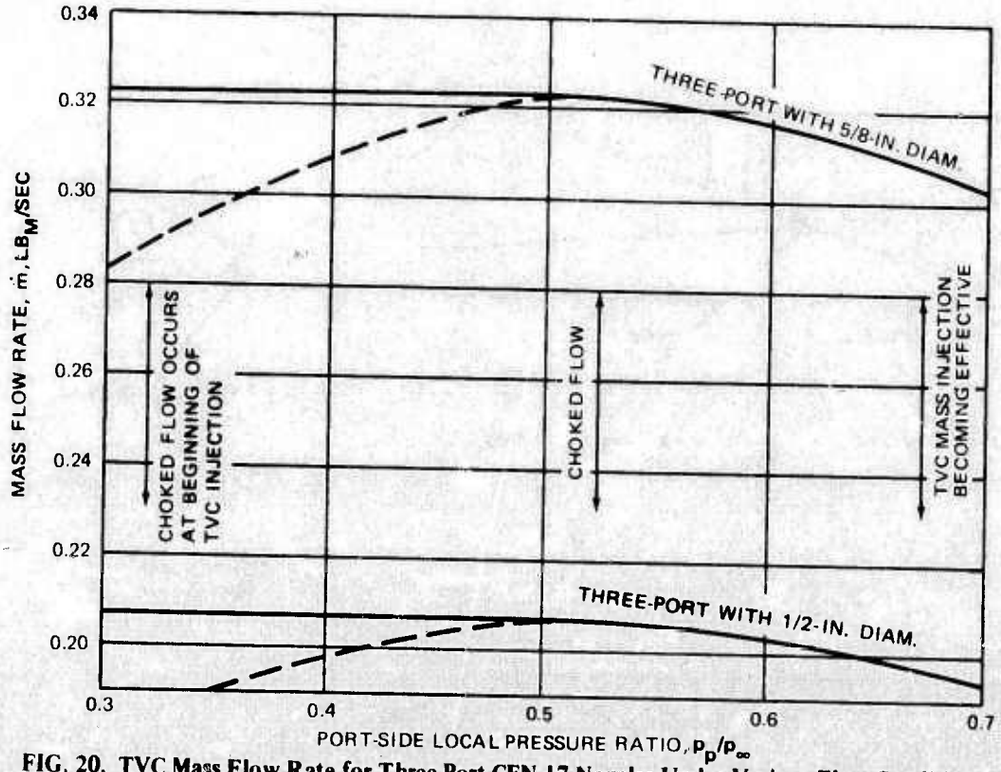

FIG. 20. TVC Mass Flow Rate for Three-Port CEN-17 Nozzles Under Various Flow Conditions.

initially assumed, and p_2 is subsequently used as an iterative variable so that a mixing layer can be imposed on a corresponding inviscid streamline to obtain viscous solutions. Since matching between the inviscid and viscous solutions is required frequently in the computing process, inviscid relations such as the isentropic Prandtl-Meyer theory are used rather than more time-consuming approaches such as the method of characteristics. In the same spirit, the nozzle flow is also described by the isentropic flow relations.

The mass flow ratio used frequently in the computation is

$$\frac{(\rho u)_2}{(\rho u)_1} = \frac{M_2}{M_1}\left\{\frac{1+\frac{\gamma-1}{2}M_1^2}{1+\frac{\gamma-1}{2}M_2^2}\right\}^{\frac{\gamma+1}{2(\gamma-1)}} \tag{32}$$

and the flow turning angle, θ_2, is related to θ_1 by the Prandtl-Meyer expansion relation as

$$\theta_2 = \theta_1 + (\nu_2 - \nu_1) \tag{33}$$

where θ_2 is an approximate streamline direction for the overall expanded outer-inviscid flow. Similar relations can be obtained for the inner (nozzle) flow using proper shock-wave relations.

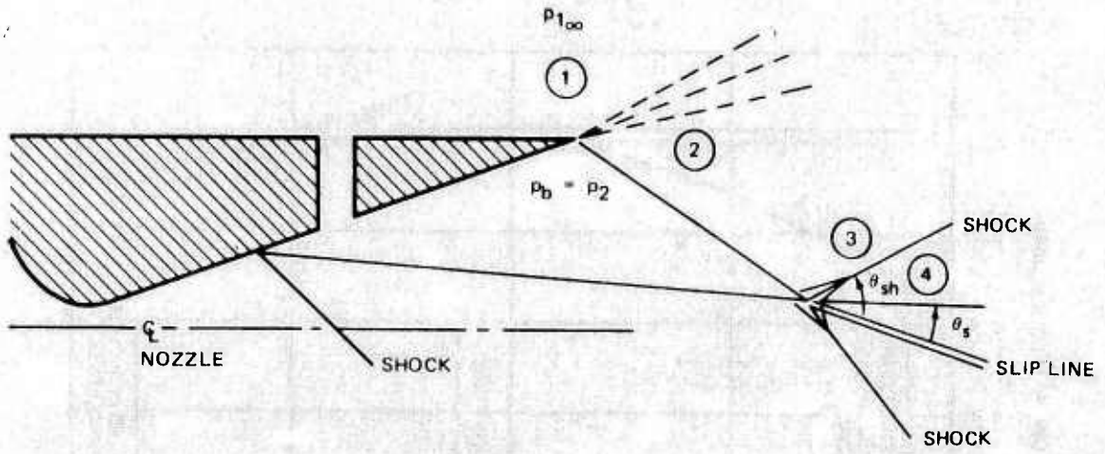

a. Inviscid flow field

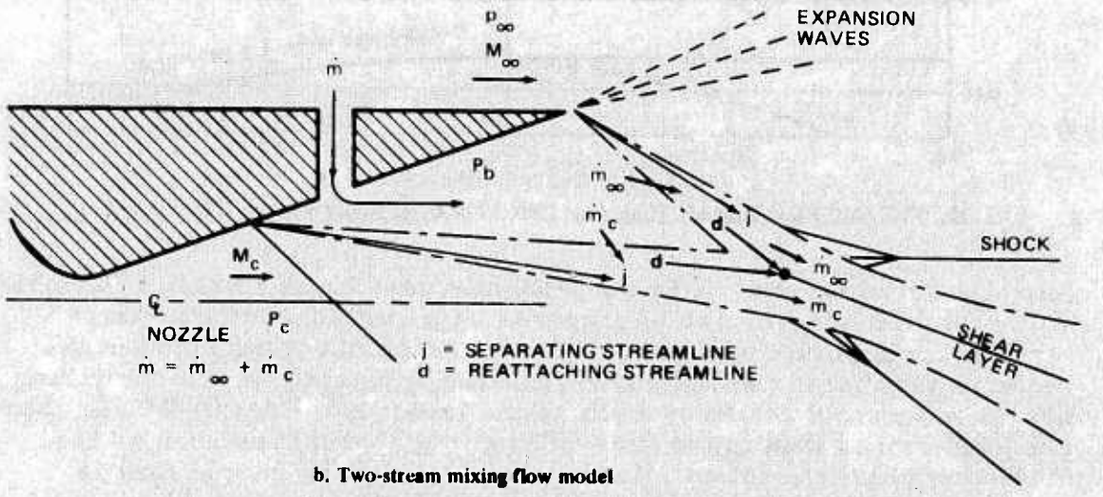

b. Two-stream mixing flow model

FIG. 21. Two-Stream Flow-Field Interactions – Inviscid and Intrinsic.

Downstream Recompression

Wedge theory is used in order to specify the recompressed inviscid-flow properties. The pressure rise is determined by the position of the slipline, the oncoming Mach number, and the shock-wave angle of each stream. For example, for a selected value of the slipline angle, θ_s, the recompression pressure, p_4, is computed using oblique shock relations, viz.

$$\frac{p_4}{p_3} = \frac{2\,\gamma\,M_{3e}^2\,\sin^2\,\theta_{sh} - (\gamma-1)}{\gamma+1} \qquad (34)$$

Iterations are made on the value of the slipline angle until the pressures and the flow directions for the two flows above and below the slipline are equal. As discussed later, this recompression pressure, p_4, is an important quantity in dealing with the reattachment process.

Initial Boundary-Layer Effects

Some properties of the mixing layer are influenced (1) by the external boundary-layer characteristics that exist at the missile aft end and (2) by the internal boundary-layer characteristics that exist at the nozzle flow-separation point. Methods to estimate these effects, such as those given in Ref. 15 and 16, are available. However, because of the predominant effects of the TVC injection mass, the initial boundary effects are secondary and have not been considered in the present analysis.

Mixing-Layer Properties

To describe the mixing-layer velocity profile, an error function has been used. This profile has been analytically derived and experimentally verified for the two-dimensional and axisymmetric mixing layers (Ref. 17 and 18), respectively. The profile is expressed by

$$\phi = \frac{u}{u_e} = \frac{1}{2} (1 + \text{erf}\, \eta) \tag{35}$$

where $\eta = \sigma y/x$ and σ is the jet-spreading parameter which, from Ref. 14 and 17, is given by

$$\sigma = 12 (1 + 0.23\, M_{ze}) \tag{36}$$

and where the error function, erf η, is defined as

$$\text{erf}\, \eta \equiv \frac{2}{\sqrt{\pi}} \int_0^{\eta} e^{-\beta^2}\, d\beta \tag{37}$$

Although the present velocity profile may not exactly follow the error-function shape, it is widely known that an integral method, such as the one used here, is not very sensitive to small changes in profile shape.

The total enthalpy profile is obtained using the Crocco relation:

$$\Lambda = \phi + \Lambda_B (1 - \phi) = \Lambda_b + (1 - \Lambda_b)\, \phi \tag{38}$$

where $\Lambda \equiv h_o/h_{oe}$ is the total enthalpy ratio of the jet.

The density profile for a constant-pressure mixing region is given as

$$\frac{\rho}{\rho_e} = \frac{\mathcal{M} T_e}{\mathcal{M}_e T} = \frac{h_{oe} - u_e^2/2}{h_o - u^2/2} \frac{c_p \mathcal{M}}{c_{pe} \mathcal{M}_e} = \frac{1 - C_e^2}{\Lambda - \phi^2 C_e^2} \lambda \qquad (39)$$

where $\lambda \equiv c_p \mathcal{M} / c_{pe} \mathcal{M}_e$ is the molar specific-heat ratio of the jet.

The thermodynamic properties such as specific heat, c_p, and specific-heat ratio, γ, are assumed to be independent of temperature for the purpose of simplicity and computational efficiency.

Important Streamlines

There are two important streamlines in a mixing-layer analysis. One is called the separating (or dividing) streamline, the other the reattaching (or discriminating) streamline. The latter is either identical to or related to the former, depending on whether there is an injection or not. Therefore, it is necessary to locate the separating streamline first. To do this, the coordinate shift, η_m, should be determined. Since the initial boundary-layer effects have been neglected, the "restricted" mixing theory of Korst for a negligible initial boundary layer is directly applicable (Ref. 14). The X-momentum entrained by the recirculating flow is usually ignored. Hence, X-momentum conservation gives the following relation per unit width of the mixing layer:

$$(\rho u^2 Y)_e = \int_{-\infty}^{y_e} \rho u^2 dy \qquad (40)$$

The y_e is large enough that $\phi_e \to 1$.

The coordinate system shown in Fig. 22 indicates the following relation:

$$X \cong x \qquad (41)$$

$$Y \cong y - y_m(x) \qquad (42)$$

where X-Y and x-y are the inviscid and intrinsic coordinate systems, respectively. Using the similarity coordinates, $y = (x/\sigma)\eta$, Eq. 42 becomes

$$Y = \frac{x}{\sigma} (\eta - \eta_m)$$

Equation 40 then becomes

$$(\eta_e - \eta_m)(\rho u^2)_e = \int_{-\infty}^{\eta_e} \rho u^2 d\eta \qquad (43)$$

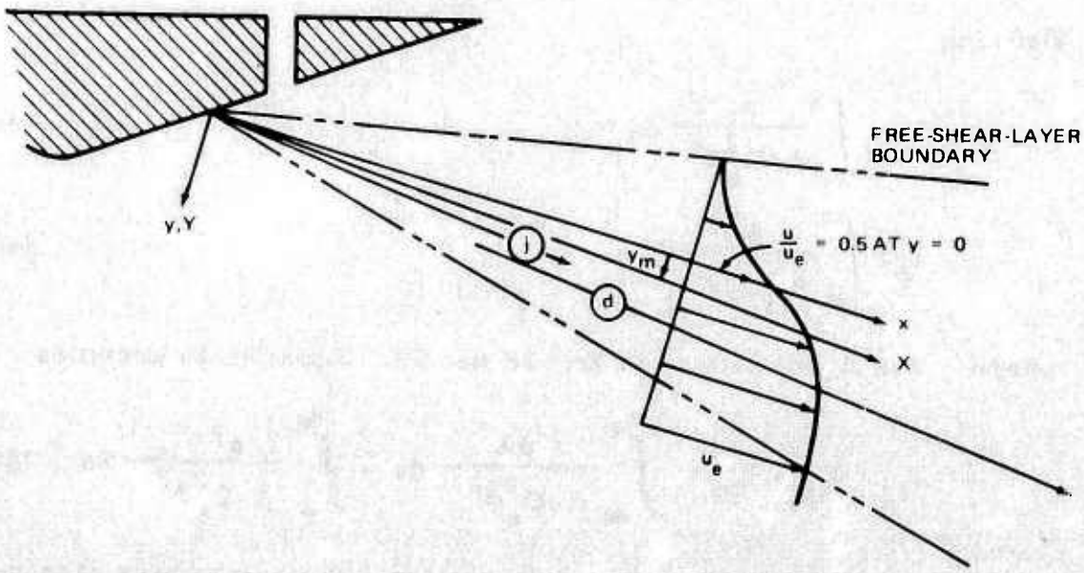

FIG. 22. Coordinate Systems and Nomenclature.

and with Eq. 39, it results in

$$\eta_e - \eta_m = \int_{-\infty}^{\eta_e} \frac{\rho u^2}{(\rho u^2)_e} d\eta = (1 - C_{2e}^2) \int_{-\infty}^{\eta_e} \frac{\phi^2 \lambda}{\Lambda - C_e^2 \phi^2} d\eta \qquad (44)$$

Separating (Dividing) Streamline. With the use of the preceding analyses, the separating streamline, j, can be determined. This streamline separates the main nozzle flow at the separating corner from the entrained into the recirculated flow region. One may use the mass conservation law:

$$(\rho u Y)_e = \int_{y_j}^{y_e} \rho u \, dy \qquad (45)$$

Using the similarity coordinates and Eq. 39 and 43, an equation results that allows the separating streamline to be determined.

$$\int_{\eta_j}^{\eta_e} \frac{\phi \lambda}{\Lambda - C_e^2 \phi^2} d\eta = \int_{-\infty}^{\eta_e} \frac{\phi^2 \lambda}{\Lambda - C_e^2 \phi^2} d\eta \qquad (46)$$

Defining

$$I_1 \equiv \int_{-\infty}^{\eta} \frac{\phi}{\Lambda - C_e^2 \phi^2} \, d\eta \tag{47}$$

$$I_2 \equiv \int_{-\infty}^{\eta} \frac{\phi^2 \lambda}{\Lambda - C_e^2 \phi^2} \, d\eta \tag{48}$$

where λ and Λ are defined in Eq. 38 and 39. Equation 46 becomes

$$I_{1j} = I_{1e} - I_{2e} = \int_{-\infty}^{\eta_e} \frac{\phi \lambda}{\Lambda - C_e^2 \phi^2} \, d\eta - \int_{-\infty}^{\eta_e} \frac{\phi^2 \lambda}{\Lambda - C_e^2 \phi^2} \, d\eta \tag{49}$$

Reattaching (Discriminating) Streamline. The reattaching streamline, d, is the other important streamline considered. This is the streamline that divides the mass flow in the mixing layer from the flow, which is turned back into the base region to be recirculated and/or vented. When there is no injection, the d and j streamlines are identical. With injection present, the j and d streamlines are related by the amount of mass pumping in or out of the recirculation region according to the following relation:

$$\dot{m} = \pm \int_{y_j}^{y_d} \rho u \, dy \tag{50}$$

where the negative sign refers to $y_d < y_j$, i.e., mass is being pumped out of the recirculation region through the mixing layer as shown in Fig. 21b.

Reattachment (Recompression) Process

Perfect mass-pumping effectiveness is assumed, and the cutoff location of the free-shear-layer region is consequently ended at the rear stagnation point. Furthermore, a Nash factor of unity is used, which implies

$$\frac{p_{o3d}}{p_{3e}} = \frac{p_4}{p_3} \tag{51}$$

where p_4 is the pressure that exists on a wedge of angle θ_{12} behind the oblique shock when a flow with Mach number M_{3e} exists. Note that when $M_{3d} \geq 1$, $p_4 = p_{o3dy}$, i.e., the value of p_{o3d} is therefore

the stagnation pressure behind a normal shock. Obtaining the stagnation pressure of the d streamline permits evaluation of the remaining properties:

$$\frac{T_{od}}{T_d} = \left(\frac{p_{od}}{p_d}\right)^{\frac{\gamma - 1}{\gamma}} = \left(\frac{p_{od}}{p_e}\right)^{\frac{\gamma - 1}{\gamma}} \tag{52}$$

$$M_d^2 = \frac{2}{\gamma - 1}\left(\frac{T_{od}}{T_d} - 1\right) \tag{53}$$

$$\sqrt{\frac{T_d}{T_e}} = \frac{\frac{M_d}{M_e}(1 - \Lambda_b)\frac{T_{oe}}{T_e} + \sqrt{\left[\frac{M_d}{M_e}(1 - \Lambda_b)\frac{T_{oe}}{T_e}\right]^2 + 4\frac{T_{od}}{T_d}\Lambda_b\frac{T_{oe}}{T_e}}}{2\left(\frac{T_{od}}{T_d}\right)} \tag{54}$$

$$\frac{U_d}{U_e} = \phi_d = \frac{M_d}{M_e}\sqrt{\frac{T_d}{T_e}} \tag{55}$$

The d streamline location, η_d, is determined by inverting the asymptotic velocity profile

$$\operatorname{erf} \eta_d = 2\phi_d - 1 \tag{56}$$

and then I_{1d}, the mass-flow integral, can be determined.

$$I_{1d} = \int_{-\infty}^{y_d} \frac{\phi\lambda}{\Lambda - C_e^2\phi^2}\, dy \tag{57}$$

Conservations of Mass, Momentum, and Energy

Mass Conservation. Mass-conservation principles give the following governing equation

$$\dot{m}_b + \dot{m}_\infty + \dot{m}_c = 0 \tag{58}$$

where $\dot{m}_\infty$ or $\dot{m}_c$ can be computed from Eq. 50 as shown below.

$$\dot{m}_\infty = \pm \int_{y_j}^{y_d} \rho u\, dy = \pm (\rho_e U_e)_\infty \int_{y_j}^{y_d} \frac{\rho u}{(\rho_e u_e)_\infty}\, dy$$

$$= \pm \frac{(\rho_e u_e)_\infty x_\infty}{\sigma_{2\infty}}\left(1 - C_{2a\infty}^2\right)\left(I_{1d\infty} - I_{1j\infty}\right) \tag{59}$$

and

$$\dot{m}_c = \pm \frac{(\rho_e u_e)_c x_c}{\sigma_{2c}} \left(1 - C_{2ac}^2\right)\left(I_{1d_c} - I_{1jc}\right) \tag{60}$$

where I_{1d} and I_{1j} are defined in Eq. 57 and 49, respectively.

Momentum Conservation. Since the momentum associated with the injection flow is very small (less than 4%, as compared with the main flow in all cold-flow test cases), it is neglected in the present analysis. Therefore, the momentum-conservation consideration is applied only to the free shear layer itself, as indicated in Eq. 49, to locate the separating streamline.

Energy Conservation. Two forms of energy transfer are associated with the jet mixing layer: one results from the total enthalpy gradient across the mixing layer, and the other results from mass-flow entrainment. Energy-conservation principles yield the following governing equation

$$q_b + \Sigma \Omega_c + \Sigma \Omega_d = 0 \tag{61}$$

where Ω_c is the shear work and heat transfer across the mixing layer

$$\Omega_c = \int_{y_j}^{y_e} \rho u \left(h_{oe} - h_o\right) dy \tag{62}$$

and Ω_d is the energy transfer by the entrained mass flow.

$$\Omega_d = \int_{y_j}^{y_d} \rho u \, h_o \, dy \tag{63}$$

The rate of heat transfer to the nozzle surface, q_b, has not been considered in the present study. Without knowing the q_b value, the energy equation cannot be solved directly, but it can be approximated by the following equation.

$$T_b \cong T_{ob} = \frac{1}{2}\left(T_{o\infty} + T_{oc}\right) \tag{64}$$

Since the energy transfer is not the important factor for TVC performance, the use of the above approximate equation should produce only a very small error, if any, in TVC effectiveness evaluation.

Computational Procedure

The analysis is carried out in the following manner:

1. A trial value of p_b is selected.

2. The inviscid-flow boundary for the external flow is computed using Prandtl-Meyer theory and iterating the value of the slipline angle until the recompression-pressure rises for both streams are equal.
3. Mixing-layer properties are computed.
4. Streamlines d and j are computed.
5. Mass entrainment is computed.
6. The mass-conservation equation is used, and an iteration is performed by varying p_b values until a converged solution is obtained.

PRESSURE DISTRIBUTION

As this study progressed, several cold-flow tests were conducted by Chandler Evans, Inc. in order to provide experimental guidelines for the analytical modeling of TVC-induced pressure distributions. Results of these tests were given in Ref. 19 and consist largely of internal pressure-distribution measurements. Some of the more important results are plotted in Fig. 23 through 32. In these figures, the average pressure is defined as the average of pressures along the circumferential direction, while the centerline pressure is the pressure along the geometric centerline or along the row closest to the geometric centerline for the port-side quadrant. The following processes were performed using these data.

1. Pressure at the port-side separation point, p_p, was determined from Fig. 3, and the axial separation location was determined from pp using isentropic relations between p and A for nozzle flows.
2. For the cold-flow tests, plateau pressure on the port side, p_b, was assumed to be the ambient pressure, p_∞. Note that p_b becomes lower than p_∞ near the end of the nozzle for high p_{oc} cases, which is probably due to the large ambient-flow feedback effect. For simplicity, $p_b \cong p_\infty$ is still a good approximation. For conditions with ambient flow, p_b was obtained from the two-stream mixing analysis as discussed previously. The distance between the location where p_p exists and that where p_b exists is called the "pressure recovery distance," ℓ_r. Its determination requires detailed information about the boundary-layer characteristics at the separation point. Since this information was not available from the cold-flow tests, it was estimated, using available literature, to be 1 inch, or approximately 20 to 30% of the total separation-layer length for these cold-flow tests.
3. Pressure at the attached-side separation point, p_a, was determined from Fig. 15, and the axial location was again determined from the isentropic relations. The pressure

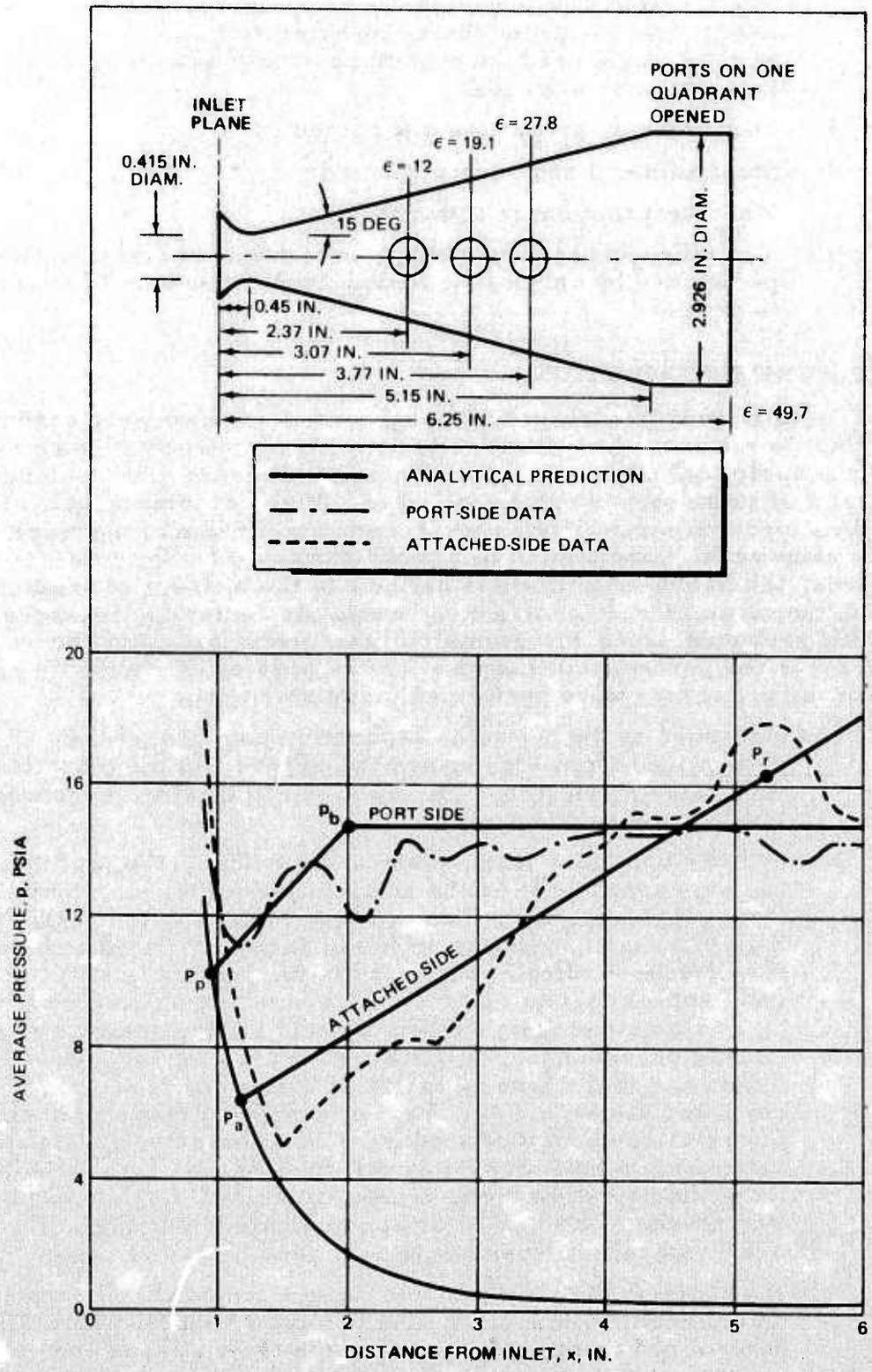

FIG. 23. Average Pressure in CEN-17 Nozzle at p_{oc} = 200 psig.

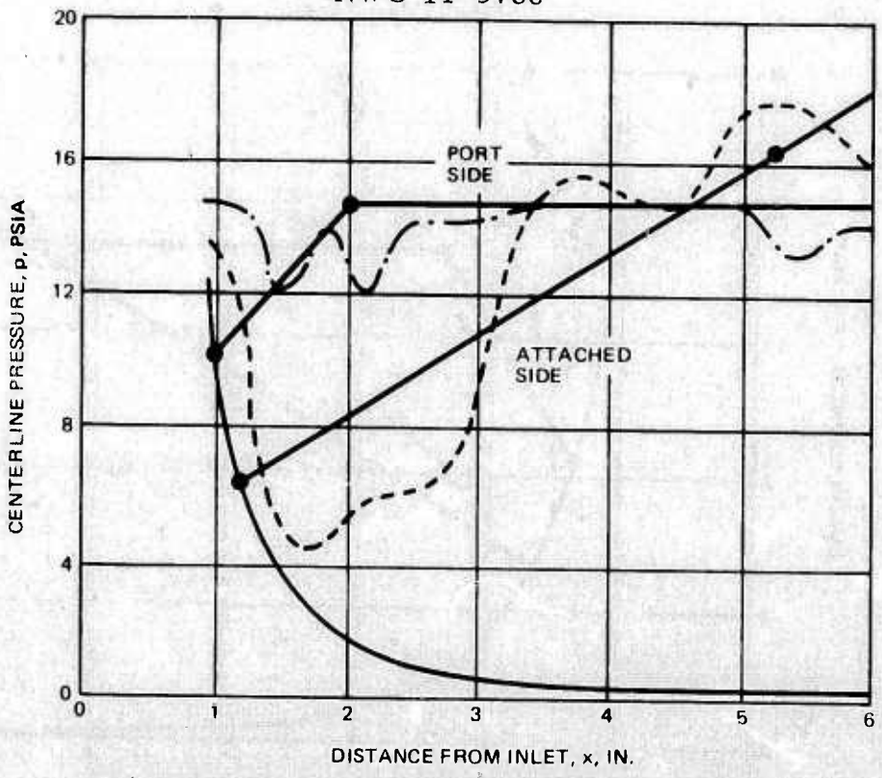

FIG. 24. Centerline Pressure in CEN-17 Nozzle at p_{oc} = 200 psig.

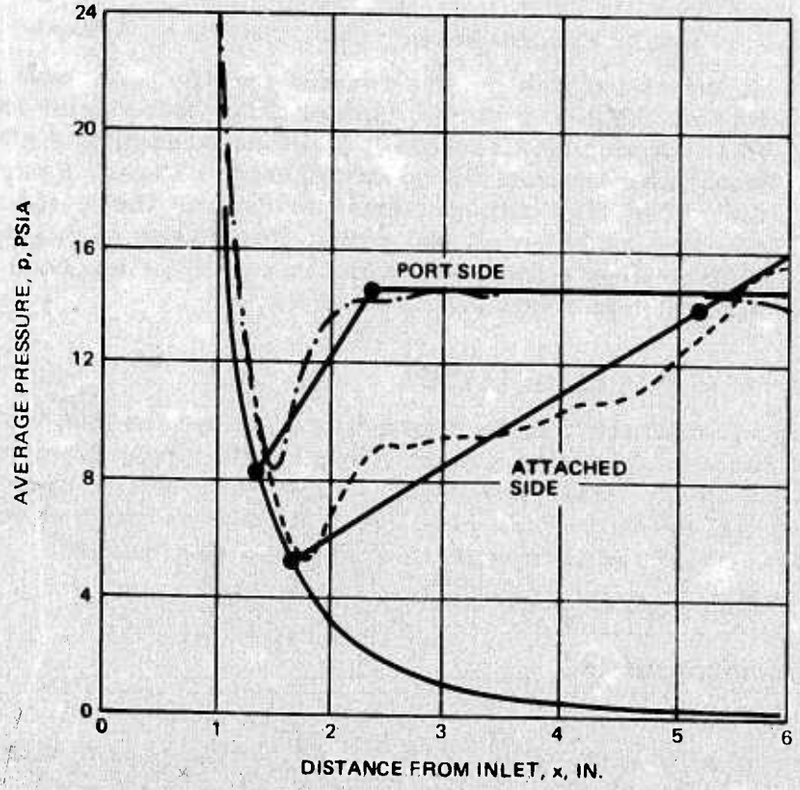

FIG. 25. Average Pressure in CEN-17 Nozzle at p_{oc} = 400 psig.

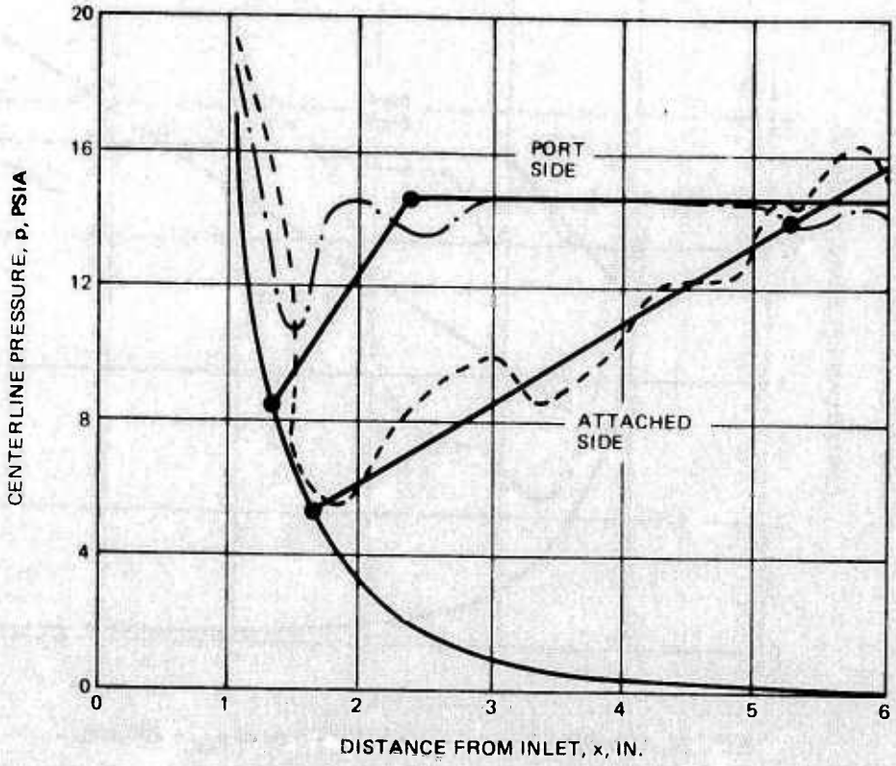

FIG. 26. Centerline Pressure in CEN-17 Nozzle at p_{oc} = 400 psig.

at the end of the nozzle conical section, p_r, was computed by the method described under Flow Reattachment Process in the preceding section. A linear pressure distribution was assumed for the no-attachment cases. From the available cold-flow experimental evidence, these cases occur for p_{oc} values below 1,000 psig. For cases of $p_{oc} \geq 1,000$ psig, p_r was also computed as in the previous section. p_a was determined from Fig. 15 and 17.

SIDE-FORCE DETERMINATION

Having obtained the pressure-distribution shapes, as shown in Fig. 23 through 32, it is now possible to integrate them to obtain the side force under TVC conditions. To do this, some basic derivations of functional relations are required. Using the control volume shown in Fig. 33, an overall momentum equation is obtained.

$$\Sigma F = \dot{m}(V_2 - V_1) = \rho_1 V_1 A_1 (V_2 - V_1) \tag{65}$$

The X-component is

$$p_1 A_1 - p_2 A_2 + \int_1^2 p\,dA_{wx} - \int_1^2 \tau_w\,dA_{wx} = \rho_1 V_1 A_1 (V_{2x} - V_1)$$

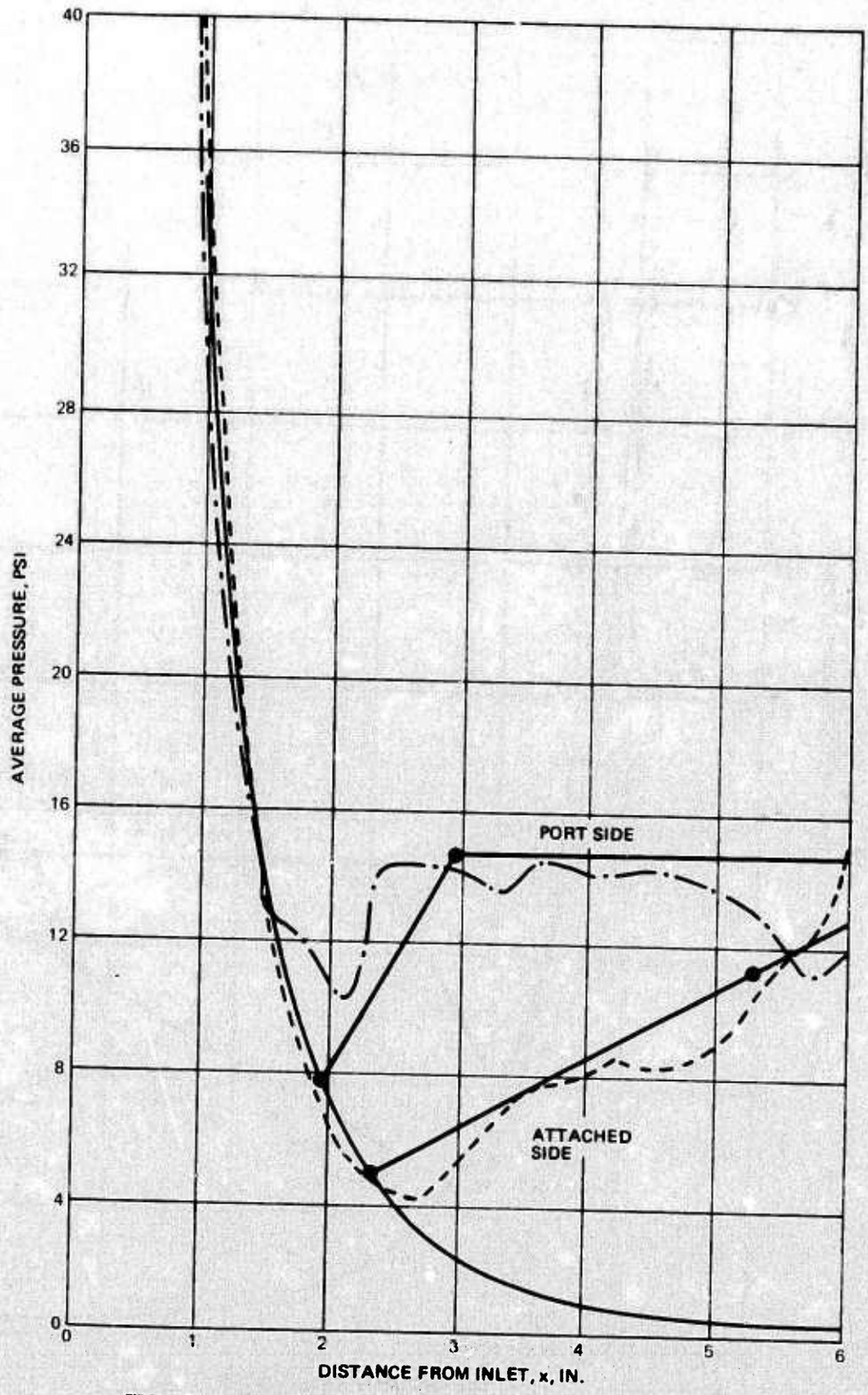

FIG. 27. Average Pressure in CEN-17 Nozzle at p_{oc} = 800 psig.

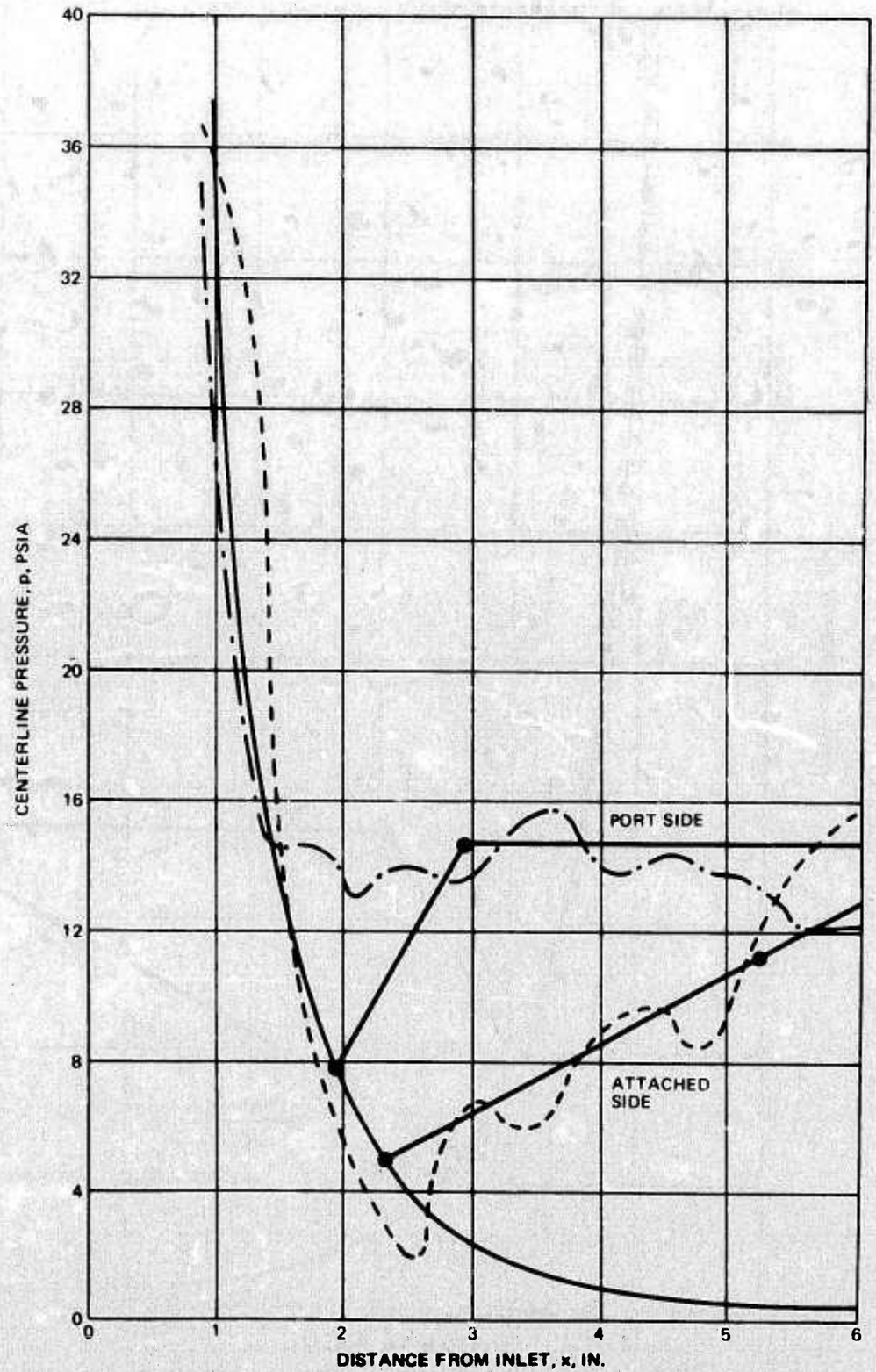

FIG. 28. Centerline Pressure in CEN-17 Nozzle at p_{oc} = 800 psig.

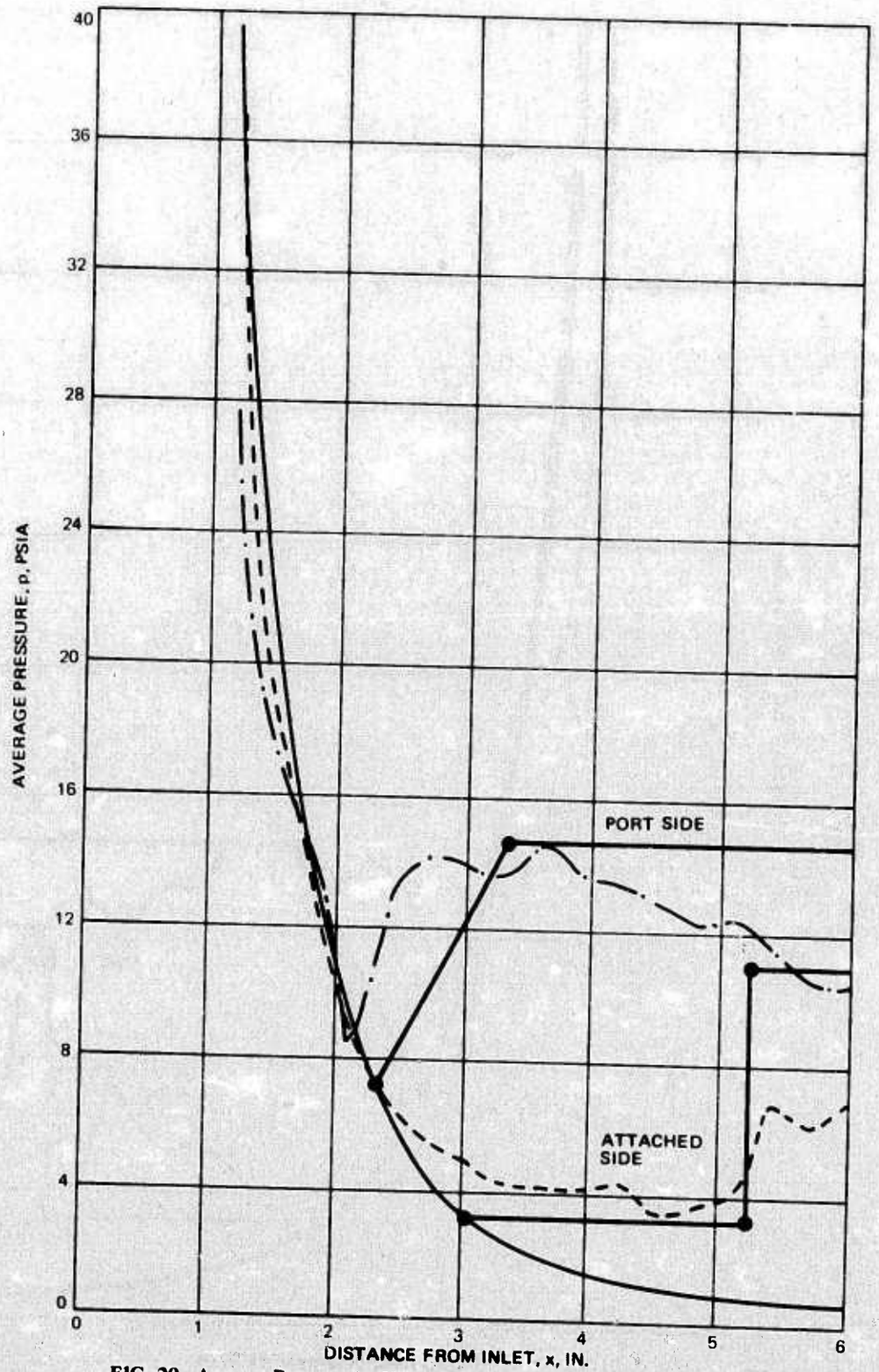

FIG. 29. Average Pressure in CEN-17 Nozzle at p_{oc} = 1,200 psig.

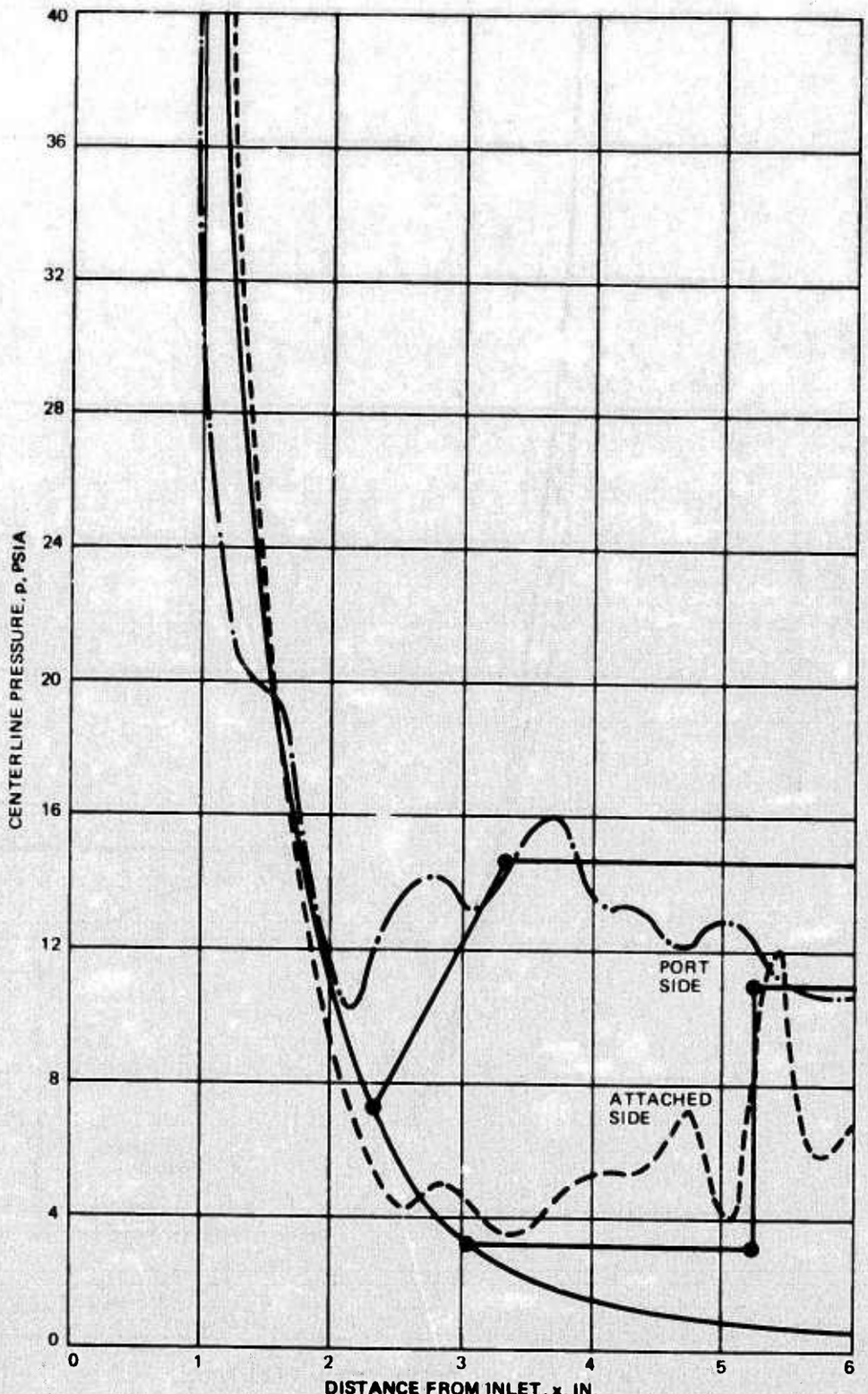

FIG. 30. Centerline Pressure in CEN-17 Nozzle at p_{oc} = 1,200 psig.

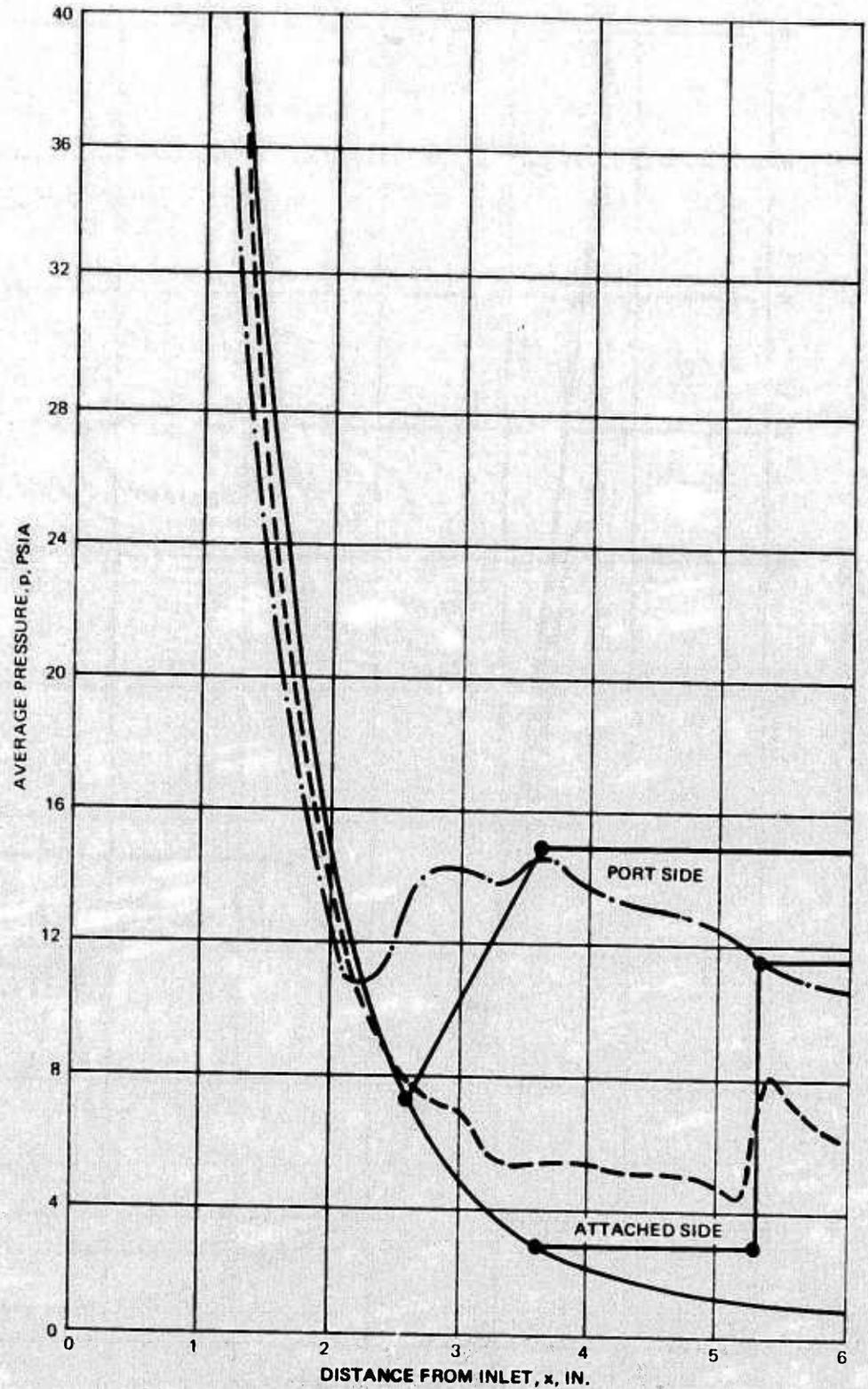

FIG. 31. Average Pressure in CEN-17 Nozzle at p_{oc} = 1,600 psig.

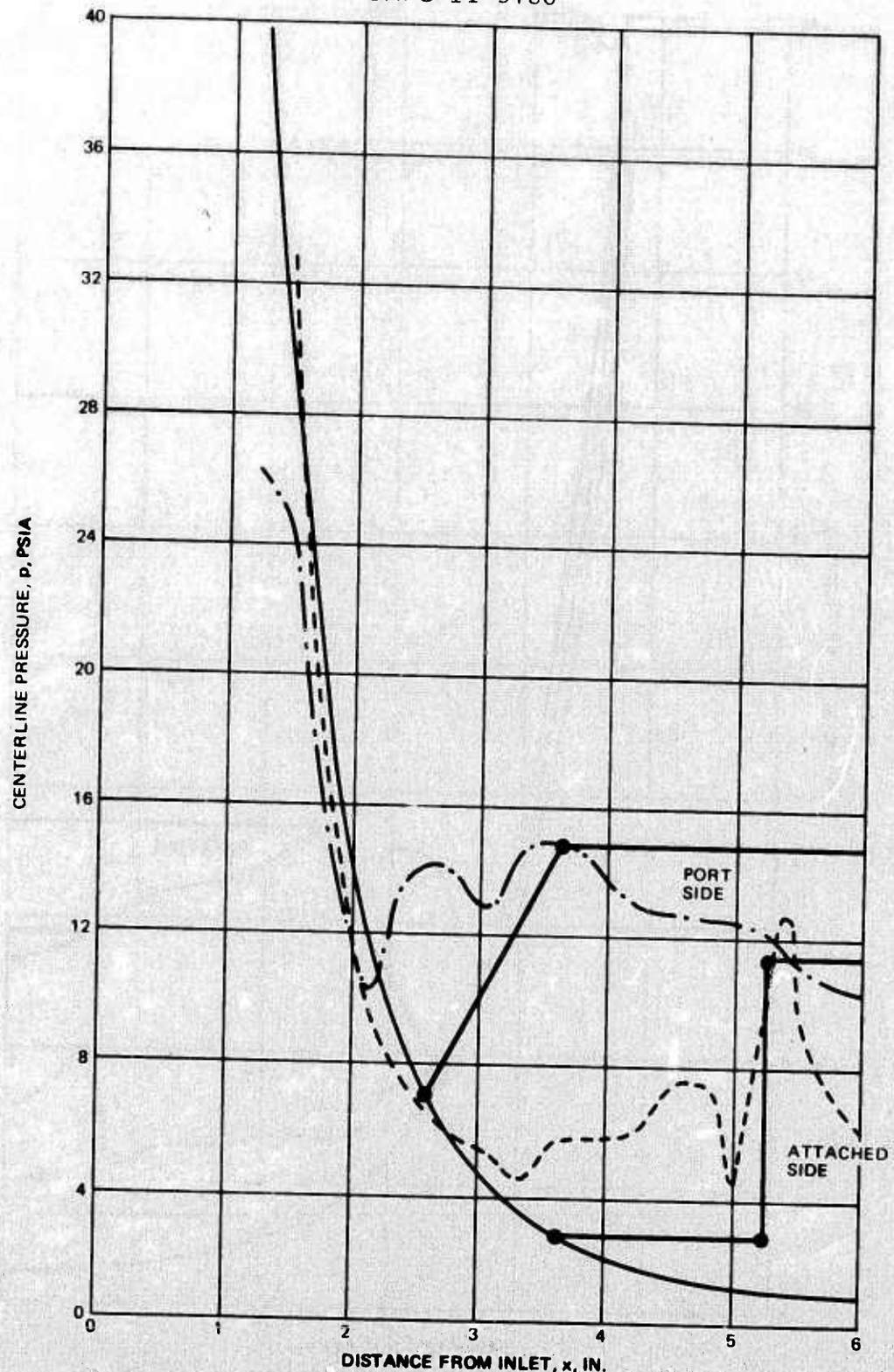

FIG. 32. Centerline Pressure in CEN-17 Nozzle at p_{oc} = 1,600 psig.

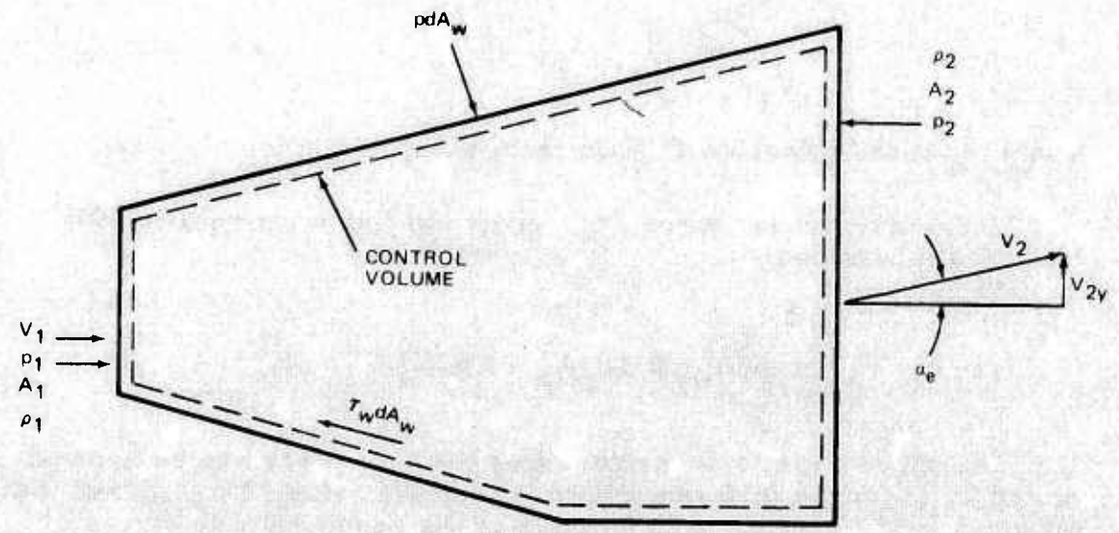

FIG. 33. Control Volume for Side-Force Determination.

where

$$\int_1^2 p dA_{wx} - \int_1^2 \tau_W dA_{wx} = F_x \equiv \text{X-component of force of walls on the fluid}$$

or

$$F_x = \left[(\rho_1 V_1 A_1)\, V_{2x} + p_2 A_2\right] - \left[\rho_1 V_1^2 A_1 + p_1 A_1\right] \qquad (66)$$

The Y-component is:

$$\int_1^2 p dA_{wy} - \int_1^2 \tau_w dA_{wy} = (\rho_1 V_1 A_1)\, V_{2y}$$

where

$$\int_1^2 p dA_{wy} - \int_1^2 \tau_w dA_{wy} = F_y \equiv \text{Y-component of force of walls on the fluid}$$

or

$$F_y = (\rho_1 V_1 A_1) V_2 \sin \alpha_e$$

where α_e is the effective TVC deflection angle.

Ignoring the shear force, τ_w, gives the following equation for BLTVC applications:

$$F_y = \int_1^2 p dA_{wy} \cong \Sigma p_p A_p - \Sigma p_a A_a \tag{67}$$

The above equation considers that the side force can be approximated by the force difference between the port side, $\Sigma p_p A_p$, and the attached side, $\Sigma p_a A_a$. Computation of the resulting side forces, which are shown in Fig. 34, used only one projected quadrant area for both A_p and A_a. Considering the complexity of the problem, the results are considered to compare well with experimental data. The agreement above also holds for the data-correlation curve for p_{oc} = 1,100 psig, although the pressure distributions given in Fig. 35 were constructed entirely with the analytical methods discussed earlier.

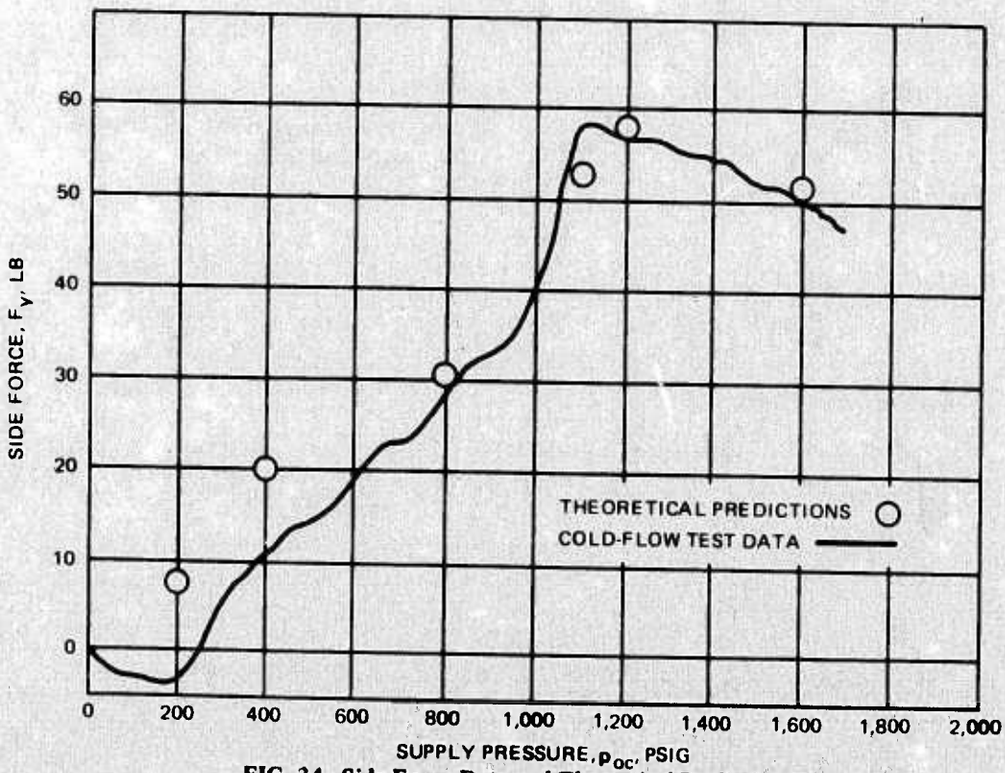

FIG. 34. Side-Force Data and Theoretical Predictions.

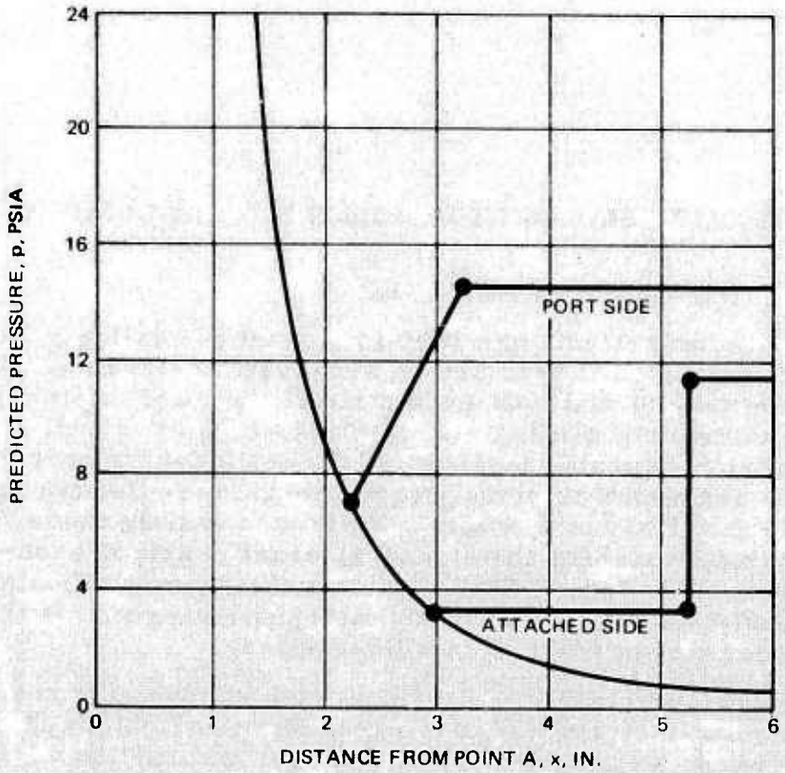

FIG. 35. Wall Static-Pressure Predictions for CEN-17 Nozzle at p_{oc} = 1,100 psig.

SIMILARITY PARAMETER AND NOZZLE DESIGN GUIDELINES

BLTVC SIMILARITY PARAMETER, $\mathcal{E}$

Simulation criteria are very important in scaling a BLTVC system that is to be tested in a combined aerodynamic-thruster environment. It is necessary to maintain geometric scaling and jet-plume-to-free-stream momentum scaling, to match Mach number and, where possible, to match Reynolds number for general aerodynamic similarity. It is also necessary to closely approximate the effective specific-heat ratio of the actual main nozzle. Failure to satisfy these requirements will preclude matching the crucial internal nozzle pressure distribution. In addition, it is desirable to duplicate the energy-diffusing parameter, $\tau = (T_o/\mathcal{M})_j/(T_o/\mathcal{M})_c$, where $\mathcal{M}$ = molecular weight, for the simulation of the external jet/free-stream interaction.

In addition to the considerations noted above, the results of the present study indicate that it is necessary to simulate an additional parameter, $\mathcal{E}$, to account for the TVC gas interaction with the nozzle main flow. $\mathcal{E}$ is a two-stream mixing-energy parameter that is a function of control-port mass-flow rate, nozzle mass-flow rate, nozzle total temperature, nozzle molecular weight, missile recovery temperature, and air molecular weight.

Two-Stream Mixing Considerations

One method of extending conventional wind-tunnel simulation requirements to flows involving two fluid streams is to require, in addition, that the ratios of all relevant reference quantities of the two streams be matched, and that dimensionless mass and energy parameters be included in the list of similarity variables. Since free-shear layers are nearly always turbulent at Reynolds numbers of practical interest, transport by molecular diffusion and conduction at the shear layer may be neglected, and the only molecular transport properties that must be included are those that influence the vehicle boundary layer, such as the mass and energy properties of the control injectant.

Temperature Effects. The simulation of temperature effects can be satisfied by matching the specific-heat ratio value and the injectant's mass, momentum, and energy fluxes normalized with respect to the corresponding quantity of the nozzle flow as shown below.

For mass,

$$\eta_m = \frac{(\rho v A)_j}{(\rho u A)_c}$$

For momentum,

$$\Theta = \frac{(p\gamma M^2 A)_j}{(p\gamma M^2 A)_c}$$

For energy

$$\mathcal{E} = \mathcal{M} \frac{(c_p T_o)_j}{(c_p T_o)_c}$$

where $c_p = (\gamma/\gamma - 1)R$ and R is the gas constant. Subscript j refers to the TVC control-port injectant, and subscript c refers to the nozzle flow at the separation point.

It is interesting to note that the energy parameter can be reduced to the well-known jet-interaction parameter, τ, by the following procedure:

$$\mathcal{E} = \mathcal{M} \frac{(c_p T_o)_j}{(c_p T_o)_c}$$

When the mass-flow ratio is duplicated in the test,

$$\mathcal{E} \rightarrow \frac{(c_p T_o)_j}{(c_p T_o)_c} = \frac{\left(\frac{\gamma}{\gamma-1} R T_o\right)_j}{\left(\frac{\gamma}{\gamma-1} R T_o\right)_c}$$

When γ is also duplicated in the test,

$$\mathcal{E} \rightarrow \frac{(R T_o)_j}{(R T_o)_c} = \frac{\left(\frac{T_o}{\mathcal{M}}\right)_j}{\left(\frac{T_o}{\mathcal{M}}\right)_c} \equiv \tau$$

where $\mathcal{M}$ is the molecular weight.

Therefore, it is clear that unless the mass-flow parameter, $\mathcal{M}$, and the specific heat ratio, γ, are duplicated, matching of the jet interaction parameter, τ, alone may not entirely satisfy the energy simulation. Also, the choice of $\mathcal{E}$ over τ for BLTVC simulation is obvious due to its generality. Independent of the magnitude of the temperature effect on TVC performance, the energy simulation should be preserved because of potential effects on other related considerations, such as heat transfer or motor thrust performance.

Typical $\mathcal{E}$ values for Chandler Evans cold-flow and NWC rocket static tests are shown in Fig. 36. Values of $\mathcal{M}$ used for computing $\mathcal{E}$ are given in Fig. 37. It can be seen in Fig. 37 that the momentum ratio of the injectant to the nozzle flow, Θ, is very small. Therefore, the BLTVC does not appear to involve a dominantly strong lateral-jet type of flow interaction under static-jet conditions.

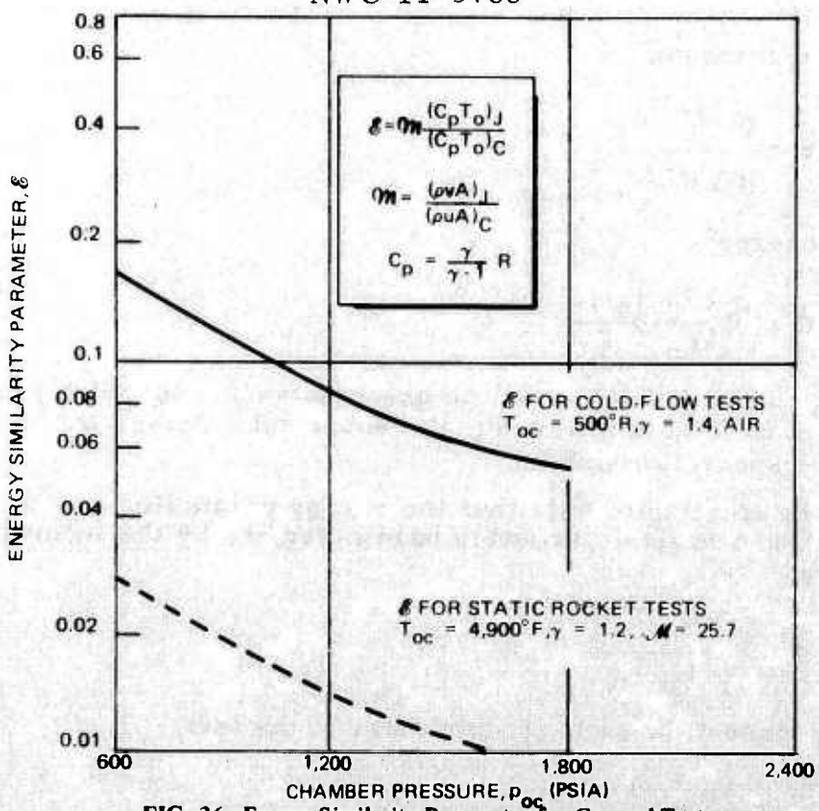

FIG. 36. Energy Similarity Parameter for Ground Tests.

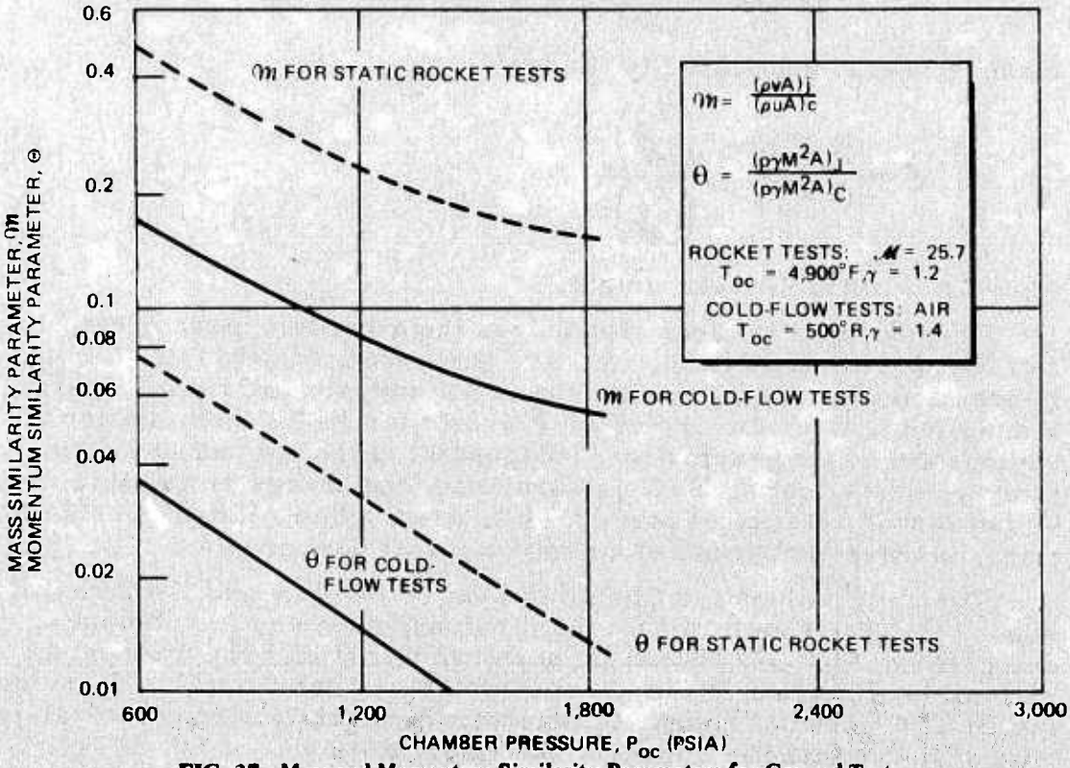

FIG. 37. Mass and Momentum Similarity Parameters for Ground Tests.

Both Fig. 36 and Fig. 37 are based on the BLTVC nozzle configurations given in Fig. 38 and Fig. 39.

Observed BLTVC Performance. TVC performance under representative hot- and cold-flow conditions for similar nozzle configurations is shown in Fig. 40. The difference in side force (or angular deflection) for cold-flow and solid-propellant rocket static tests over a range of chamber pressures appears to be significant. Therefore, the hot-gas effects such as temperature, erosion, particle deposition, etc., on BLTVC performance must be considered.

As anticipated, the largest effect appears to be that of mass addition, which serves as a triggering device. An increase in the injection mass does not always improve BLTVC effectiveness at a given p_{oc} value, as can be seen in Fig. 41. When the port size drops from 5/8- to 3/8-inch diameter, the injection flow area is reduced by a factor of about 3, while the drop in side force is of a lesser order. This may explain the fact that η_{II} for cold-flow and rocket static tests can vary by a significant factor, as shown in Fig. 37, but the difference in side force may not vary correspondingly. Therefore, it is concluded that the energy parameter, ϵ, should be used for BLTVC simulations.

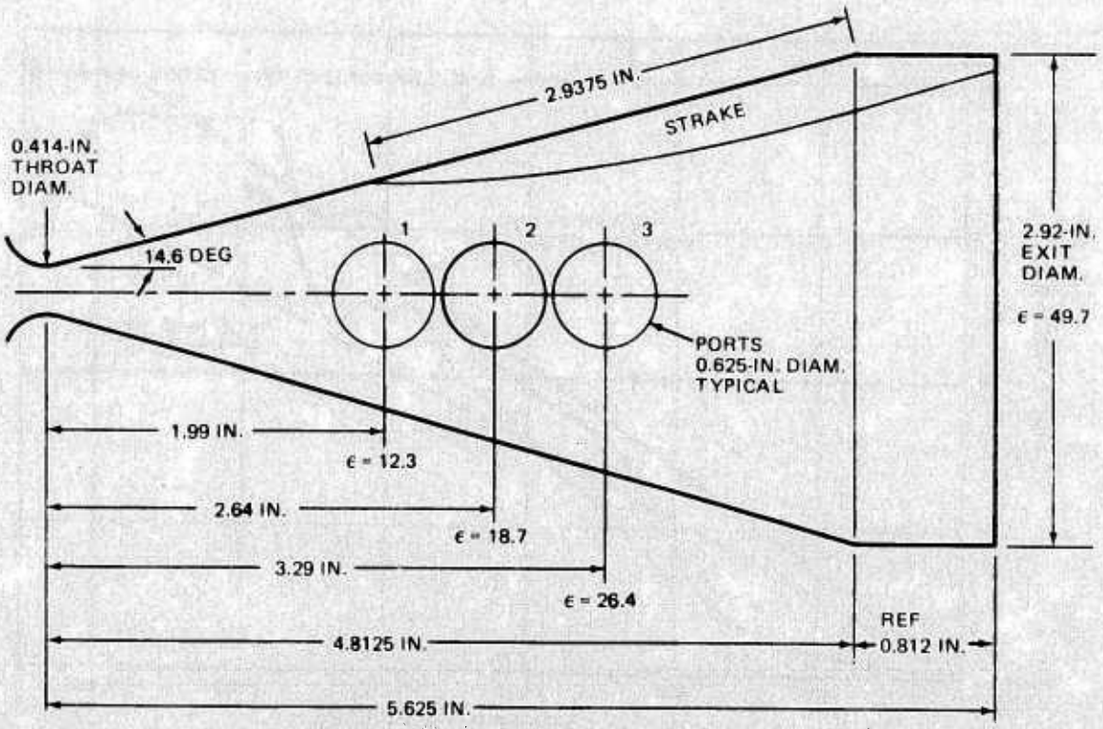

FIG. 38. Chandler-Evans Cold-Flow Test-Nozzle Configuration.

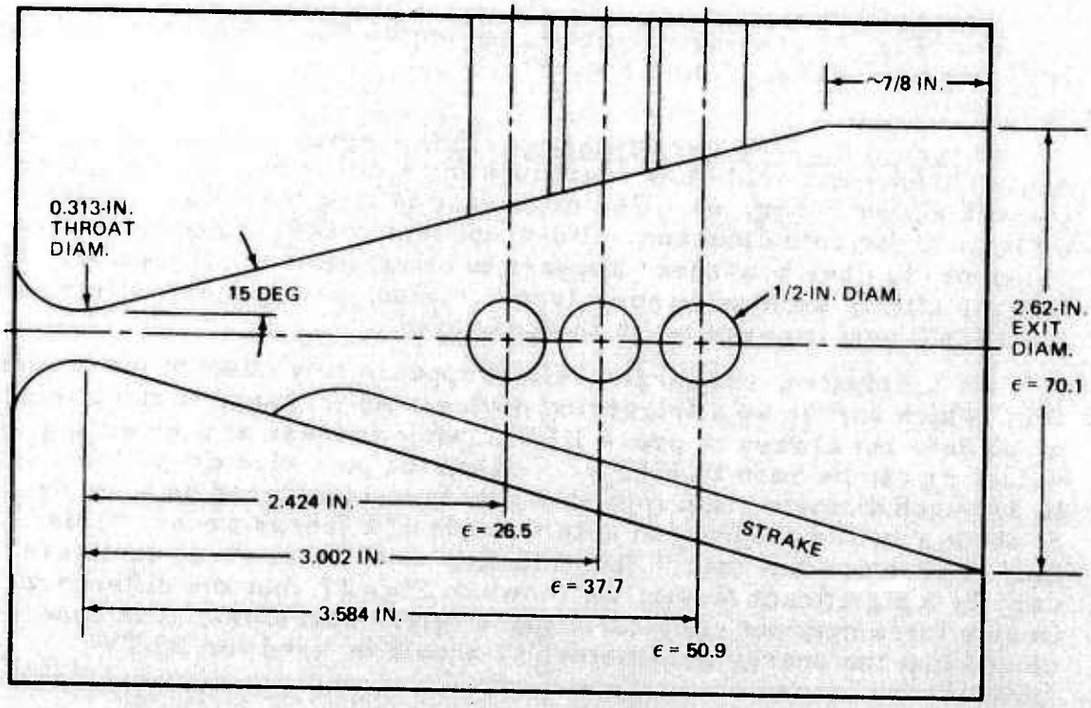

FIG. 39. NWC Rocket-Test Nozzle Configuration.

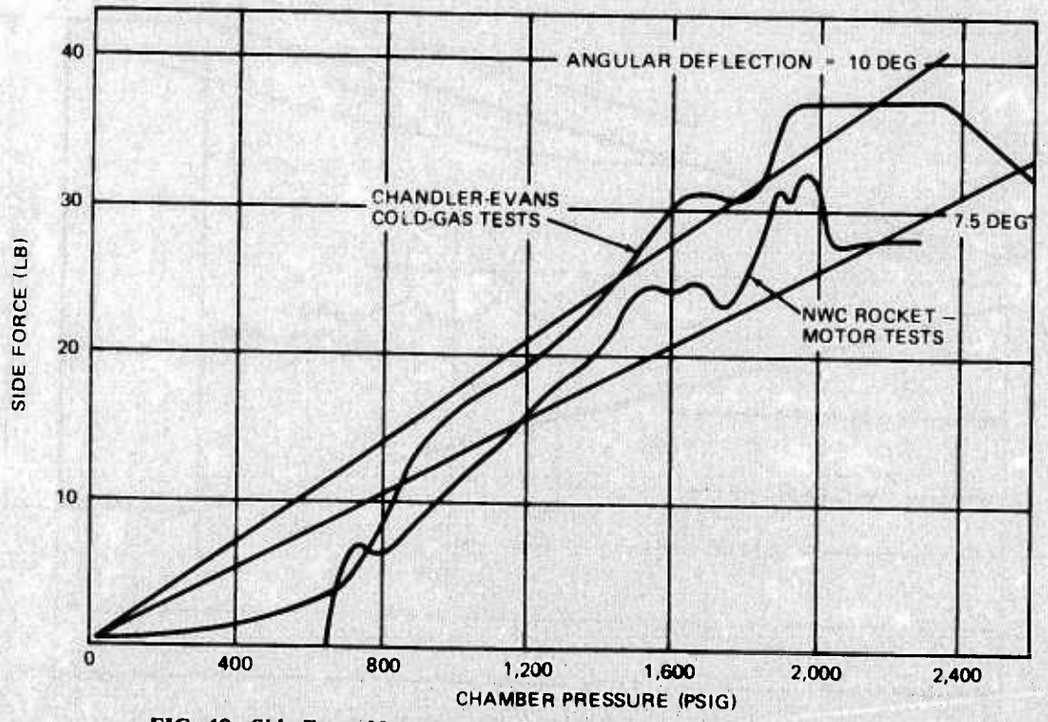

FIG. 40. Side-Force Measurements From Some Typical Cold-Flow and Rocket Static Tests.

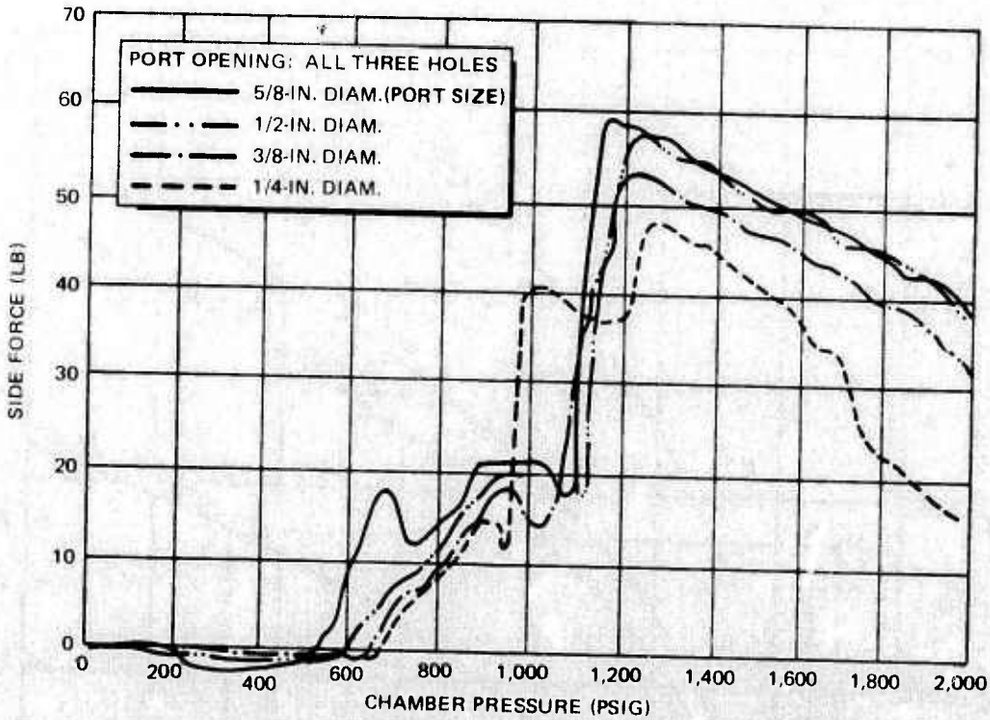

FIG. 41. Effect of Mass Addition on BLTVC Effectiveness (Cold-Flow Test Results).

NOZZLE DESIGN GUIDELINES

Guidelines for determining port locations and sizes in the design of a BLTVC nozzle are a necessary adjunct to empirical data on operation under various conditions. For example, suppose a cold-flow thrust-deflection angle of 15 degrees has been achieved with p_{oc} = 2,500 psia, ϵ = 50, and γ = 1.4. The question is how to obtain similar performance with hot gas if the operating conditions are p_{oc} = 1,600 psia, ϵ = 50, and γ = 1.2. In the present study, a preliminary design guideline was developed and is outlined below.

Port Location Determination

Construct two curves, p_{oc}/p_∞ versus ϵ_s for the two cases of interest. In Fig. 42, these have been shown as dashed lines and solid lines for two different operating cases. For each case, conditions are needed both with and without TVC. These conditions may be obtained as described in the Separation Point section.

Construct operating boundaries such as A'B'C'D' and abcd according to the p_{oc} limits shown on the right-hand scale of Fig. 42.

Locate the ports as shown in the lower portion for CEN-17, ϵ = 50 within the boundary of A'D'. Similar TVC performance could be achieved for hot-gas conditions if port locations were within the boundary of ad, as is also shown for ϵ = 50.

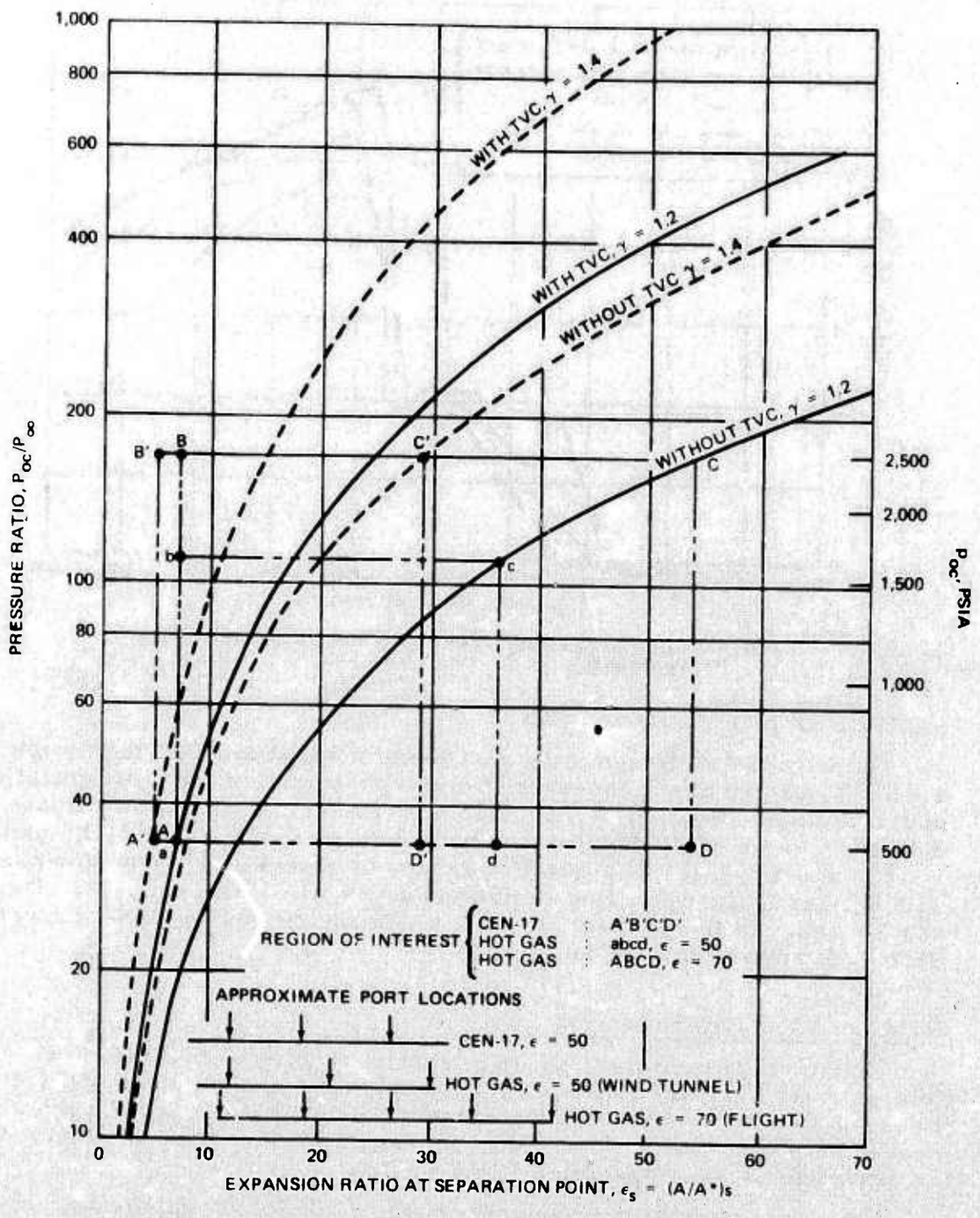

FIG. 42. Nozzle Design Auxiliary Chart – Port Locations.

If $\epsilon = 70$ is required because the operating pressure is being raised to $p_{oc} = 2,500$ psia and the boundary is consequently being changed to aD, a five-port design is then required to achieve similar performance because the operating boundary (ABCD) is larger. Typical port locations are also shown for $\epsilon = 70$.

Port Sizes

Port sizes can be determined according to the BLTVC similarity parameter, as discussed in detail earlier in this section.

Operating p_{oc} Range

It is desirable to select a lower p_{oc} range (500 to 1,600 psia) for wind-tunnel tests because a higher pressure exists at the separation point, p_{sep} (see Fig. 43) and because a shorter nozzle such as $\epsilon = 50$ (see Fig. 42) can be used. Depending on mission requirements, it may be desirable to select a high p_{oc} range (500 to 2,500 psia) for flight because a higher thrust level results, and longer operating times are experienced.

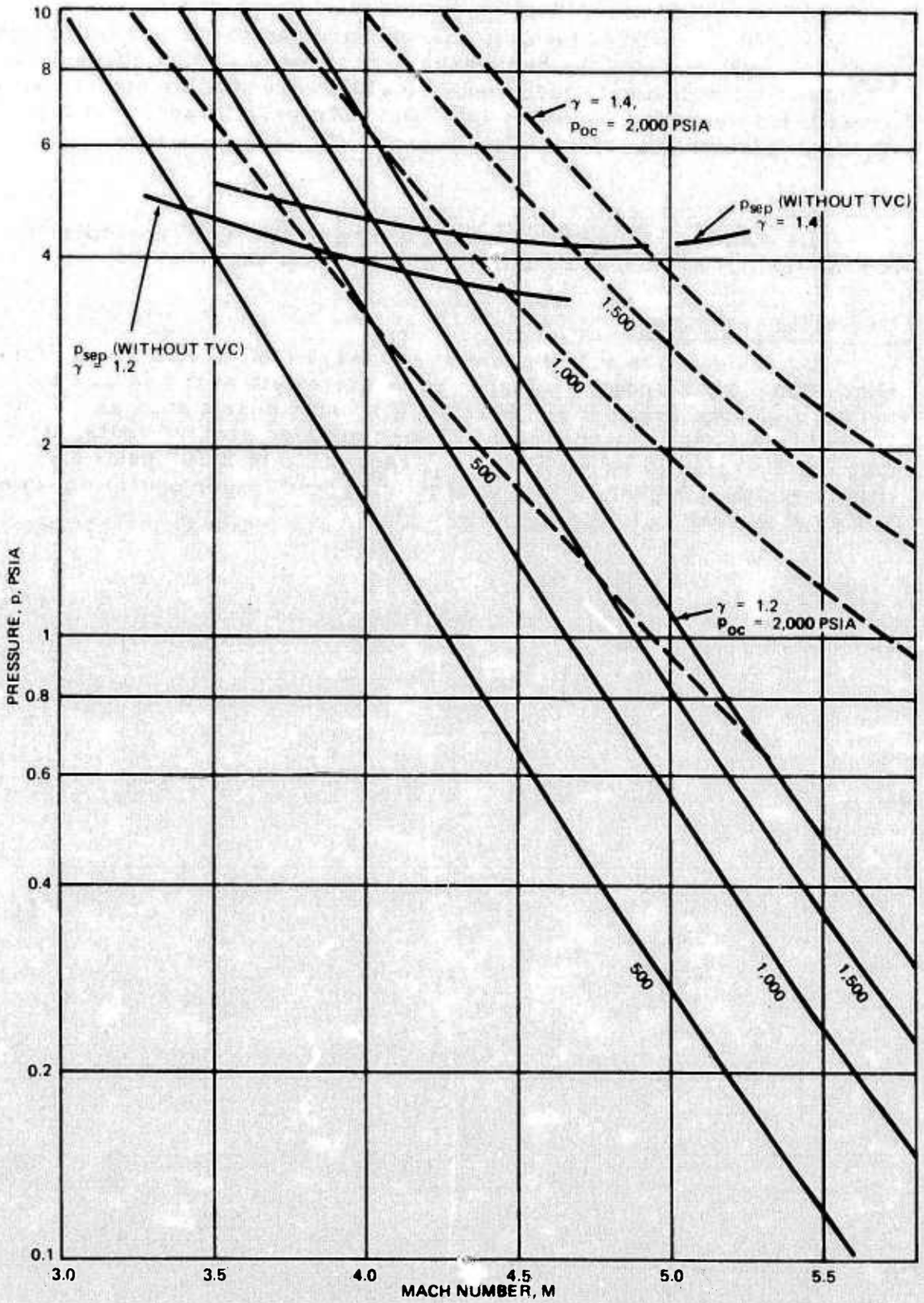

FIG. 43. Nozzle Design Auxiliary Chart – Separation Pressure.

CONCLUSIONS AND RECOMMENDATIONS

A key objective of this study was to provide analytical tools to assist in a largely empirical BLTVC design process. This has been achieved through quantification of the influence of dominant BLTVC flow-field phenomena. Significant conclusions regarding the generation of control forces are given below.

High side force can be achieved by properly choosing parameters that control the port-side and the attached-side separated flows. For the port side, early separation is desirable. For the attached side, reattachment near the nozzle aft end is desired. It is extremely important that the flow reattach on the attached side so as to maintain a much lower pressure there than on the port side. Reattachment provides a shield to prevent back-pressure feedback, which results in higher pressure, as usually observed on the port side. The cylindrical aft body provides a good mechanism to ensure an attached flow on the attached side. However, for lower chamber pressures, say $p_{oc} < 1,000$ psia, the flow does not attach, even with a cylindrical section. Additional work to investigate desirable aft-section geometry for low p_{oc} values is recommended.

Study of the separation-point locations and sizes has provided a clearer understanding of how the TVC gas interacts with the nozzle flow and has helped to provide a useful guideline for BLTVC nozzle design and a method for locating the TVC ports. The first port should be placed at or slightly downstream of the separation point without TVC. Failure to do this will result in lower side force values, as shown in Fig. 44 and 45. Other effects of port location are shown in Fig. 46. The effect of port size was discussed in the section on flow-field models and is shown in Fig. 41. The internal strakes used in some designs to obtain a two-dimensional-type flow have pronounced effects on the flow-field disturbance and consequently on the resulting side-force value. As can be seen from Ref. 19, very large, nonuniform pressures exist in the vicinity of the strake leading edge. Thus, small changes in location are important. The sensitivity of the leading-edge location may become even more critical in hot-gas tests because of the deposit of exhaust products on the strake leading-edge surfaces. Hence, in general, the position of the strake leading edge should be further downstream for hot-gas tests than for cold-flow tests. The shape and location of the strake leading-edge effect should be studied further, both analytically and experimentally.

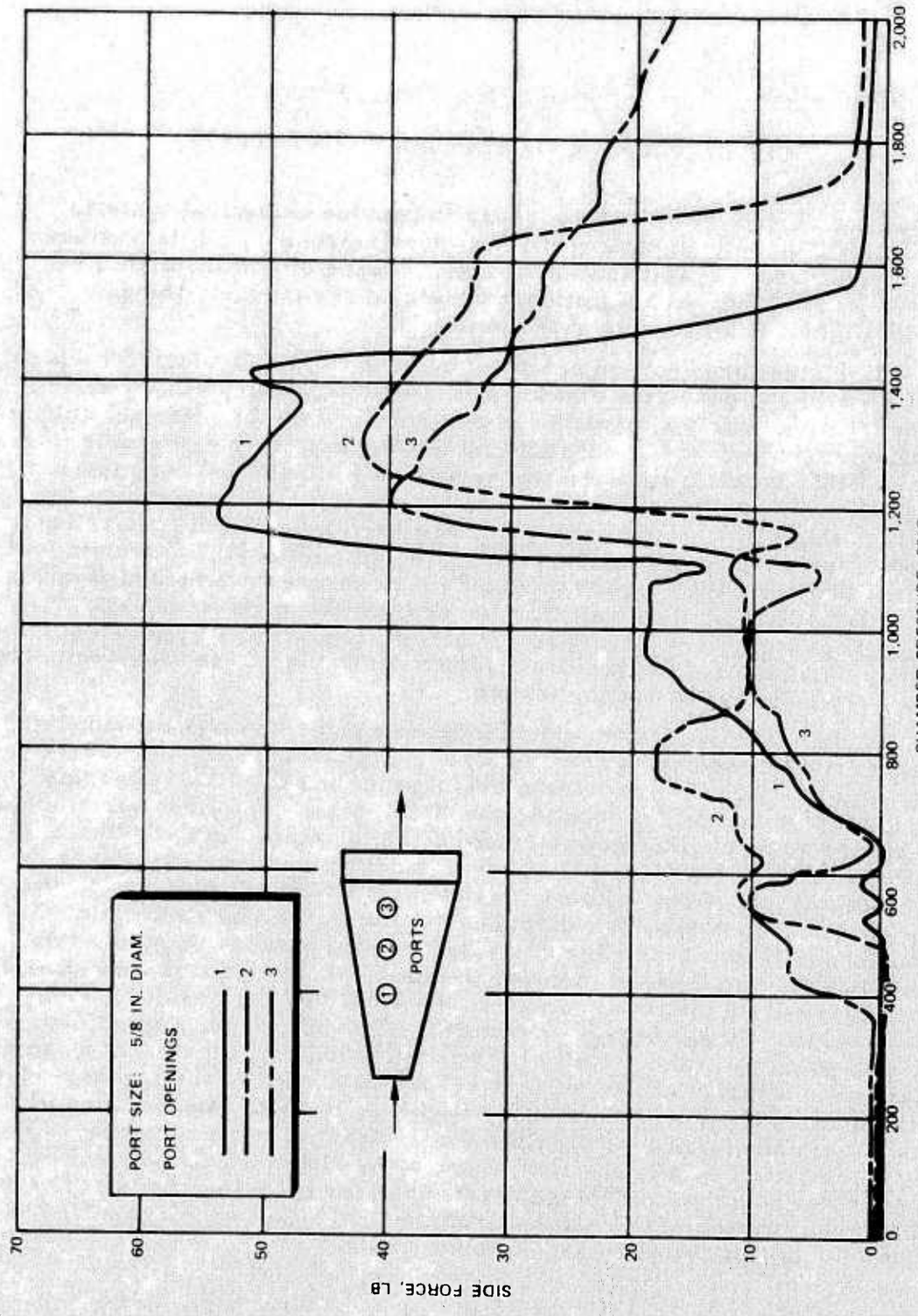

FIG. 44. Cold-Flow Test Results – One Port in One Row With Strakes.

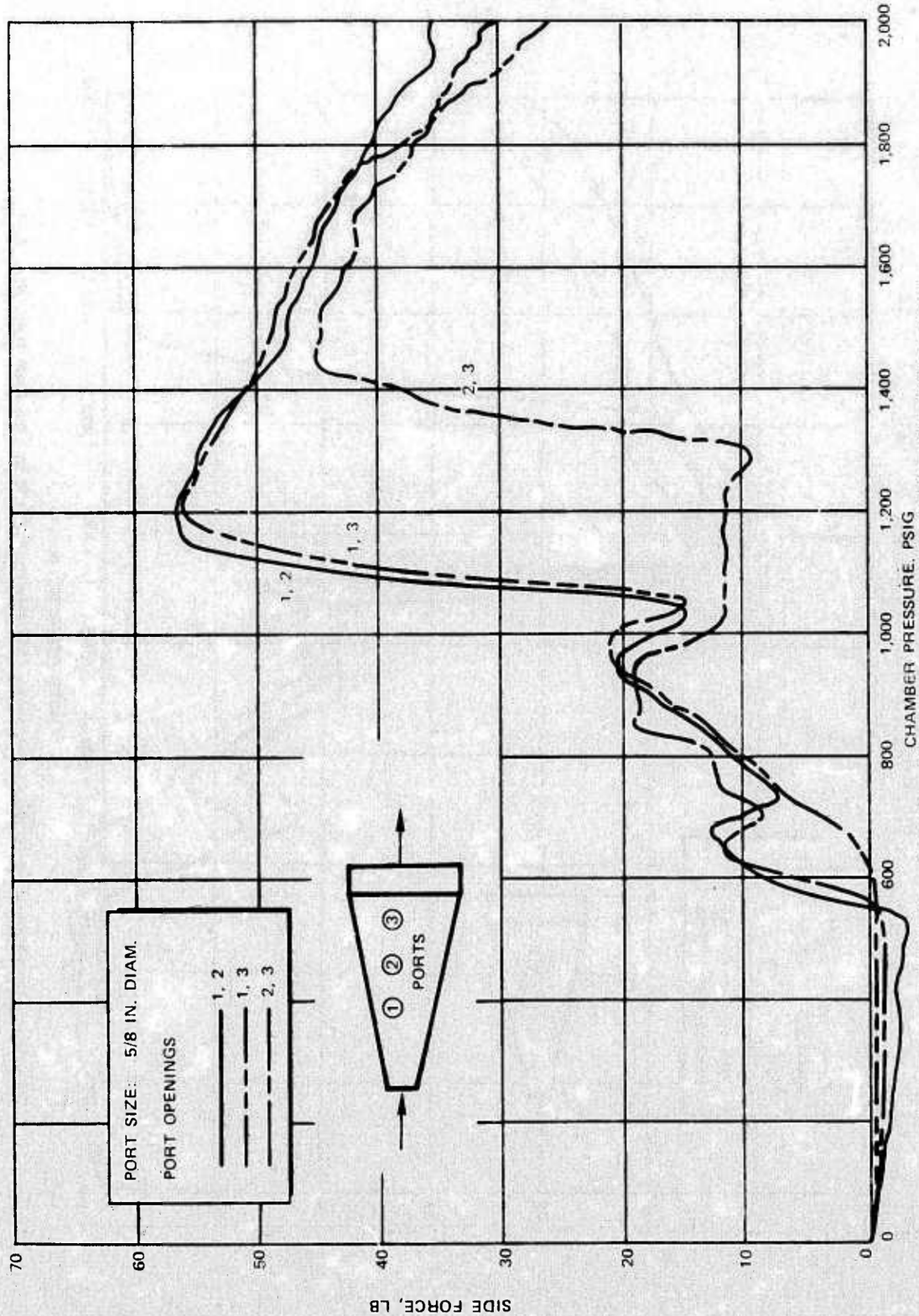

FIG. 45. Cold-Flow Test Results – Two Ports in One Row With Strakes.

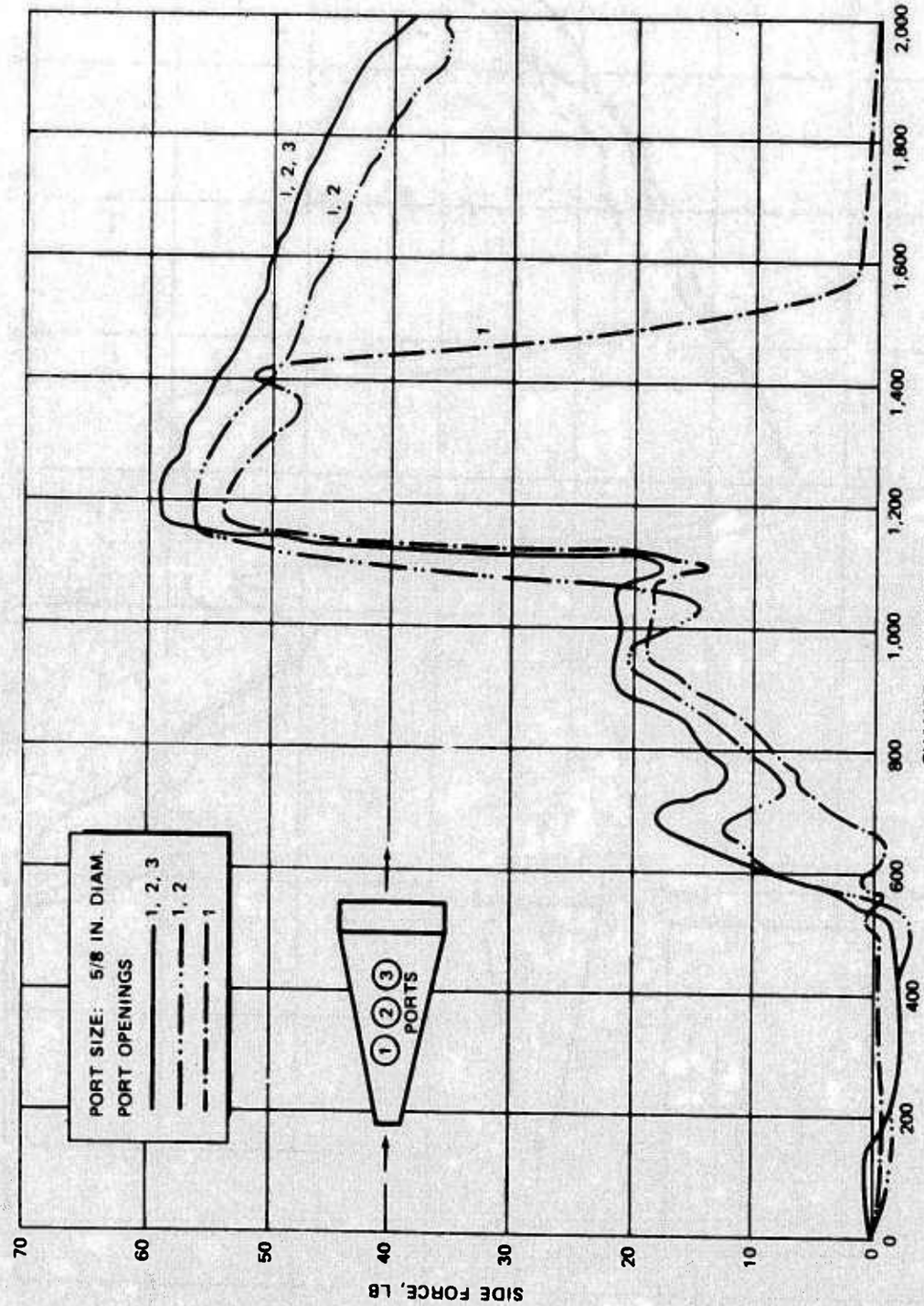

FIG. 46. Cold-Flow Test Results – Various Combinations of Ports in One Row With Strakes.

There is a significant difference between cold-flow or static rocket tests and wind-tunnel or flight tests. As discussed in detail in the section on flow-field conditions, the ambient flow will reduce the flow feedback effect, which may lower the pressure on the port side — but the ambient flow will also help flow reattachment on the attached side. Consequently, higher side force may occur with lower p_{oc} values, as compared to the same p_{oc} values in cold-flow tests. Therefore, the need for a cylindrical aft section is probably less, as compared to cold-flow tests. With higher p_{oc} values, lower side forces probably will be observed in wind-tunnel and flight tests. This should be kept in mind in designing a BLTVC system for flight environments. The combined effects of ambient flow, altitude, and the high temperature of nozzle flow can best be evaluated experimentally. Analytical study should be considered for optimizing overall performance for all parameters involved.

The present study represents the first analytical attempt to provide a method for BLTVC performance prediction, and cursory assumptions were used when needed. It is strongly recommended that further analytical efforts be conducted to improve the analytical methodology and the prediction of BLTVC performance in flight environments.

Appendix
AUXILIARY CHARTS AND THEIR USES

Subroutines from an existing McDonnell Douglas computer program for separated and base flows were used in the work covered by this report in order to obtain numerical flow-field solutions. Specifically, these subroutines were assembled to predict local flow-field solutions for a large variation of flow parameters such as M_c, T_{oc}, p_{oc}, γ_c, M_∞, $T_{o\infty}$, γ_∞, and port size. Thirty-six charts (Fig. 47 through 82) were constructed to treat the following parametric variations:

M_c (at separation point) = 3.5, 4, and 4.5

T_{oc} = 3,000, 4,000, and 5,500°R

γ_e = 1.2

M_∞ = 1.2 and 2

$T_{o\infty}$ = 500°R

γ_∞ = 1.4

p_∞/p_c = 3, 4, 6, and 8

$\dot{m}/\rho_c u_c$ = 0 to 0.2

Figures 47 through 55 present p_b/p_∞ as a function of $\dot{m}/\rho_c u_c$. Since p_b/p_∞ is an implicit function of $\dot{m}/\rho_c u_c$, iteration is needed to obtain a solution.

A typical computational procedure that uses these charts is outlined as follows:

1. Based on given p_∞/p_{oc}, γ_c, and nozzle half-angle values, determine $(A/A^*)_c$ at the separation point.
2. Compute p_c, $\dot{m}_c$, ρ_c, u_c, and p_∞/p_c values based on the value of $(A/A^*)_c$ from Step 1.
3. Using Fig. 47 through 55 and 83 through 86, iterate $\dot{m}/\rho_c u_c$ until p_b/p_∞ is satisfied. Note: $\dot{m} = (\rho v)_w$.
4. Use p_b/p_∞ to construct a pressure-distribution curve for the port side.

Nomenclature is given in Fig. 83. Several auxiliary charts for expediting computation are given in Fig. 84, 85, and 86.

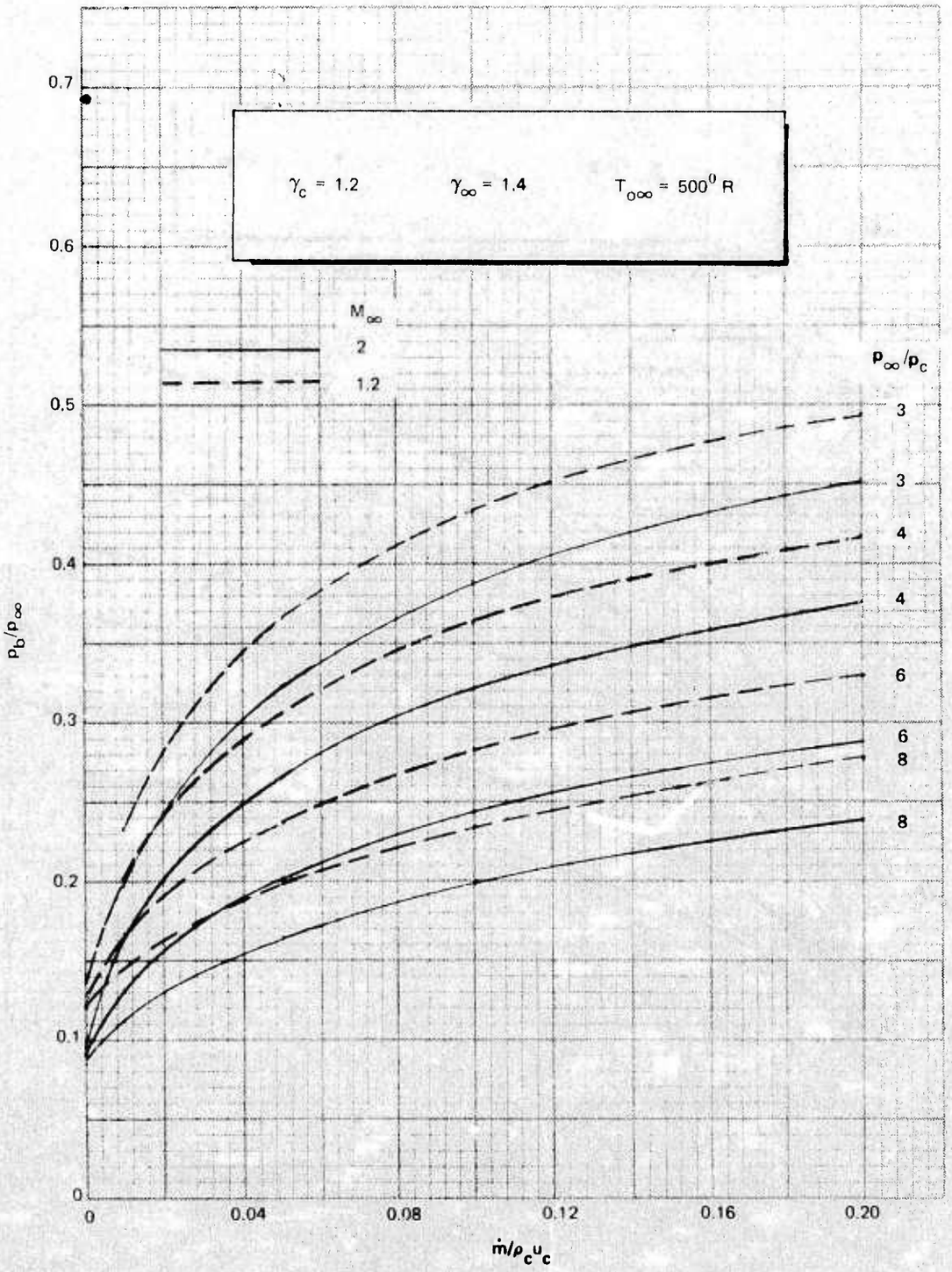

FIG. 47. p_b/p_∞ Versus $\dot{m}/\rho_c u_c$ for M_c = 3.5 With T_{oc} = 3,000° R.

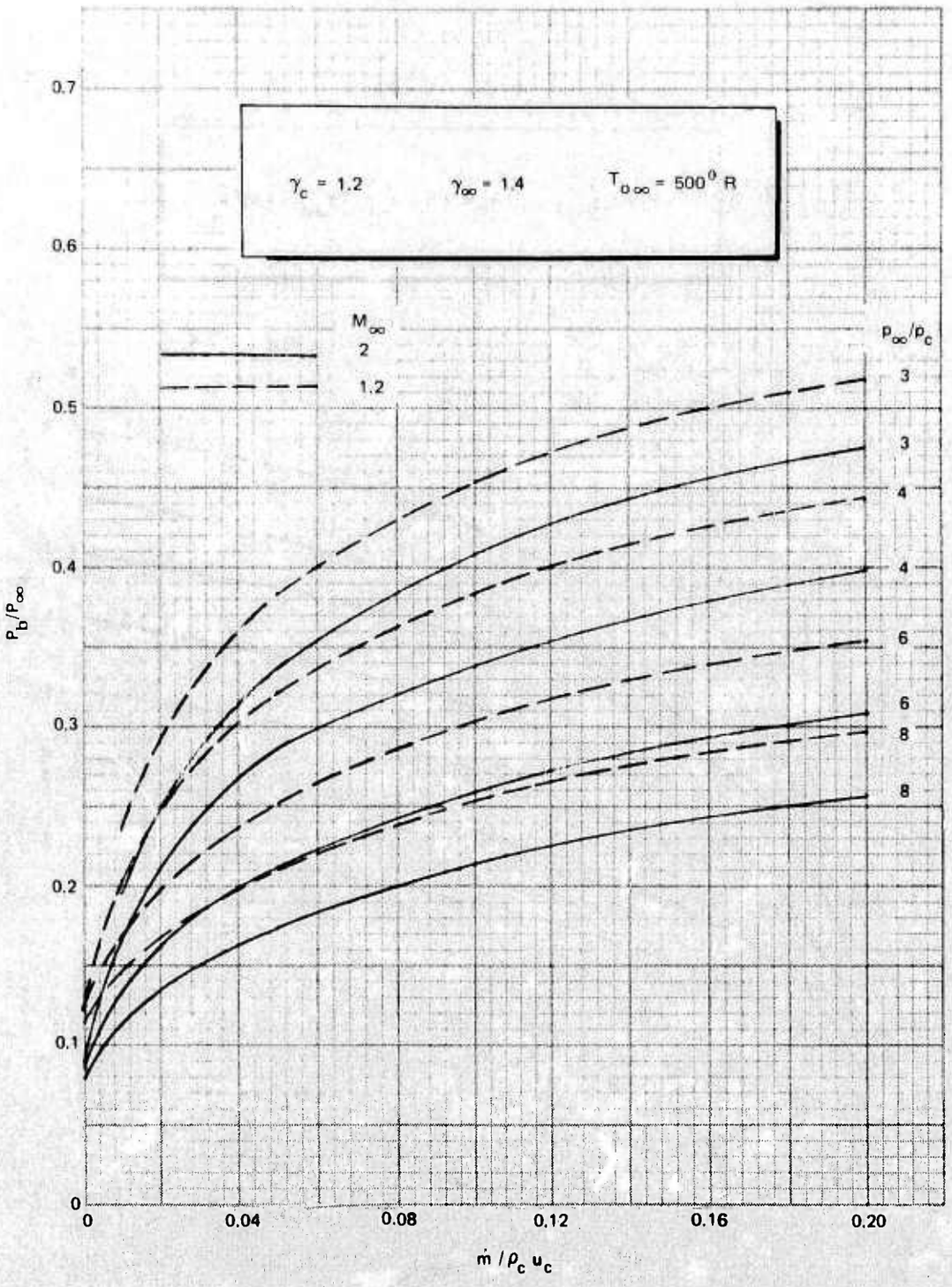

FIG. 48. p_b/p_∞ Versus $\dot{m}/\rho_c u_c$ for M_c = 4 With T_{oc} = 3,000° R.

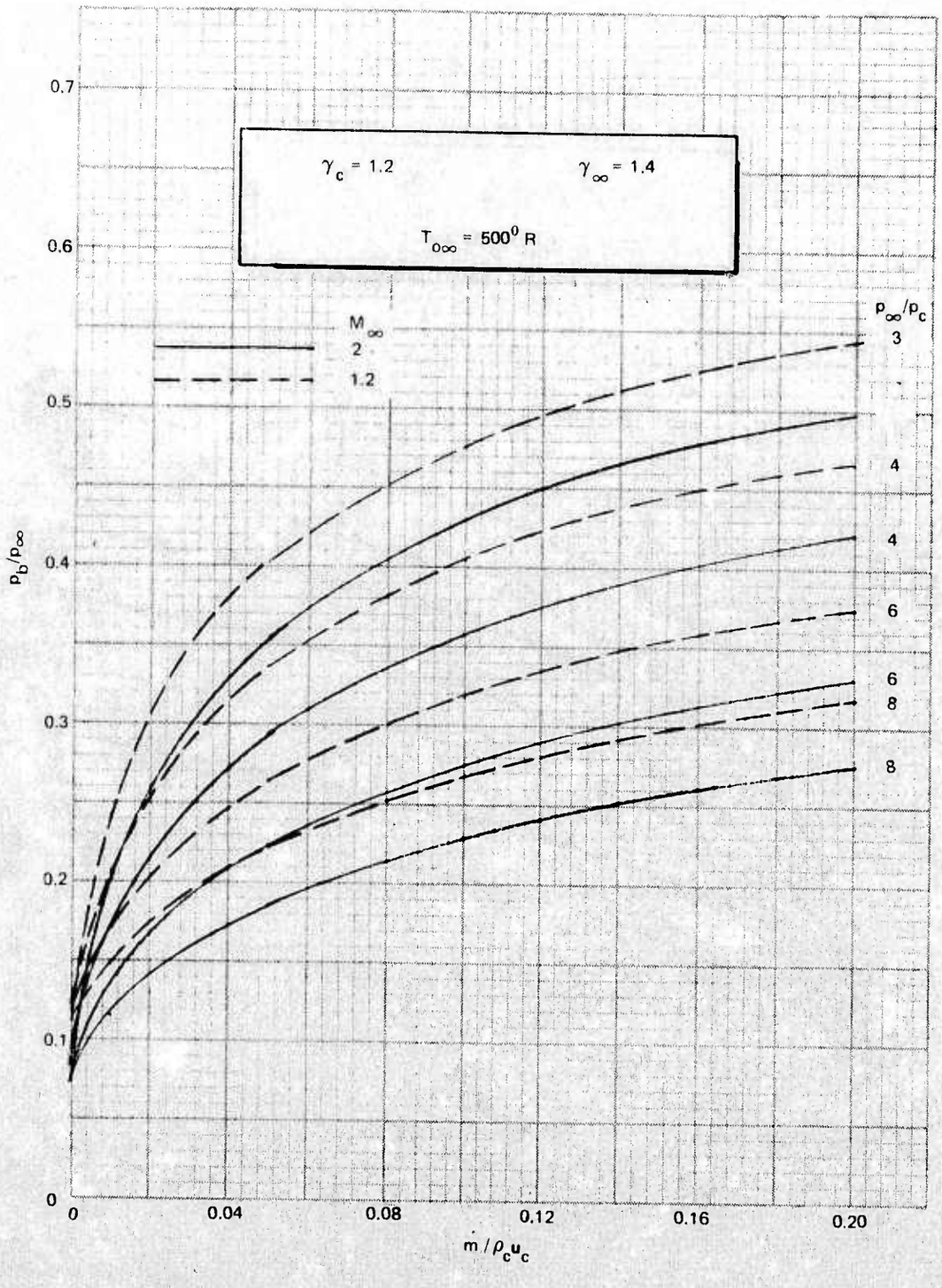

FIG. 49. p_b/p_∞ Versus $\dot{m}/\rho_c u_c$ for M_c = 4.5 With T_{oc} = 3,000° R.

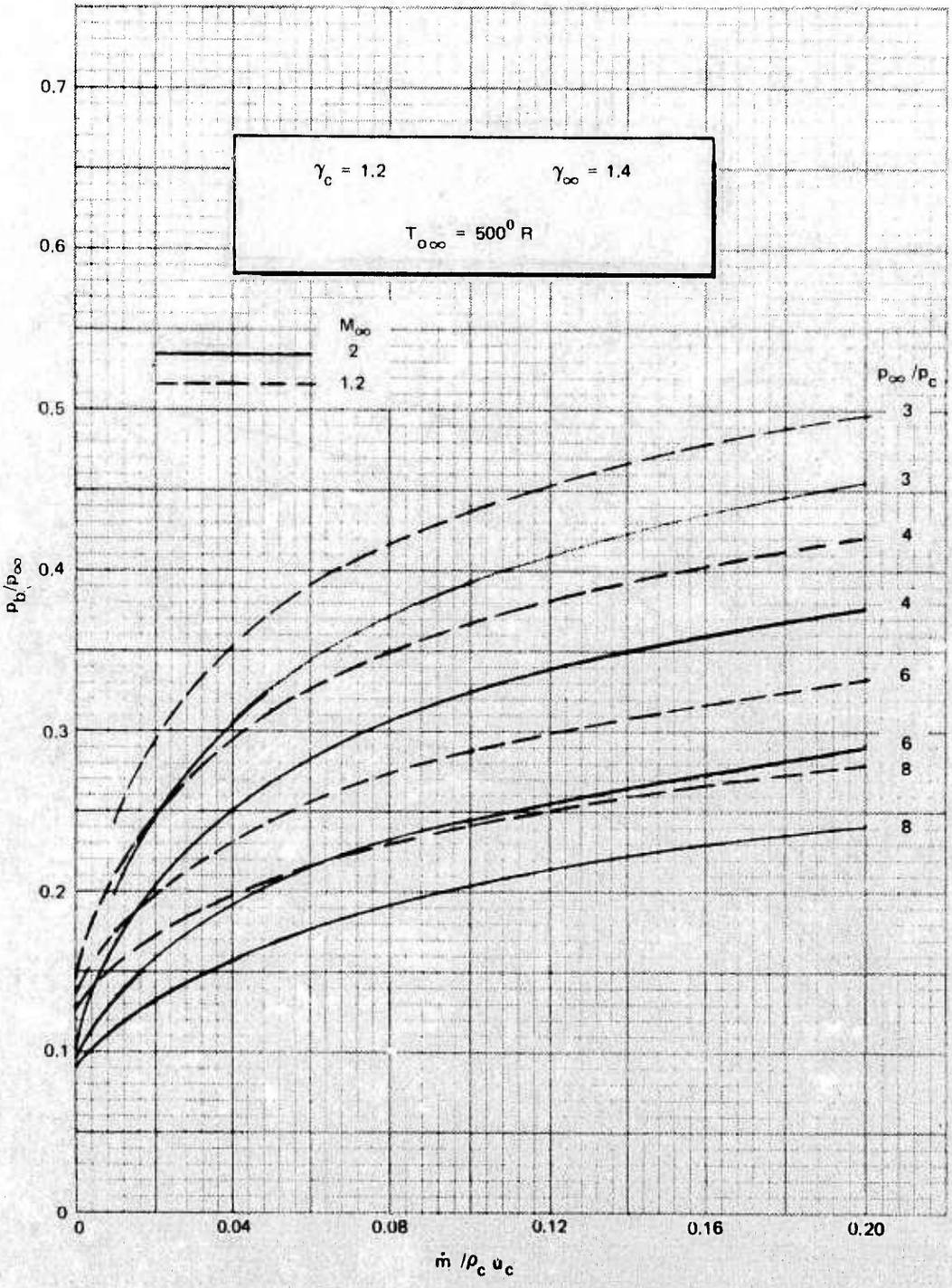

FIG. 50. p_b/p_∞ Versus $\dot{m} / \rho_c u_c$ for M_c = 3.5 With T_{oc} = 4,000° R.

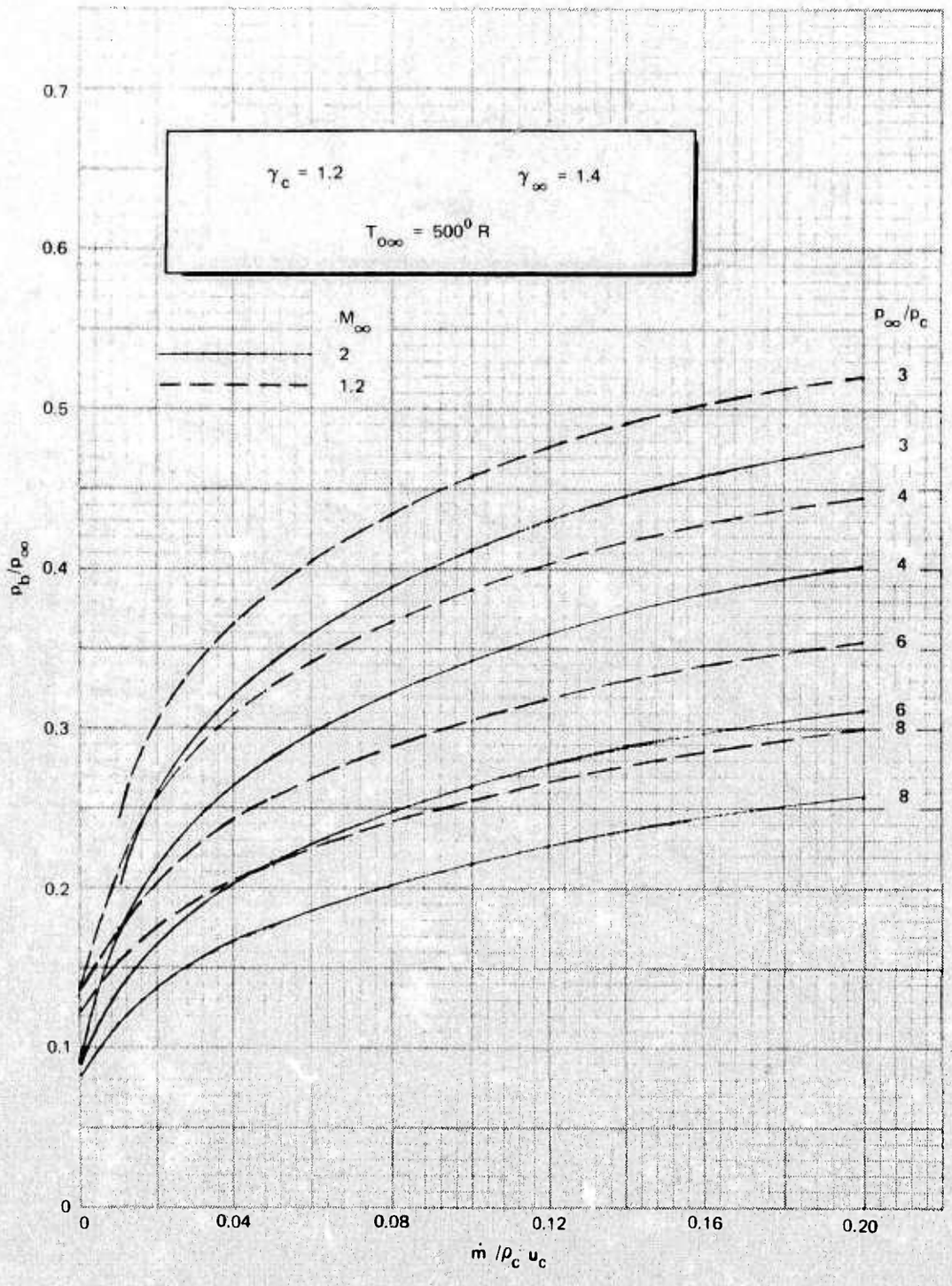

FIG. 51. p_b/p_∞ Versus $\dot{m}/\rho_c u_c$ for M_c = 4 With T_{oc} = 4,000° R.

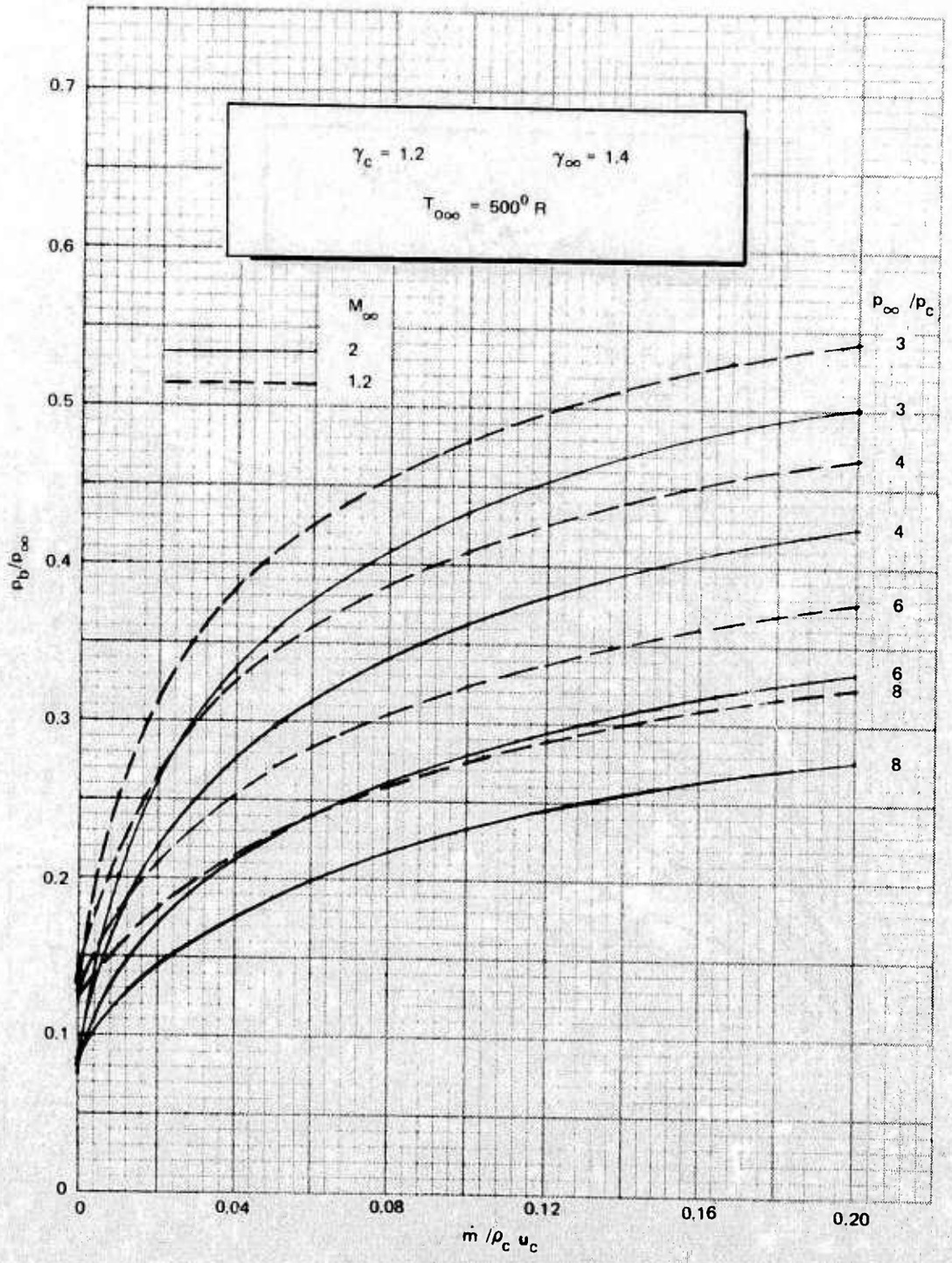

FIG. 52. p_b/p_∞ Versus $\dot{m} / \rho_c u_c$ for M_c = 4.5 With T_{oc} = 4,000° R.

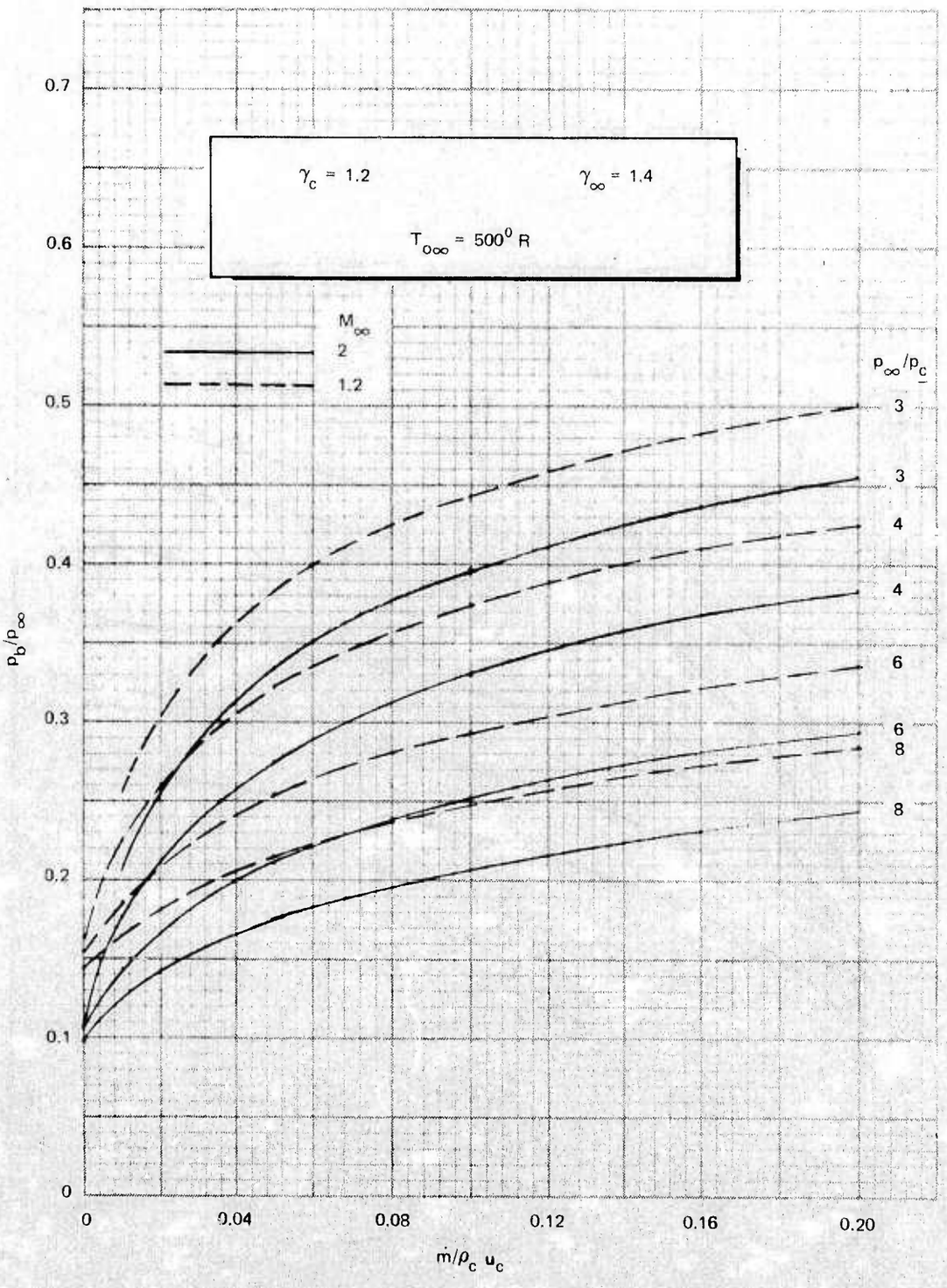

FIG. 53. p_b/p_∞ Versus $\dot{m}/\rho_c u_c$ for M_c = 3.5 With T_{oc} = 5,500° R.

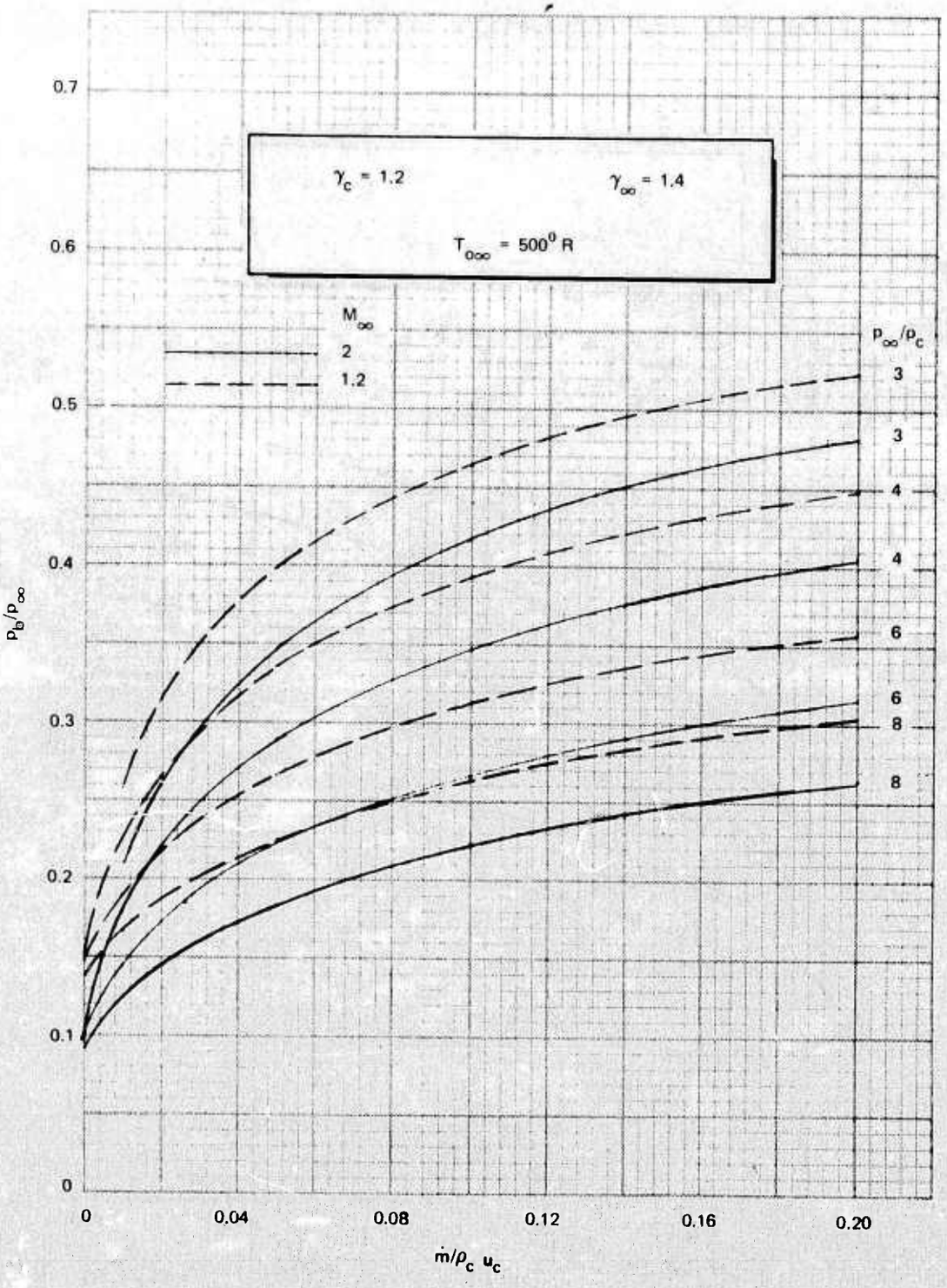

FIG. 54. p_b/p_∞ Versus $\dot{m}/\rho_c u_c$ for M_c = 4 With T_{oc} = 5,500° R.

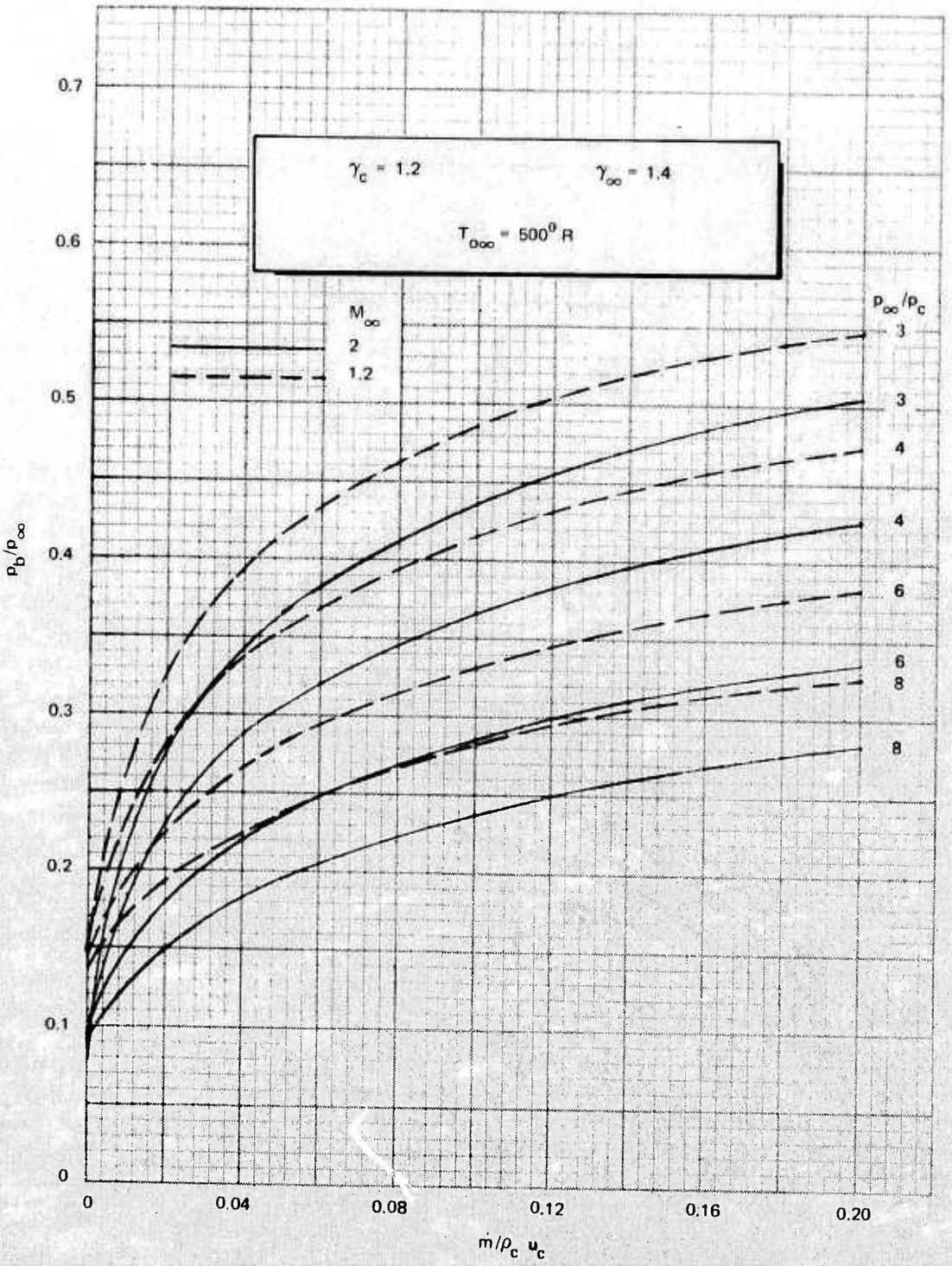

FIG. 55. p_b/p_∞ Versus $\dot{m}/\rho_c\ u_c$ for M_c = 4.5 With T_{oc} = 5,500° R.

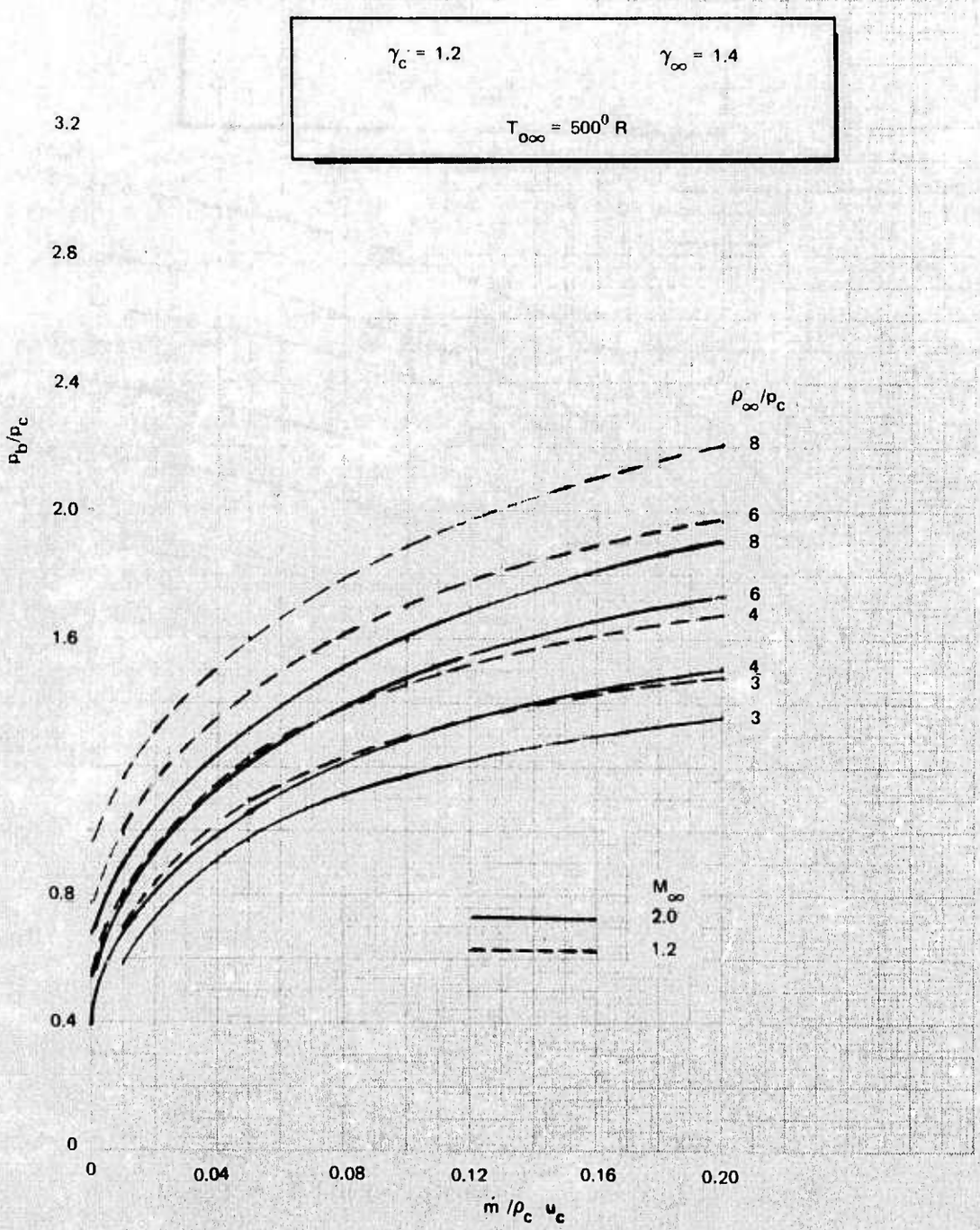

FIG. 56. p_b/p_c Versus $\dot{m}/\rho_c\ u_c$ for M_c = 3.5 With T_{oc} = 3,000° R.

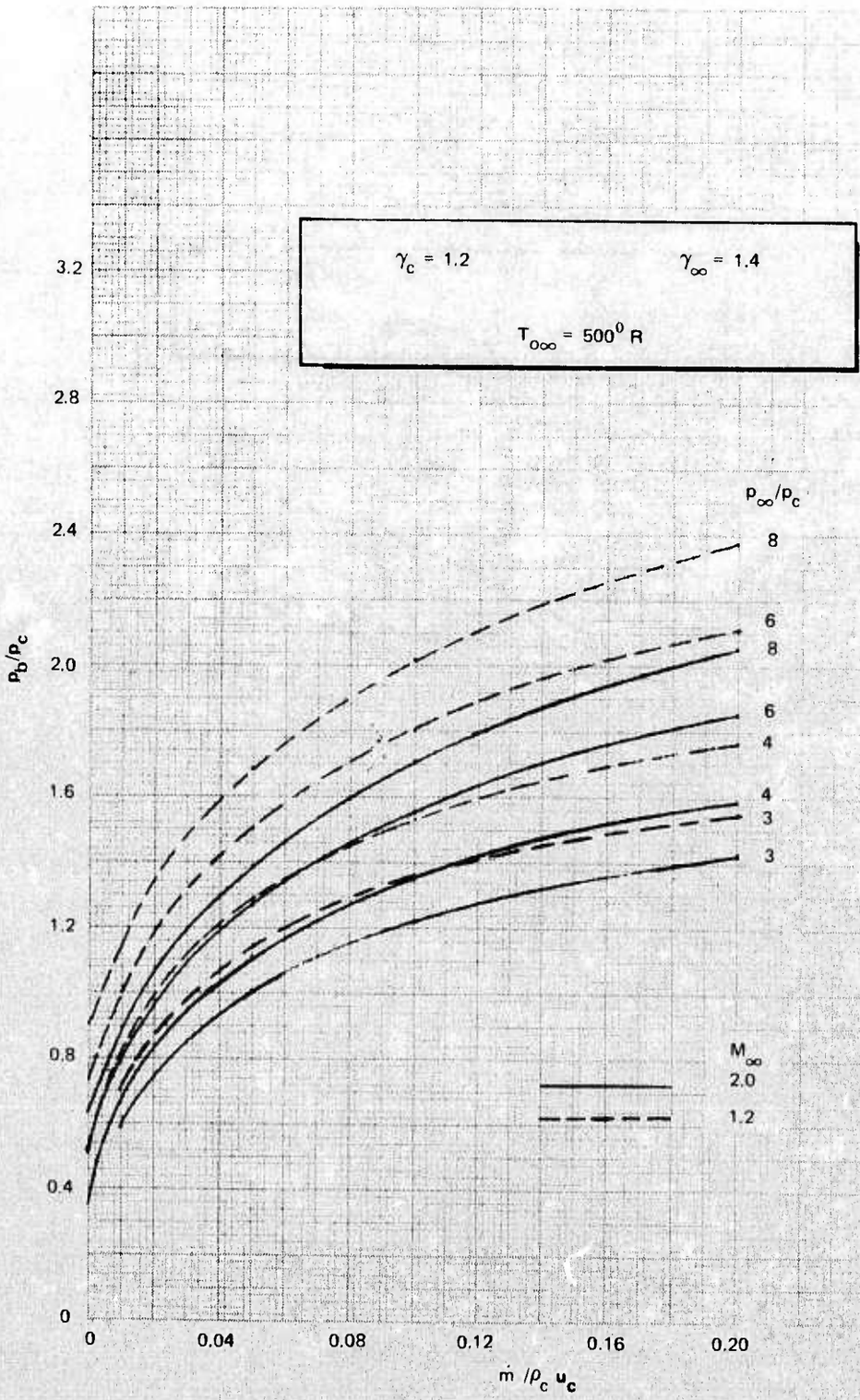

FIG. 57. p_b/p_c Versus $\dot{m}/\rho_c u_c$ for $M_c = 4$ With $T_{oc} = 3{,}000^0$ R.

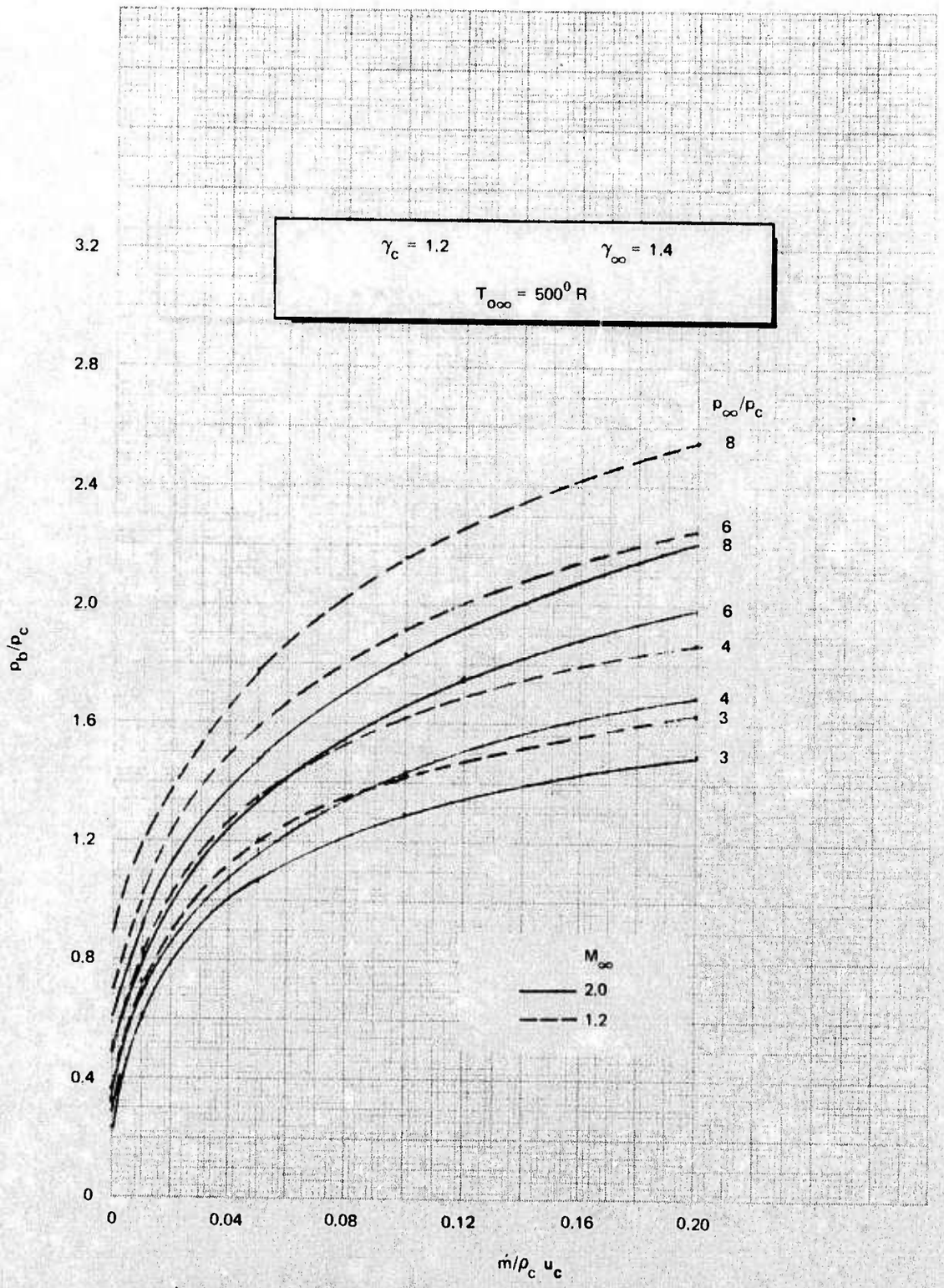

FIG. 58. p_b/p_c Versus $\dot{m}/\rho_c u_c$ for M_c = 4.5 With T_{oc} = 3,000° R.

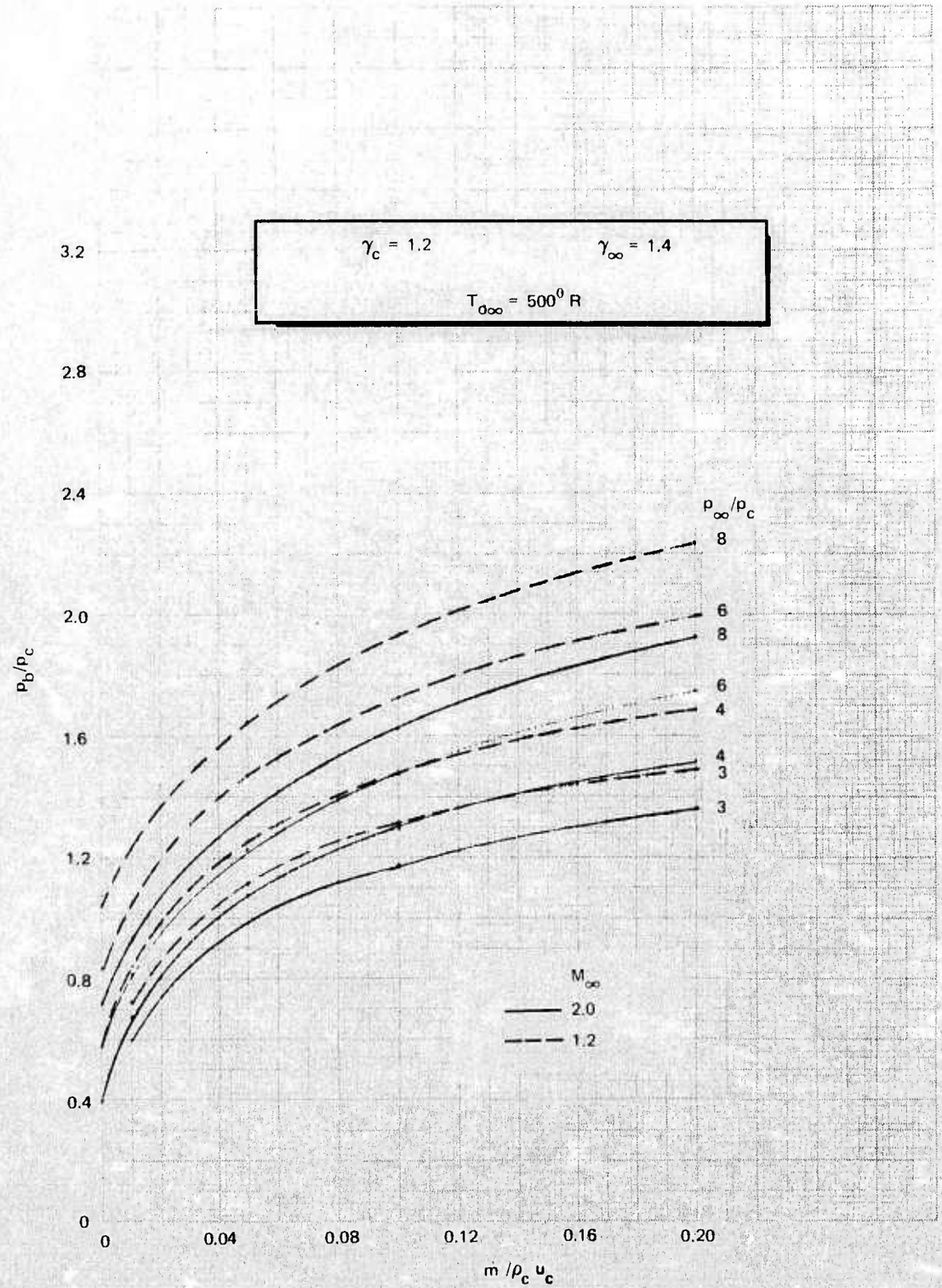

FIG. 59. p_b/p_c Versus $\dot{m}/\rho_c u_c$ for M_c = 3.5 With T_{oc} = 4,000° R.

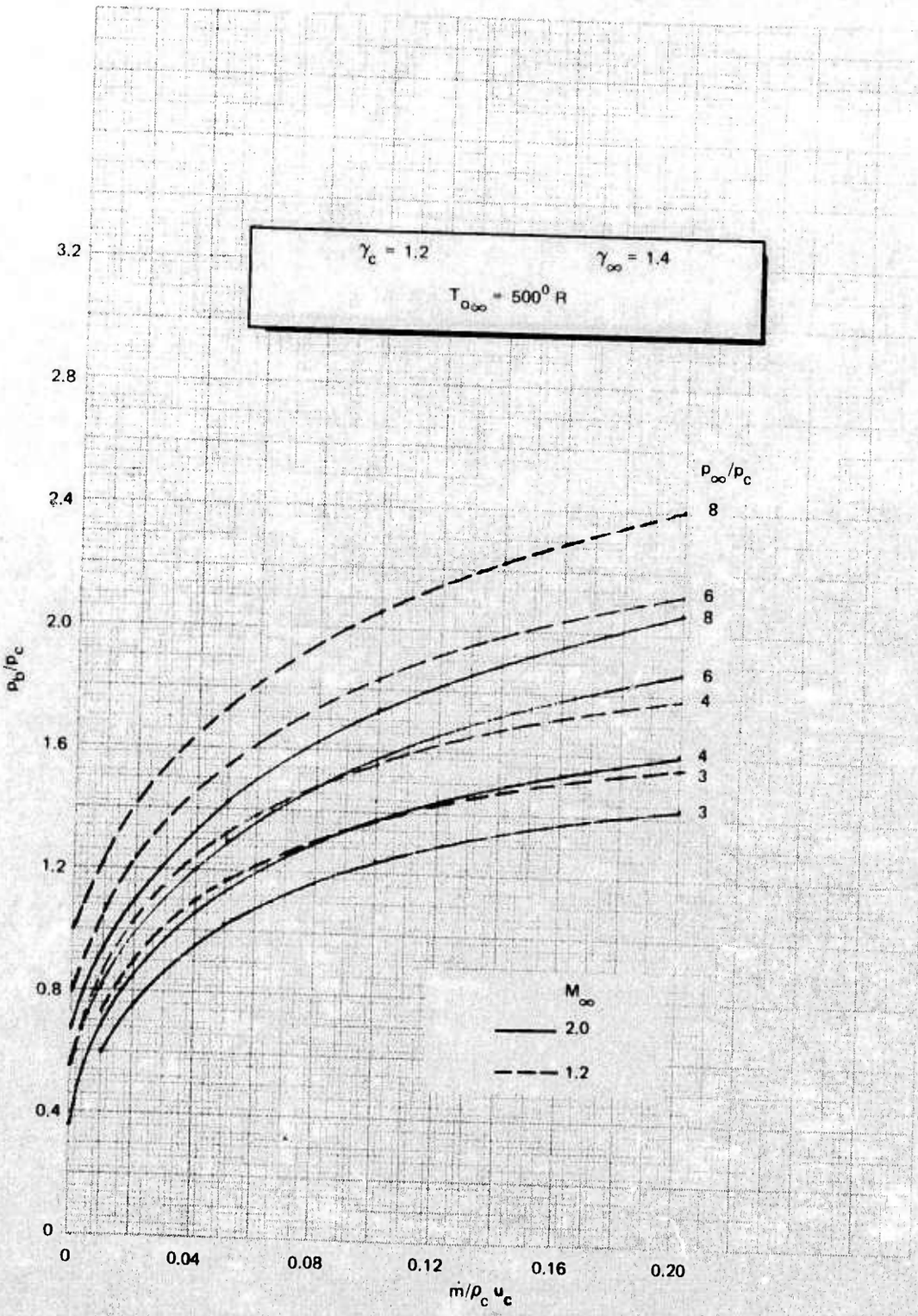

FIG. 60. p_b/p_c Versus $\dot{m}/\rho_c u_c$ for $M_c = 4$ With $T_{oc} = 4{,}000^\circ$ R.

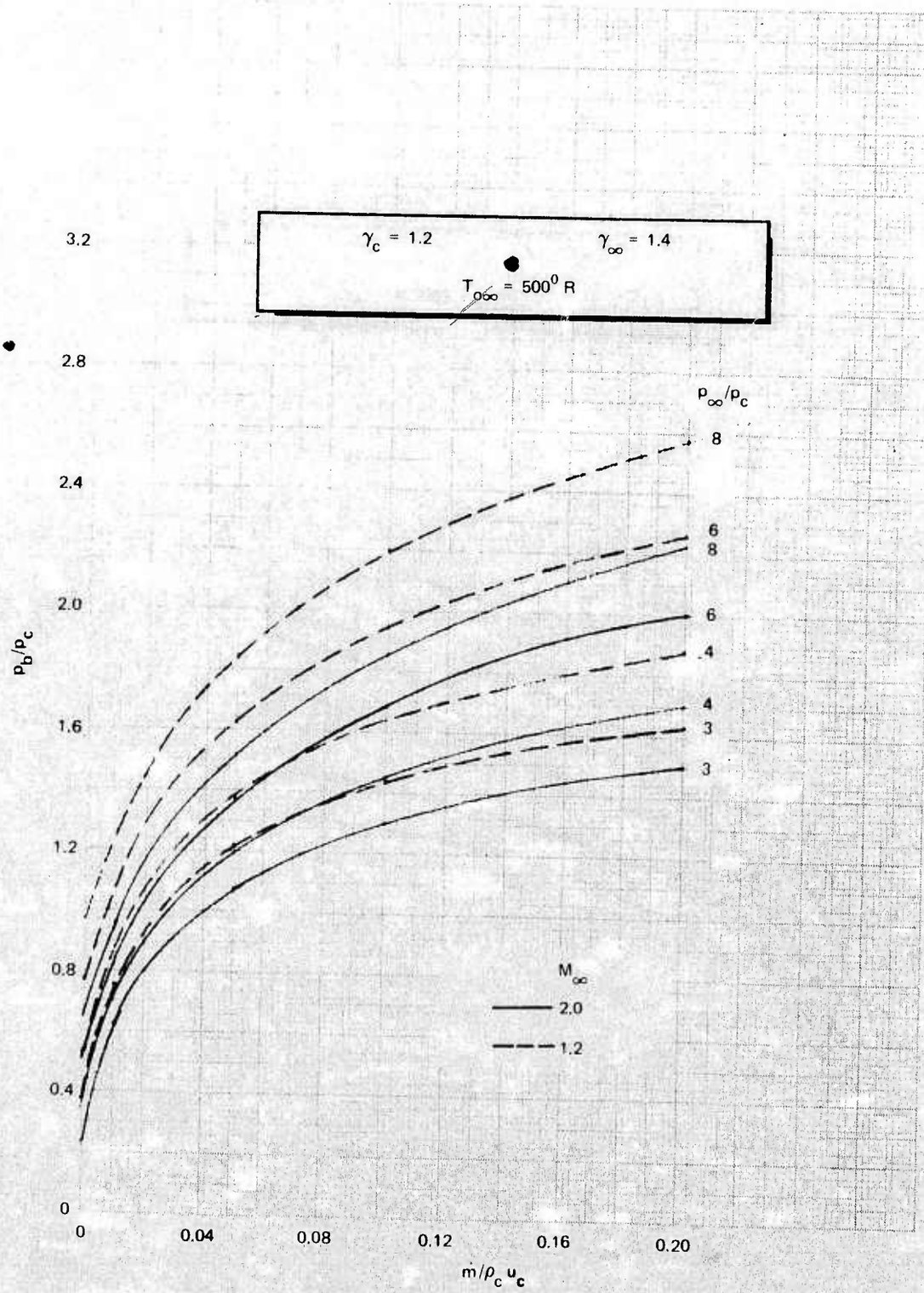

FIG. 61. p_b/p_c Versus $\dot{m}/\rho_c u_c$ for M_c = 4.5 With T_{oc} = 4,000° R.

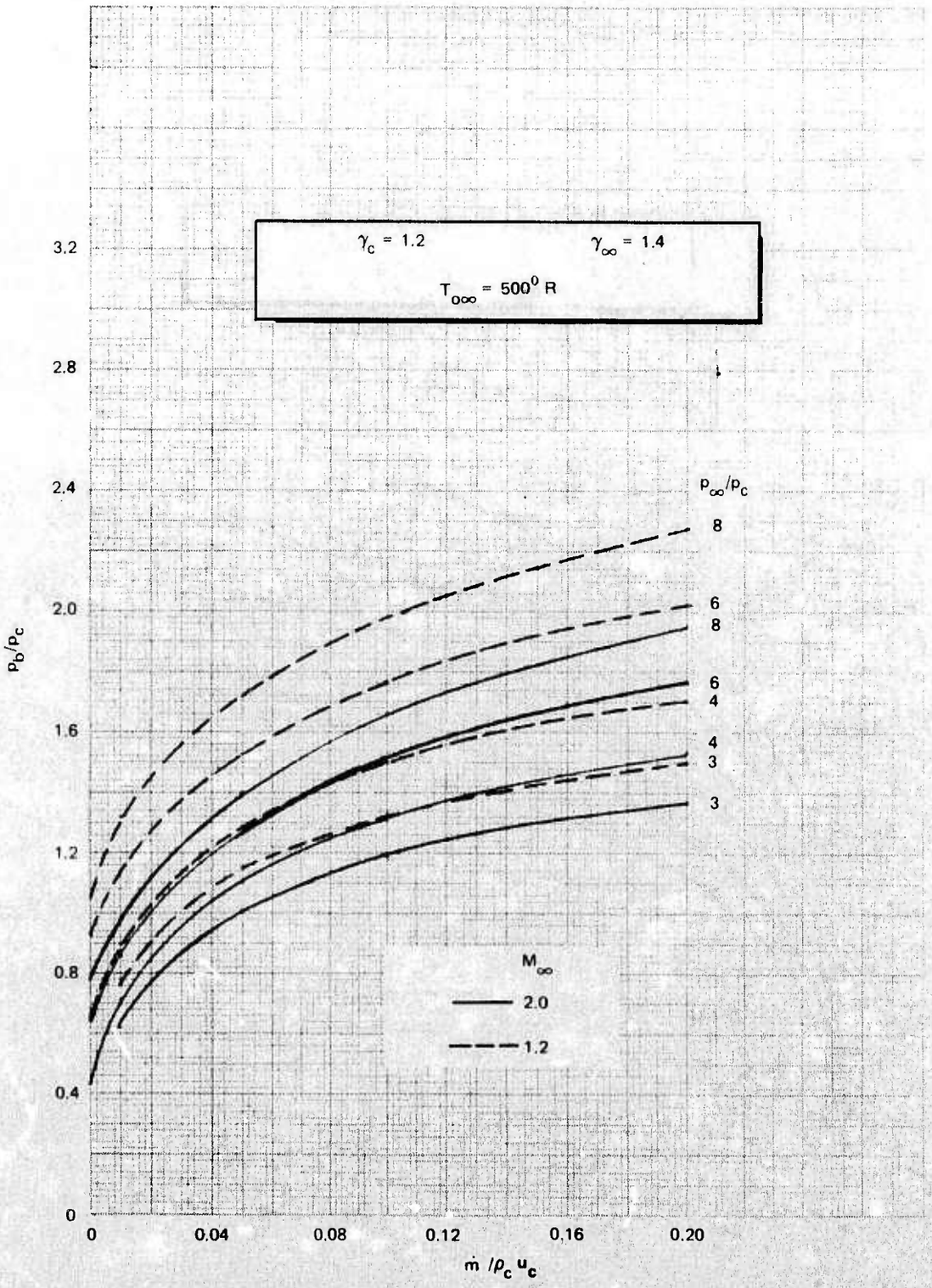

FIG. 62. p_b/p_c Versus $\dot{m}/\rho_c u_c$ for M_c = 3.5 With T_{oc} = 5,500° R.

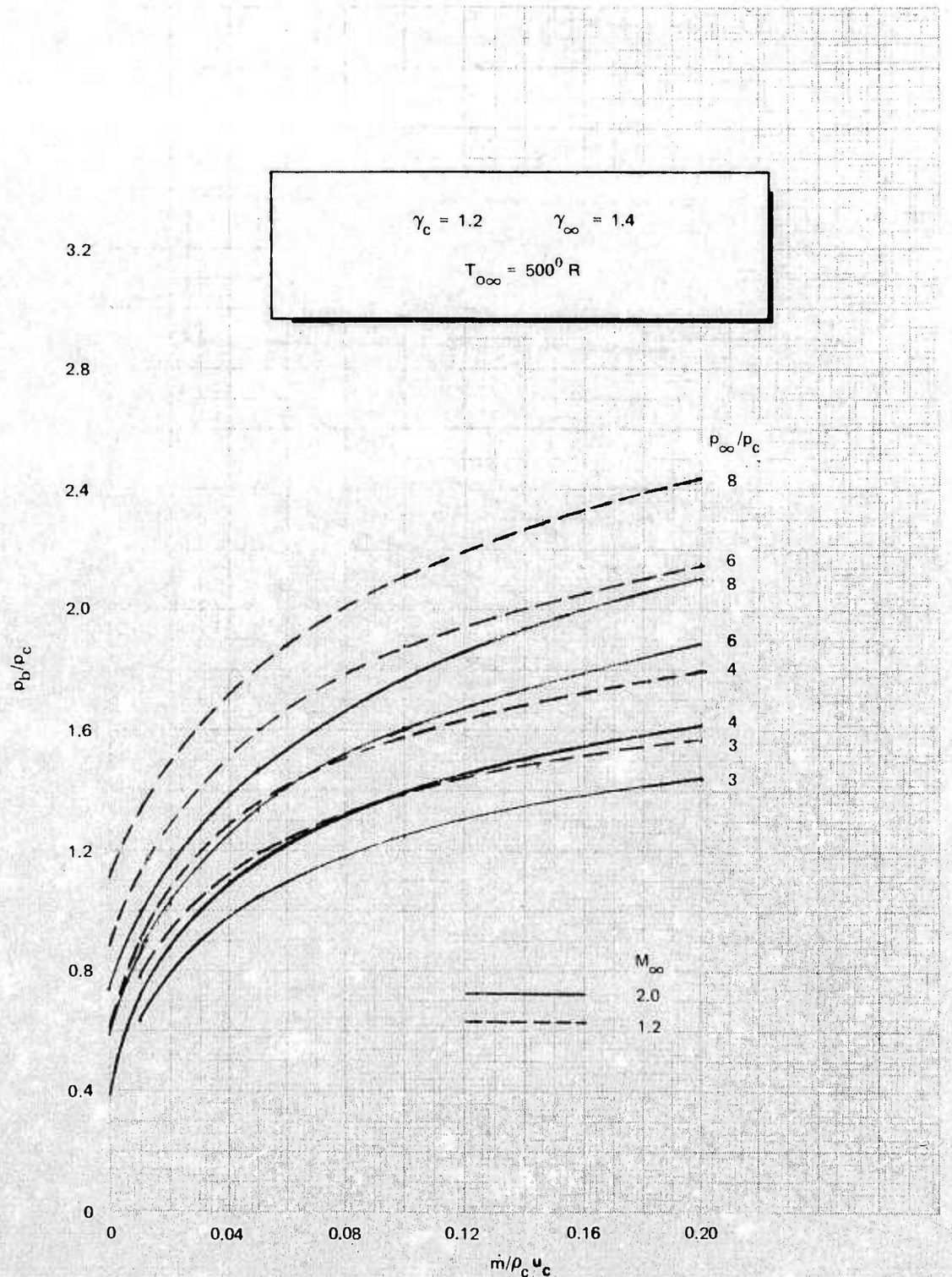

FIG. 63. p_b/p_c Versus $\dot{m}/\rho_c u_c$ for M_c = 4 With T_{oc} = 5,500° R.

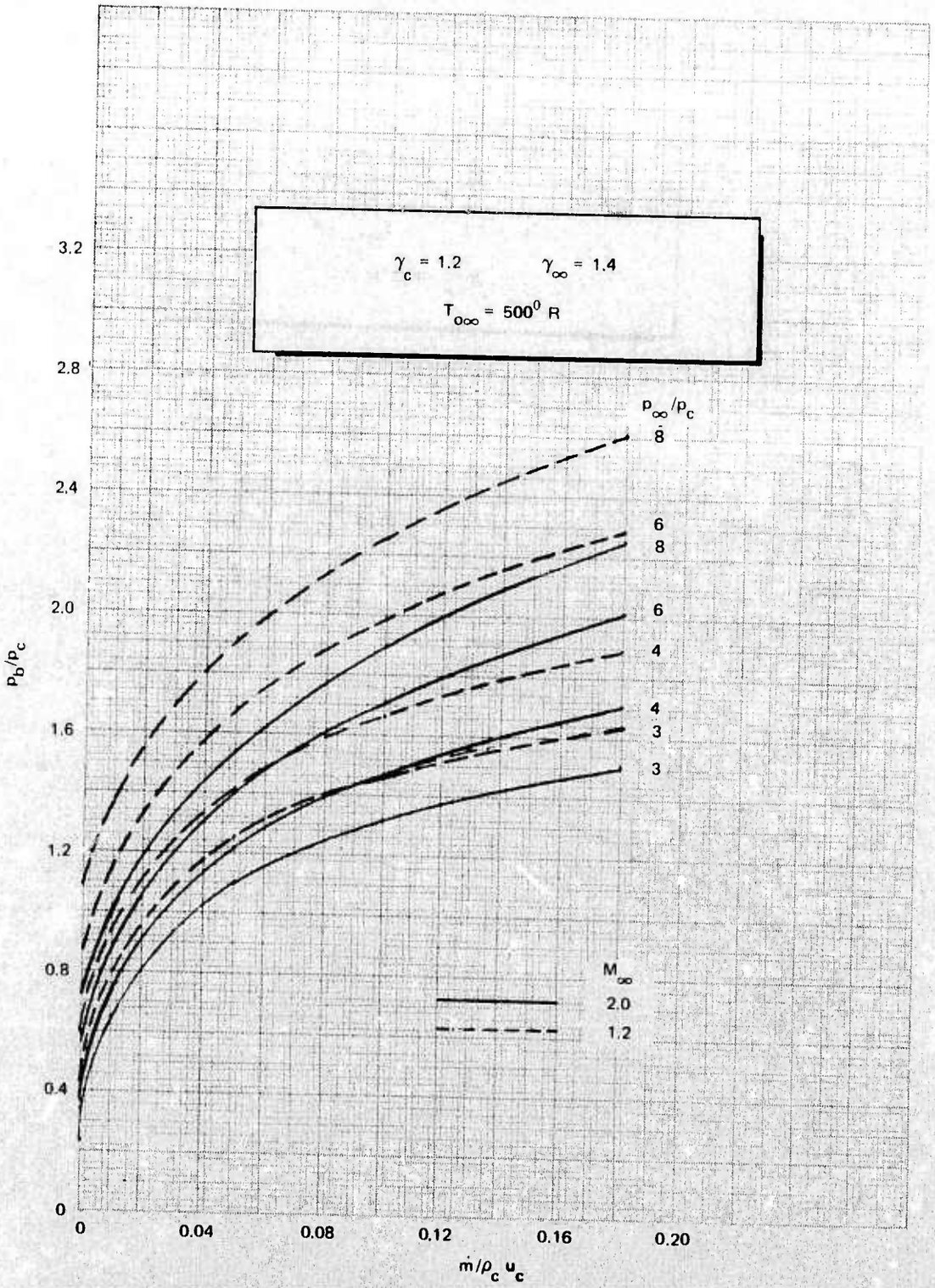

FIG. 64. p_b/p_c Versus $\dot{m}/\rho_c u_c$ for M_c = 4.5 With T_{oc} = 5,500° R.

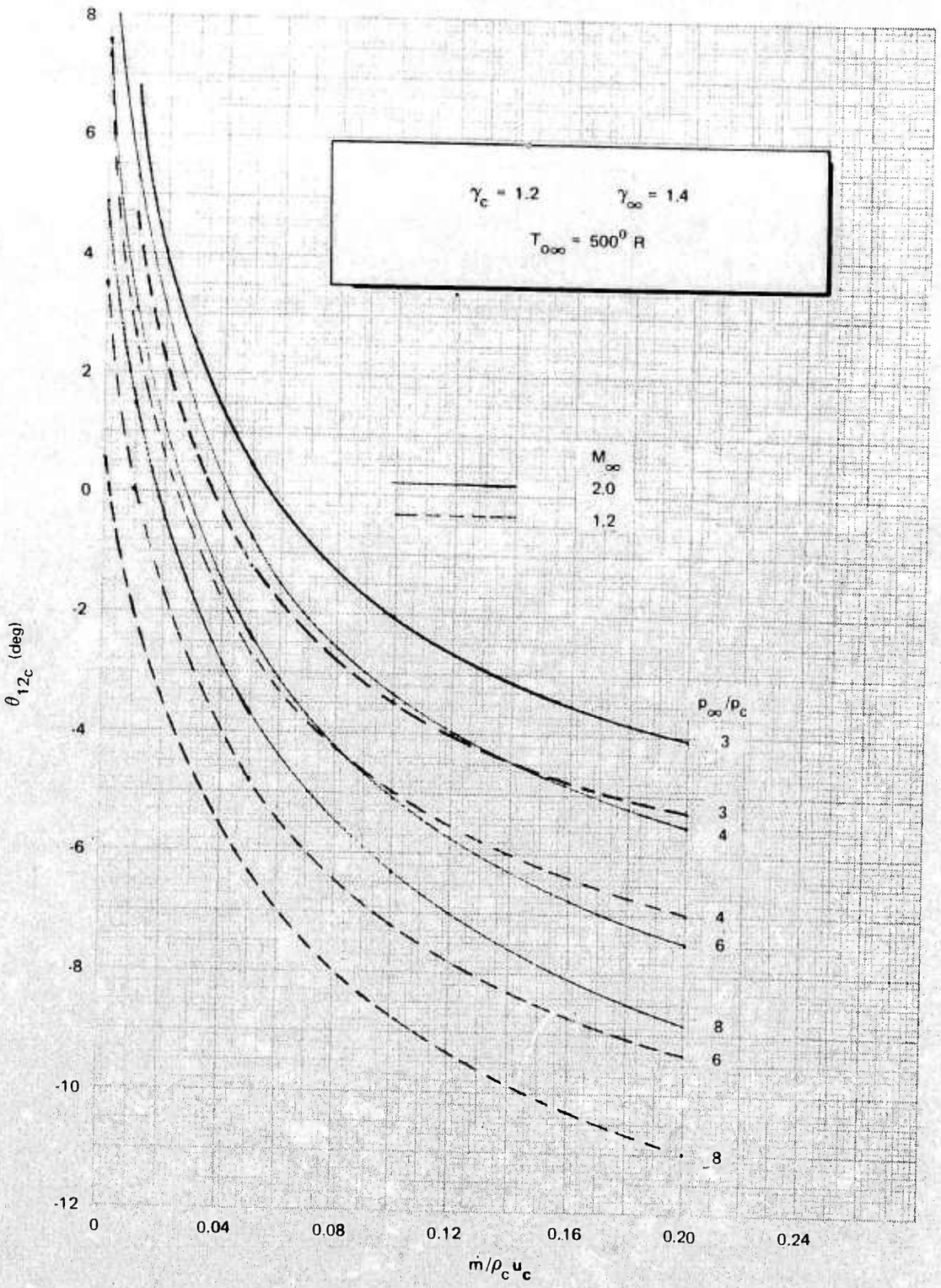

FIG. 65. θ_{12_c} Versus $\dot{m}/\rho_c u_c$ for M_c = 3.5 With T_{oc} = 3,000° R.

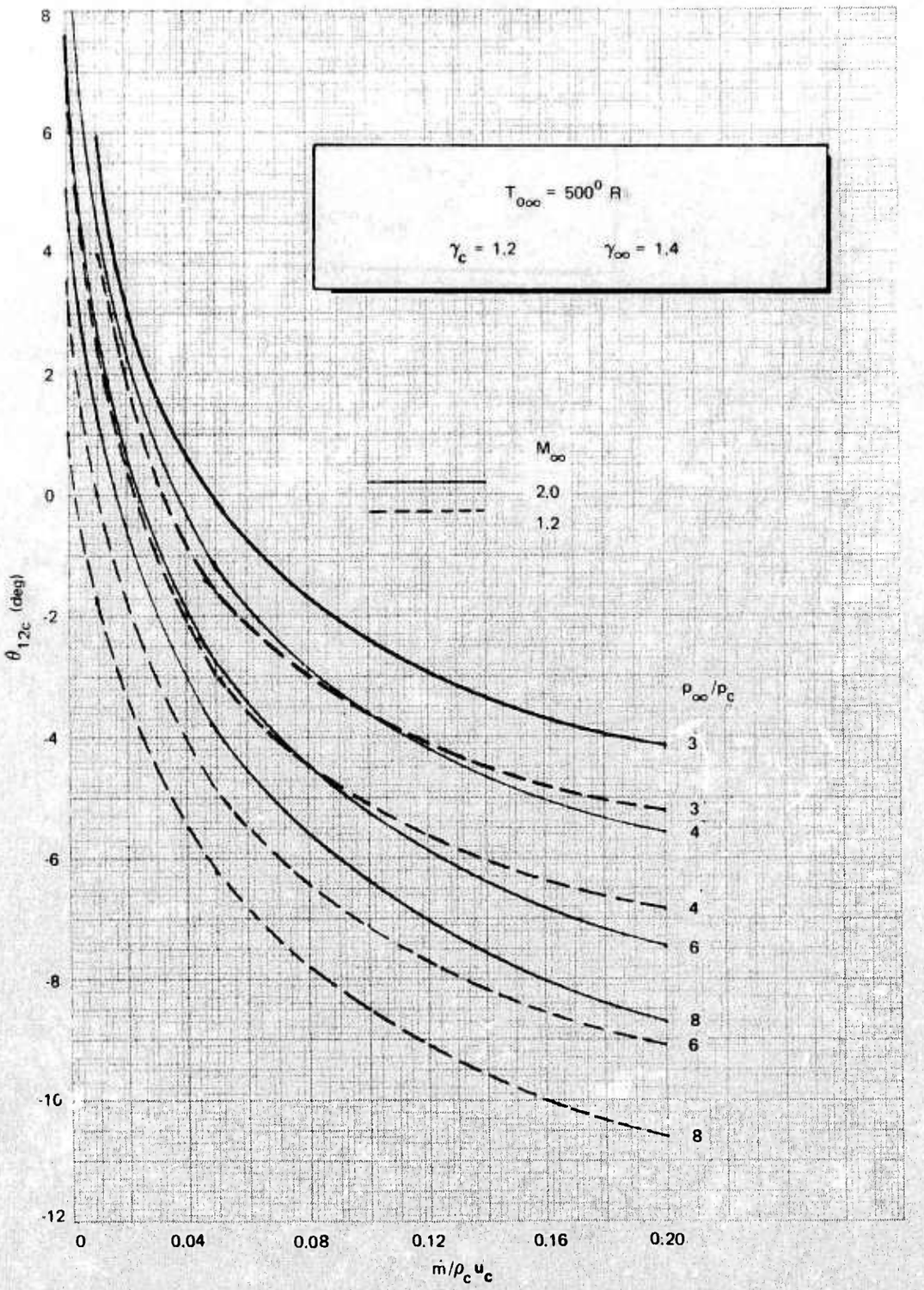

FIG. 66. θ_{12c} Versus $\dot{m}/\rho_c u_c$ for M_c = 4 WIth T_{oc} = 3,000° R.

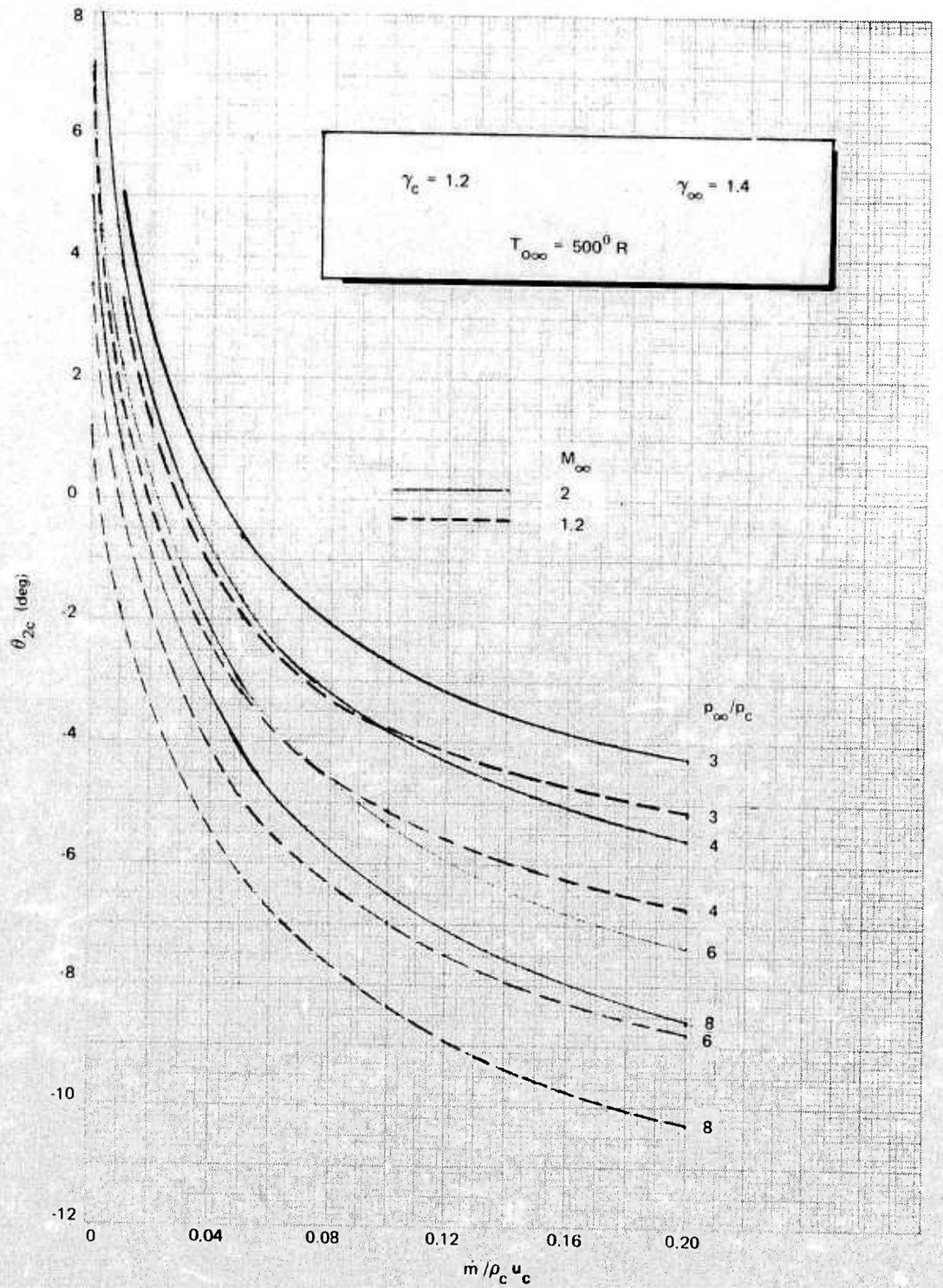

FIG. 67. θ_{12c} Versus $\dot{m}/\rho_c u_c$ for M_c = 4.5 With T_{oc} = 3,000° R.

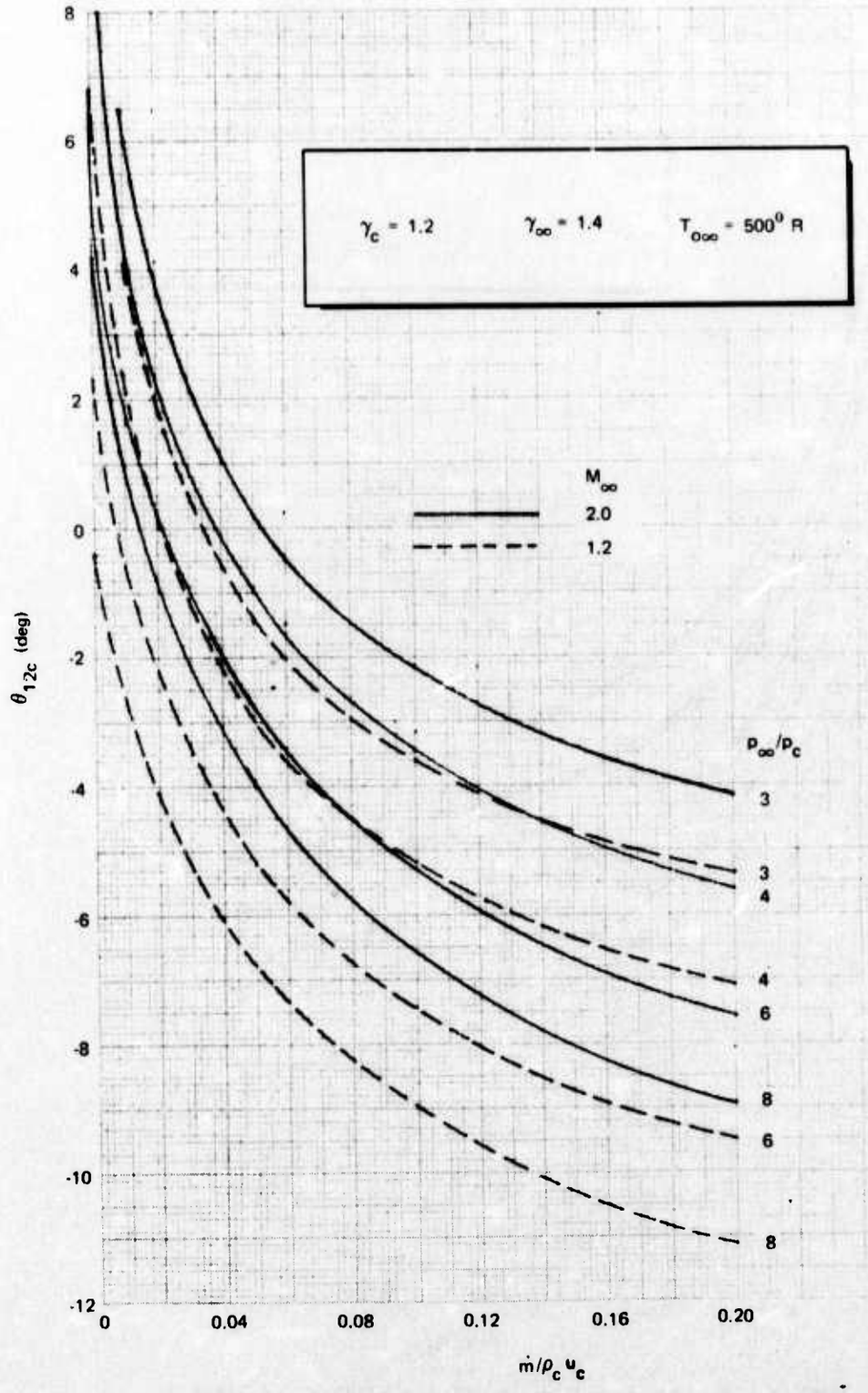

FIG. 68. θ_{12c} Versus $\dot{m}/\rho_c u_c$ for M_c = 3.5 With T_{oc} = 4,000° R.

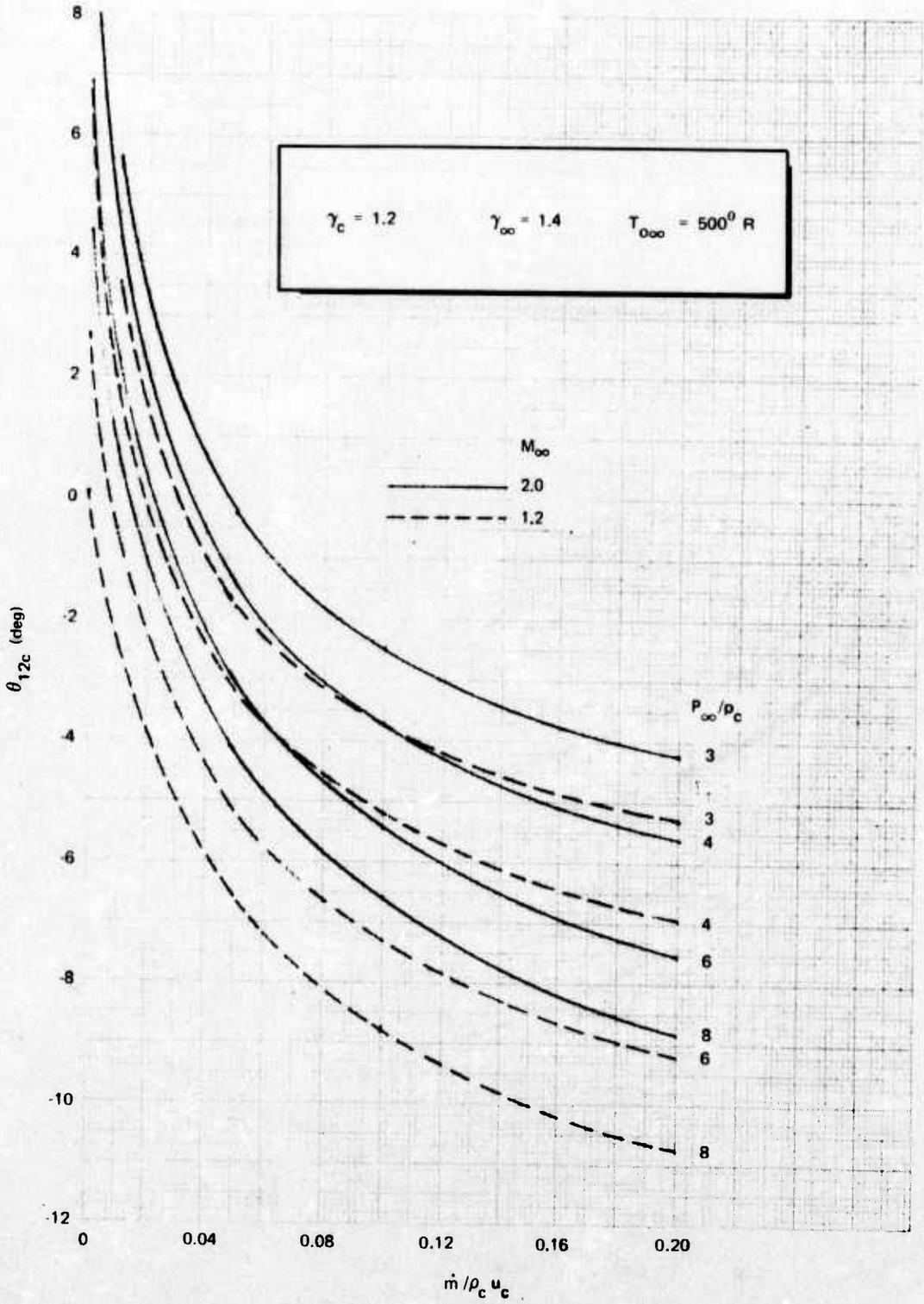

FIG. 69. θ_{12c} Versus $\dot{m}/\rho_c u_c$ for $M_c = 4$ With $T_{oc} = 4{,}000^0$ R.

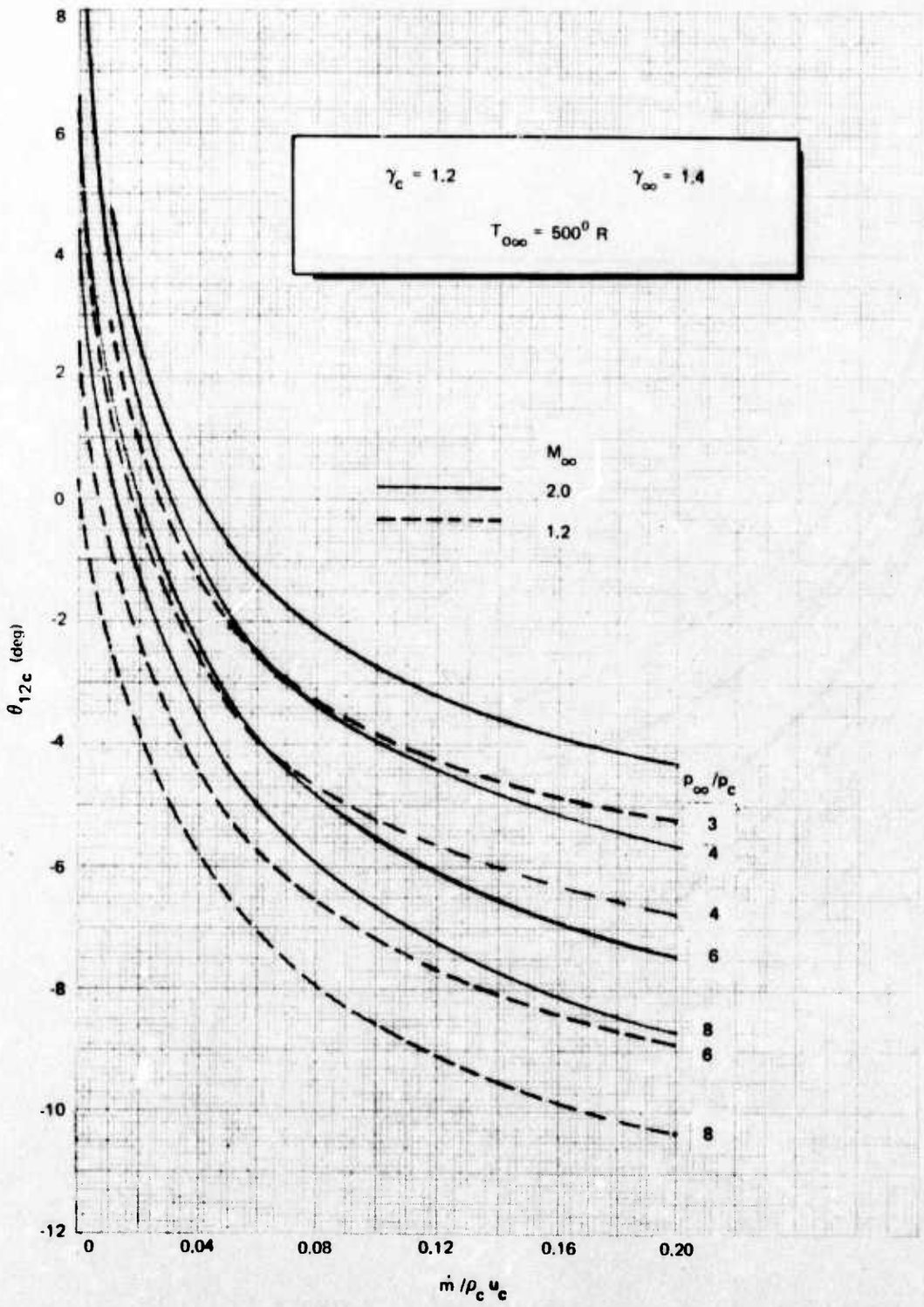

FIG. 70. θ_{12c} Versus $\dot{m}/\rho_c u_c$ for M_c = 4.5 With T_{oc} = 4,000° R.

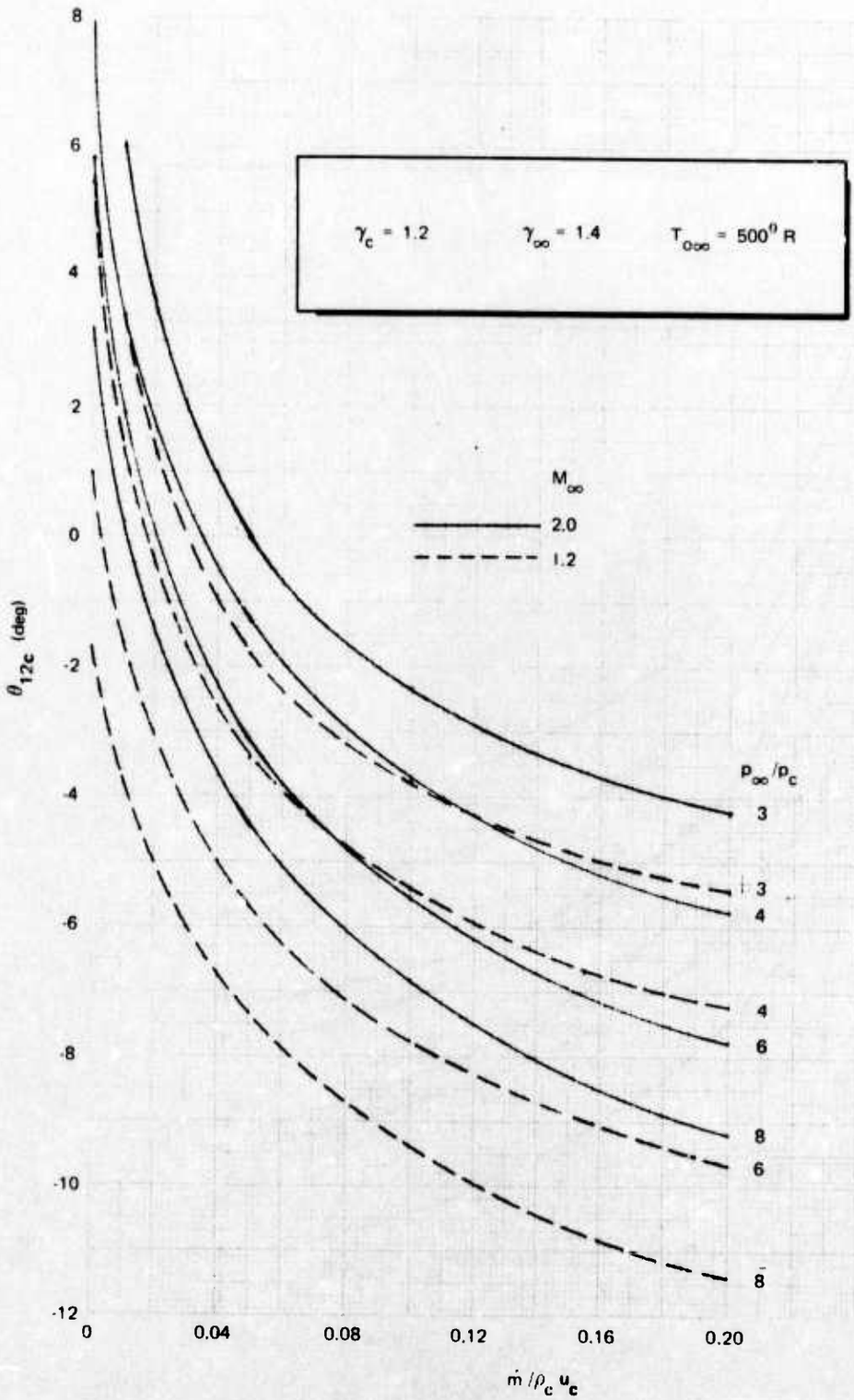

FIG. 71. θ_{12c} Versus $\dot{m}/\rho_c u_c$ for M_c = 3.5 With T_{0c} = 5,500° R.

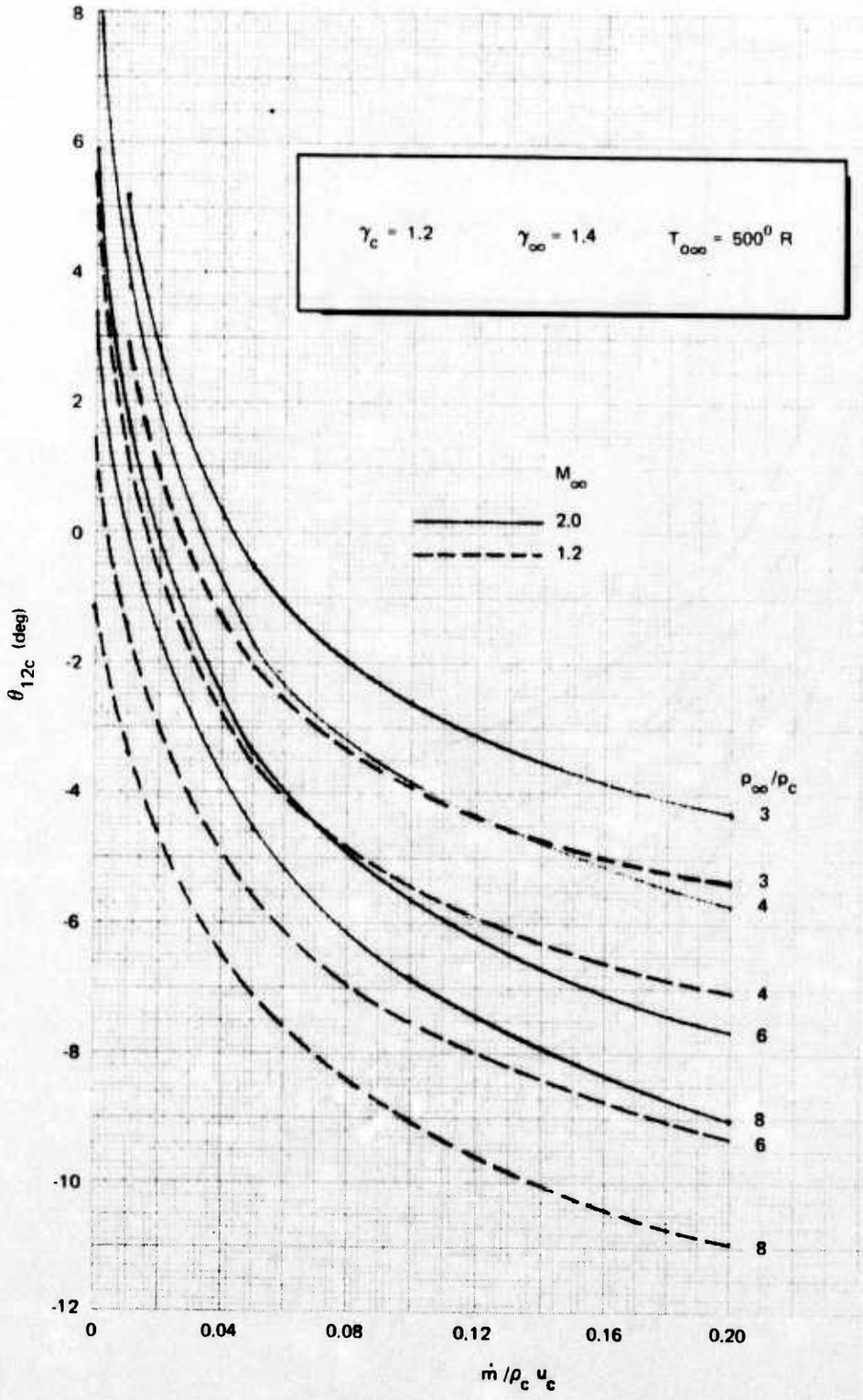

FIG. 72. θ_{12c} Versus $\dot{m}/\rho_c u_c$ for M_c = 4 With T_{oc} = 5,500° R.

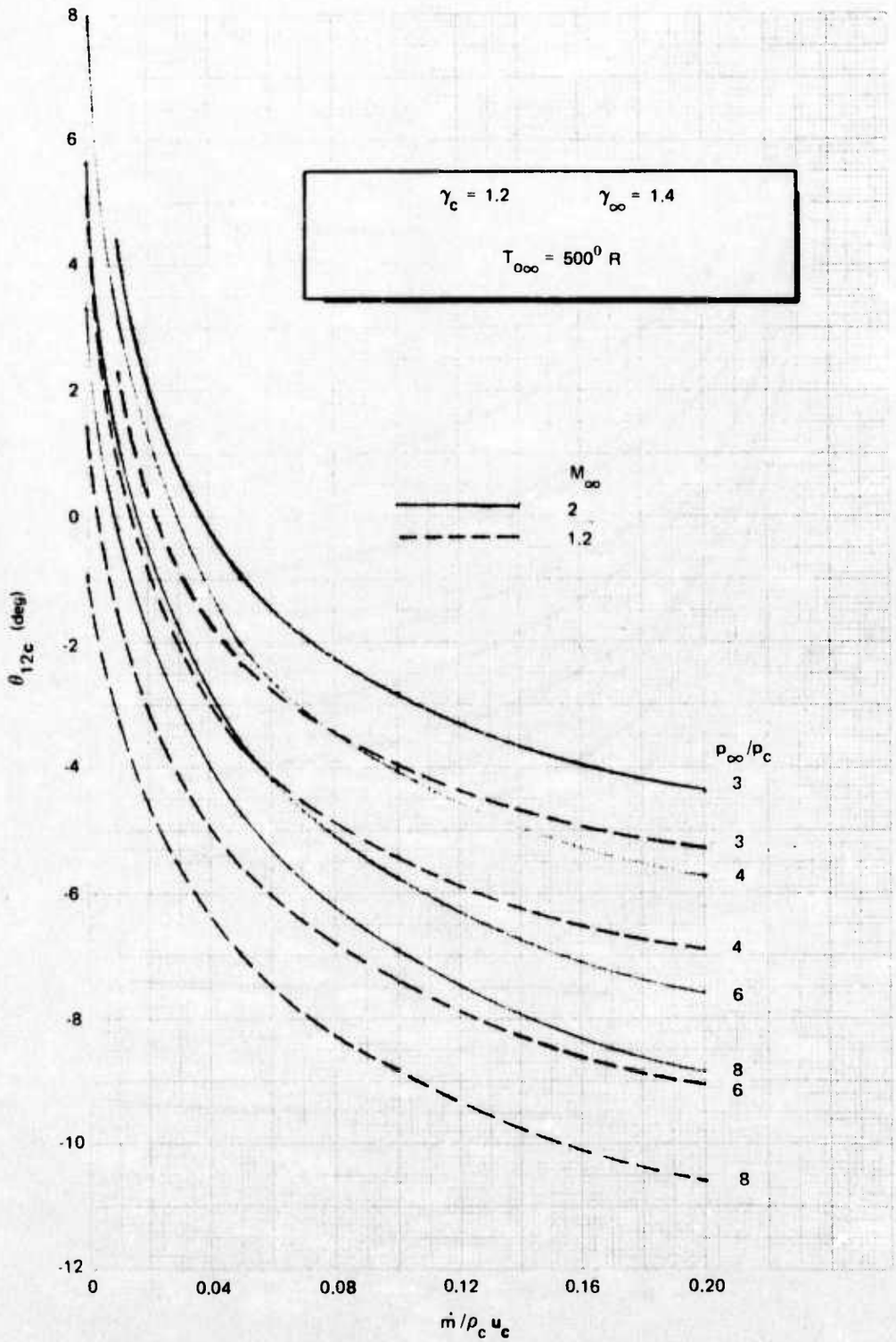

FIG. 73. θ_{12c} Versus $\dot{m}/\rho_c u_c$ for M_c = 4.5 With T_{oc} = 5,500° R.

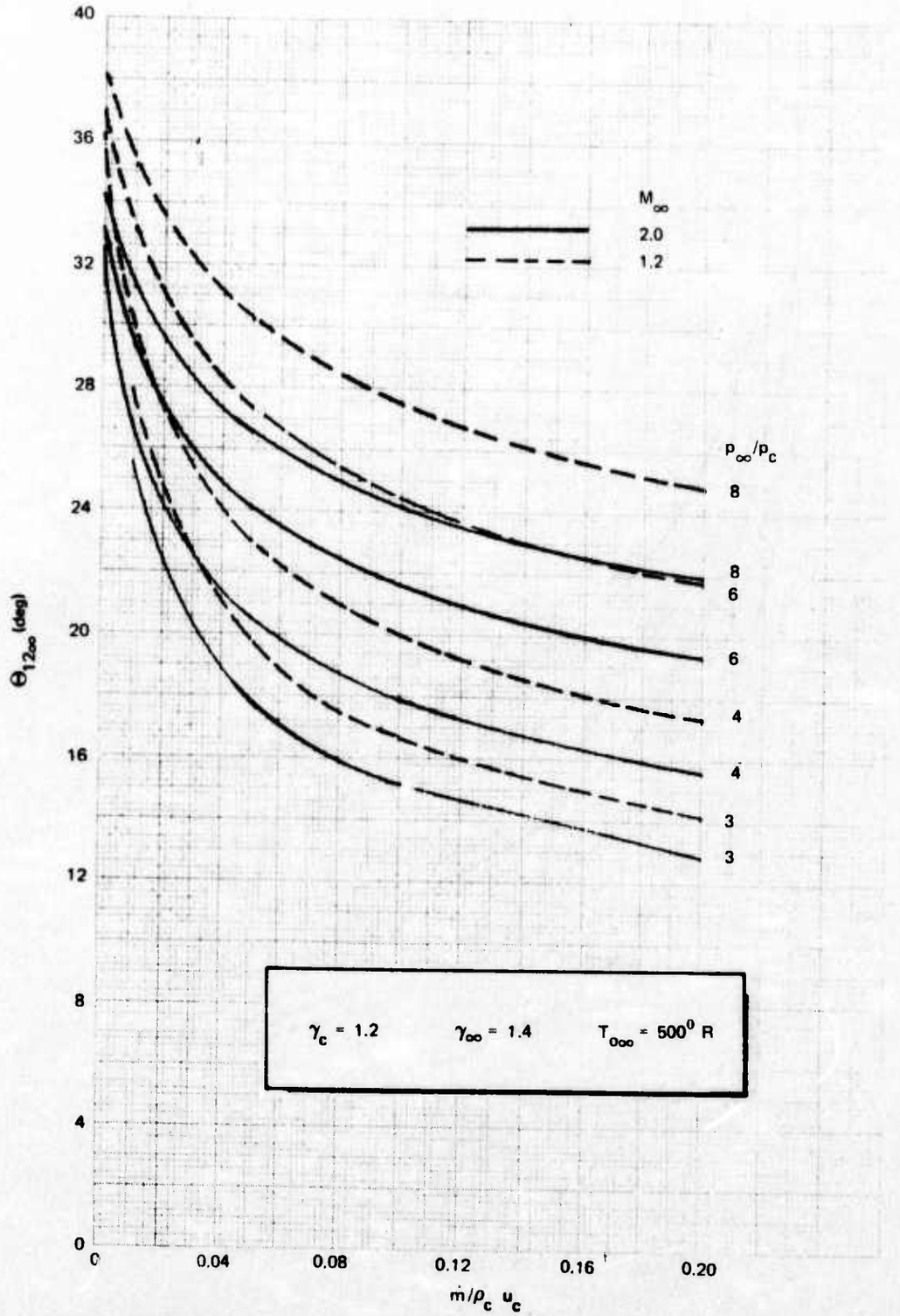

FIG. 74. $\Theta_{12\infty}$ Versus $\dot{m}/\rho_c u_c$ for M_c = 3.5 With T_{0c} = 3,000°R.

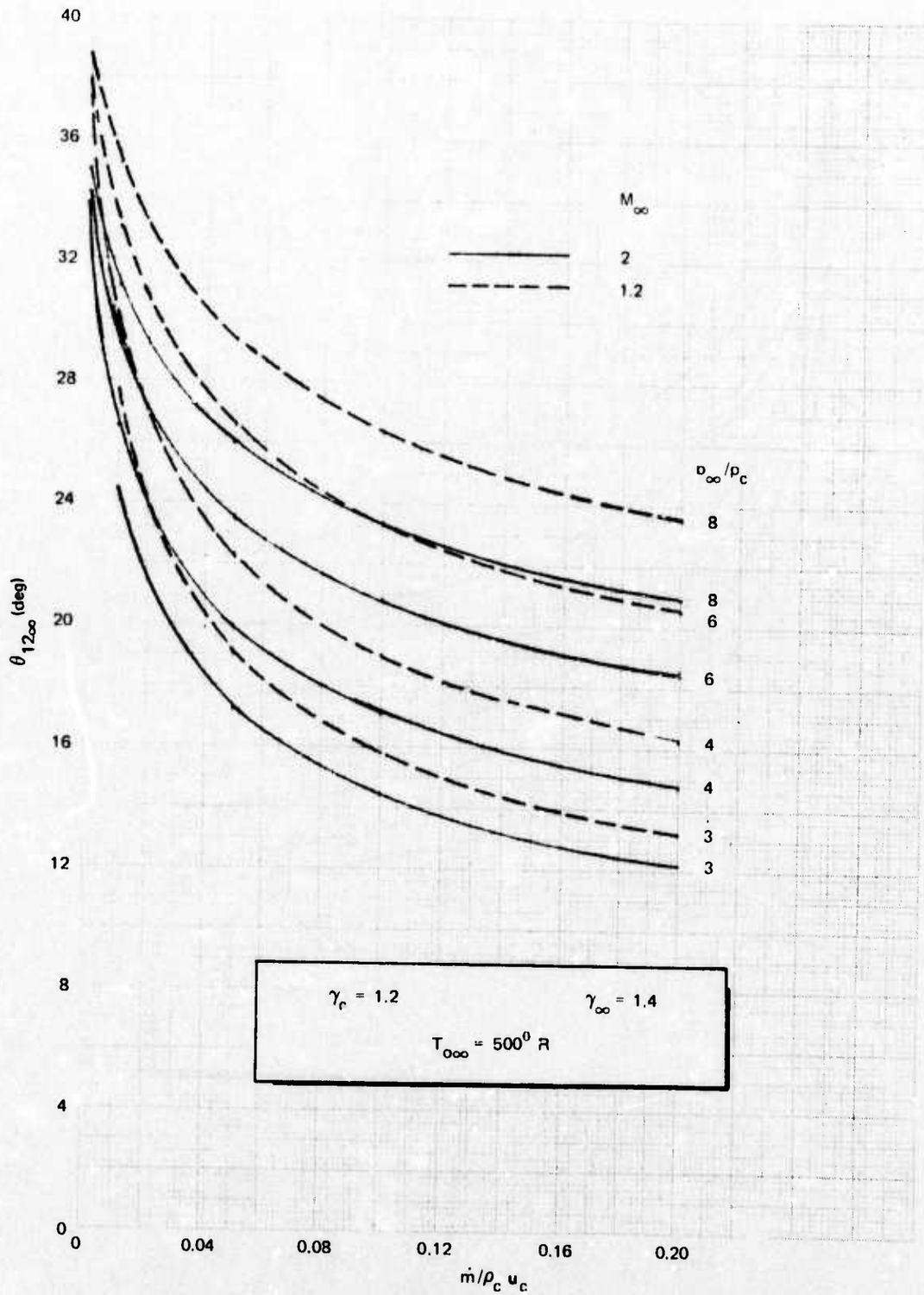

FIG. 75. $\theta_{12\infty}$ Versus $\dot{m}/\rho_c u_c$ for $M_c = 4$ With $T_{0c} = 3{,}000^0$ R.

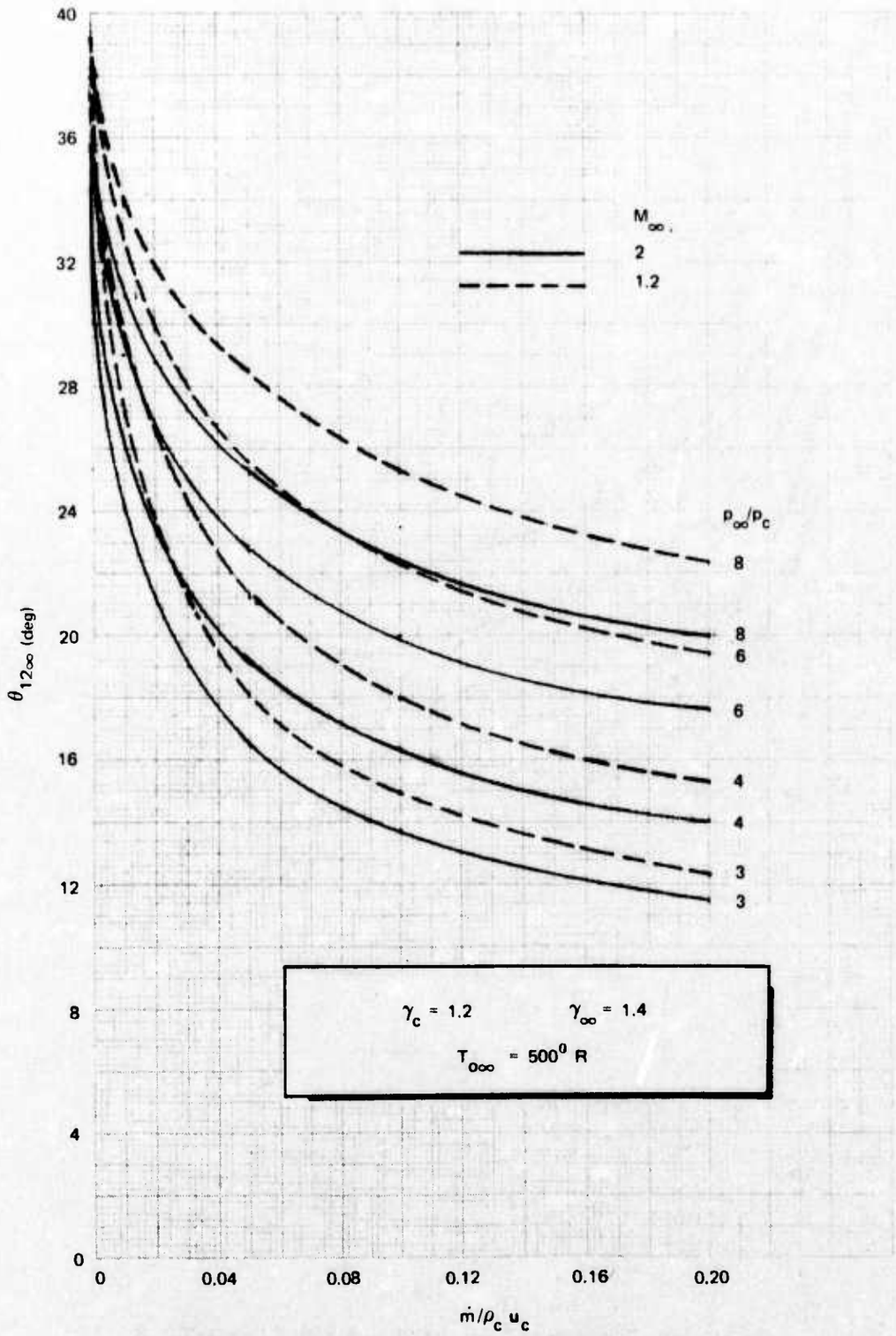

FIG. 76. $\theta_{12\infty}$ Versus $\dot{m}/\rho_c u_c$ for M_c = 4.5 With T_{0c} = 4.5.

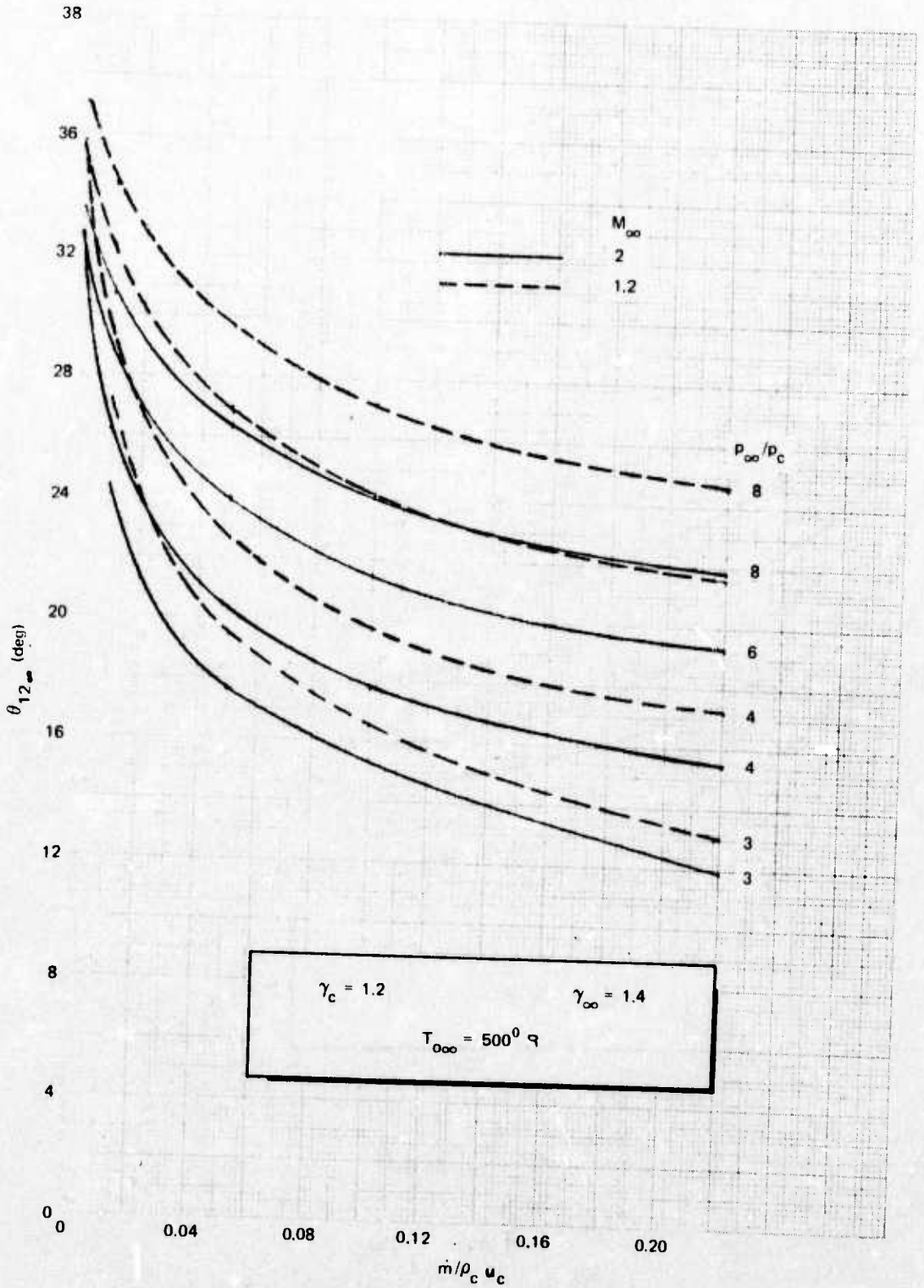

FIG. 77. $\theta_{12\infty}$ Versus $\dot{m}/\rho_c u_c$ for M_c = 3.5 With T_{oc} = 4,000° R.

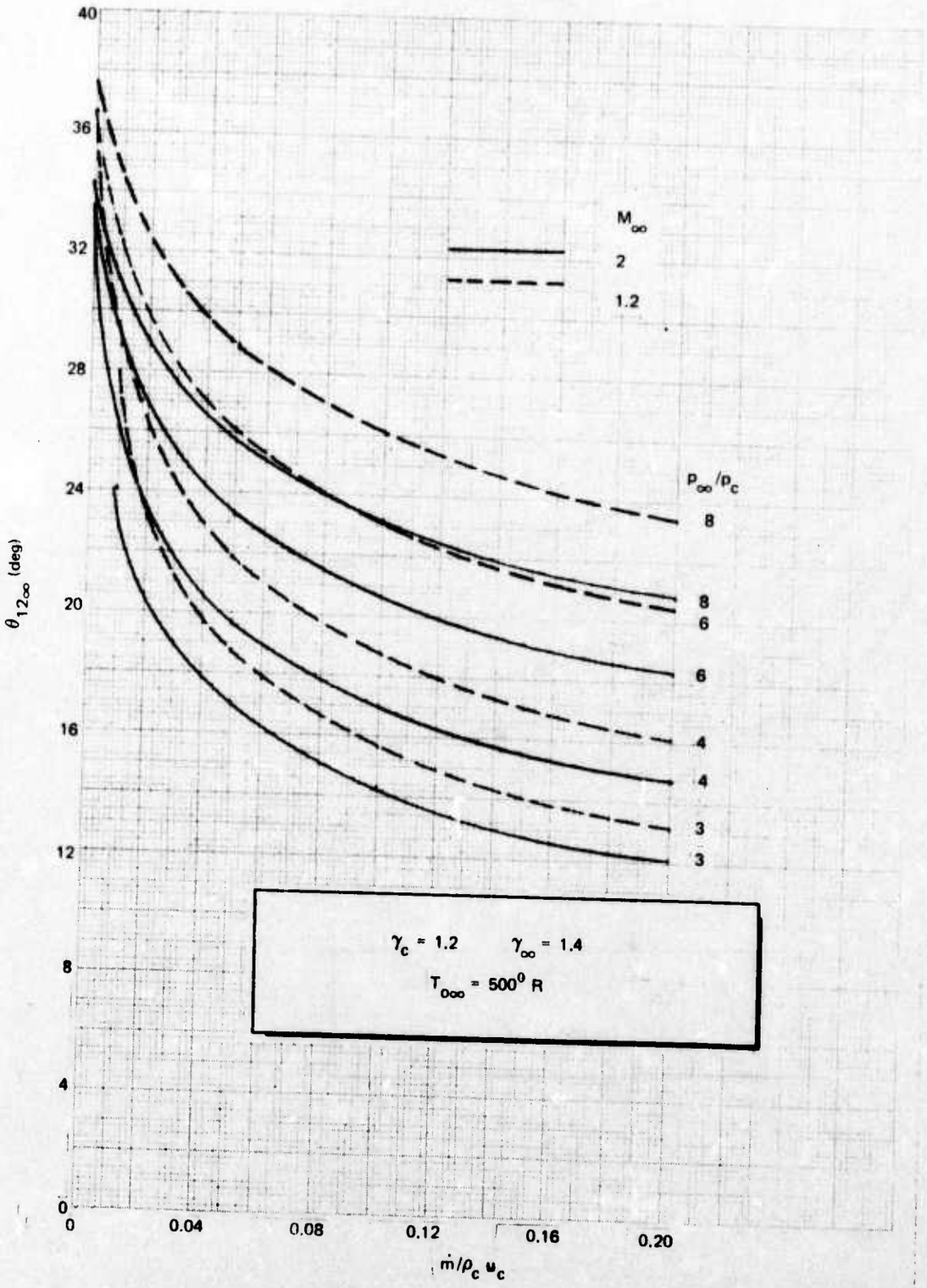

FIG. 78. $\theta_{12\infty}$ Versus $\dot{m}/\rho_c u_c$ for M_c = 4 With T_{oc} = 4,000° R.

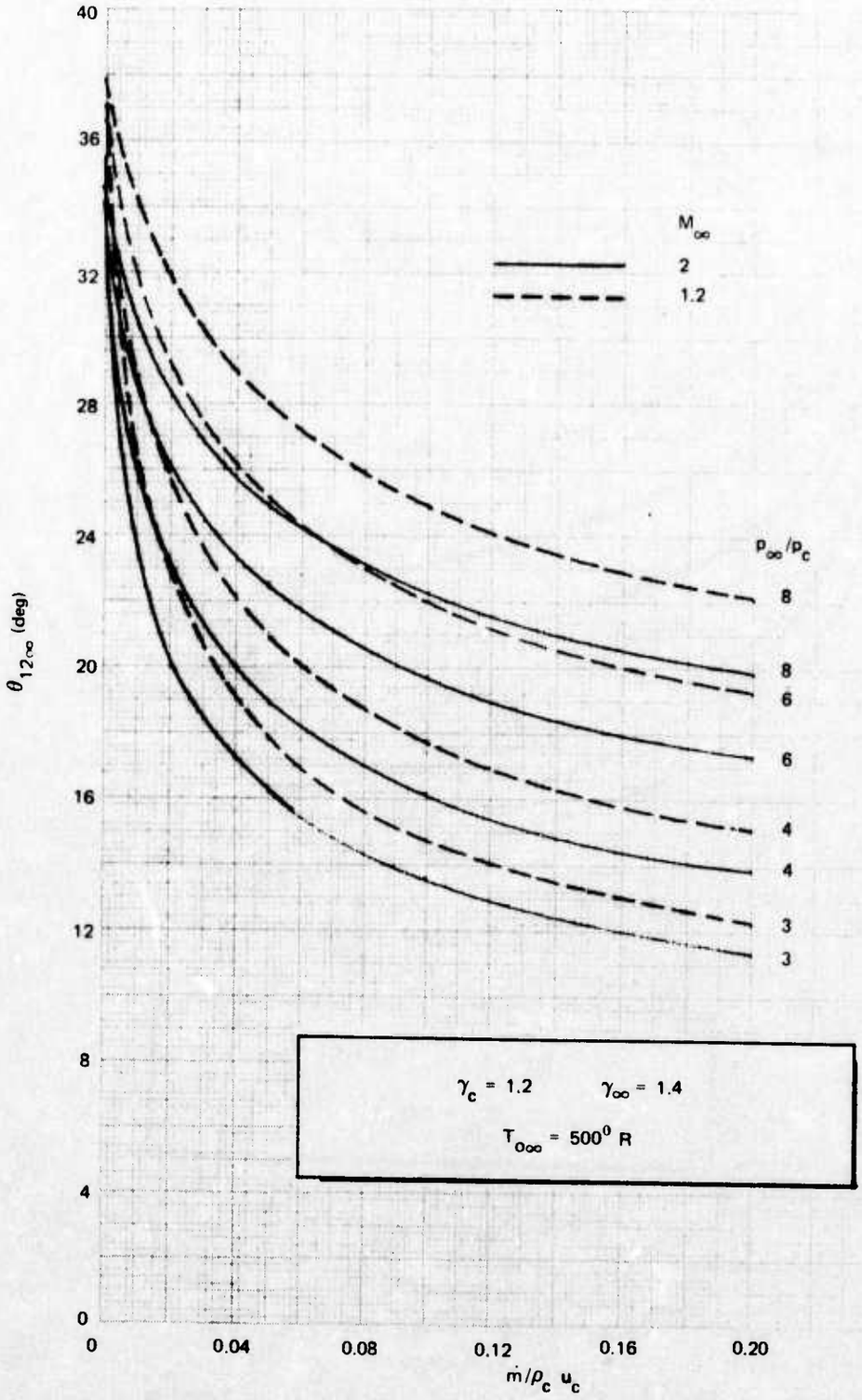

FIG. 79. $\theta_{12\infty}$ Versus $\dot{m}/\rho_c\ u_c$ for M_c = 4.5 With T_{oc} = 4,000° R.

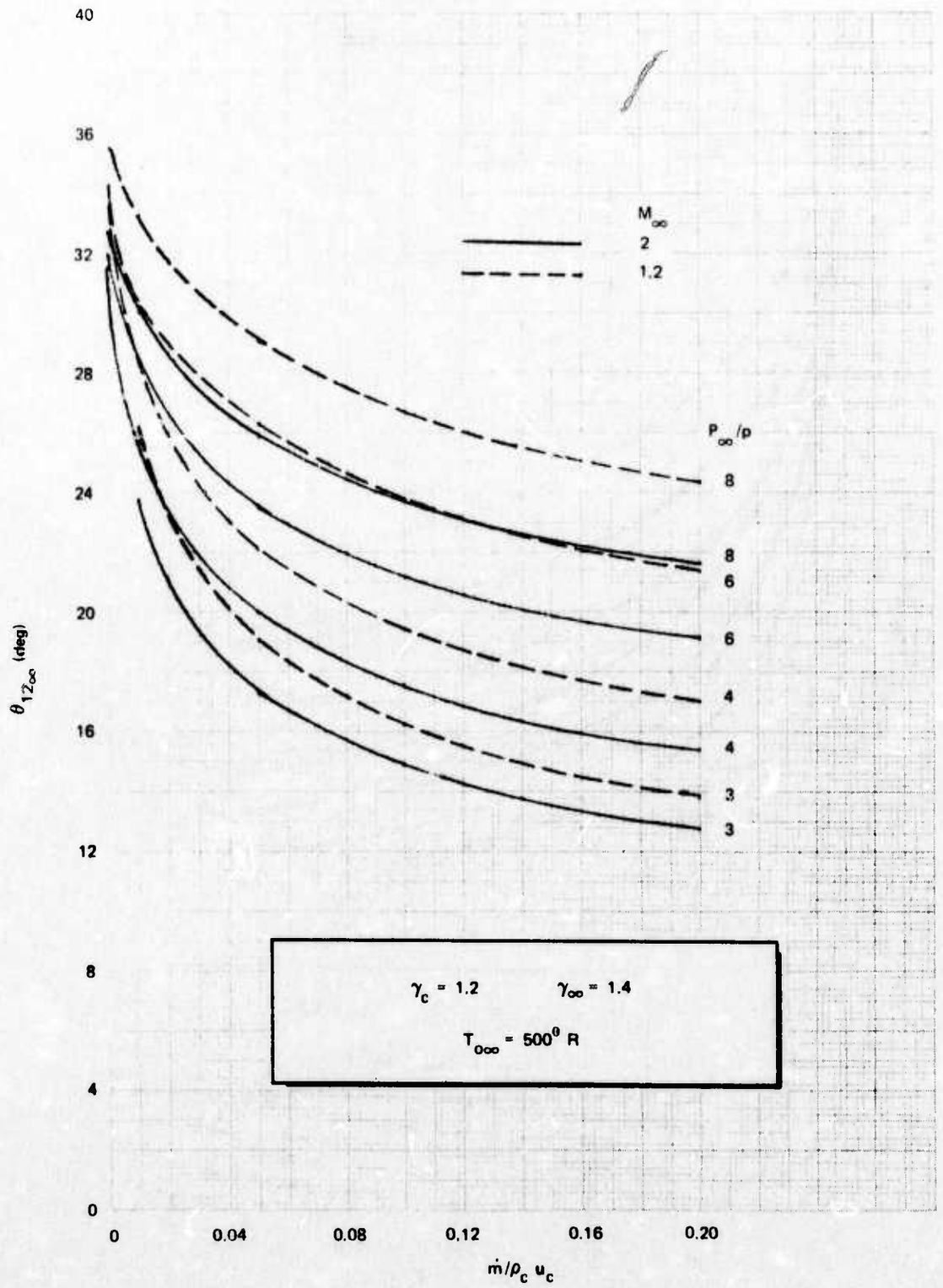

FIG. 80. θ_{12_∞} Versus $\dot{m}/\rho_c u_c$ for M_c = 3.5 With T_{0c} = 5,500° R.

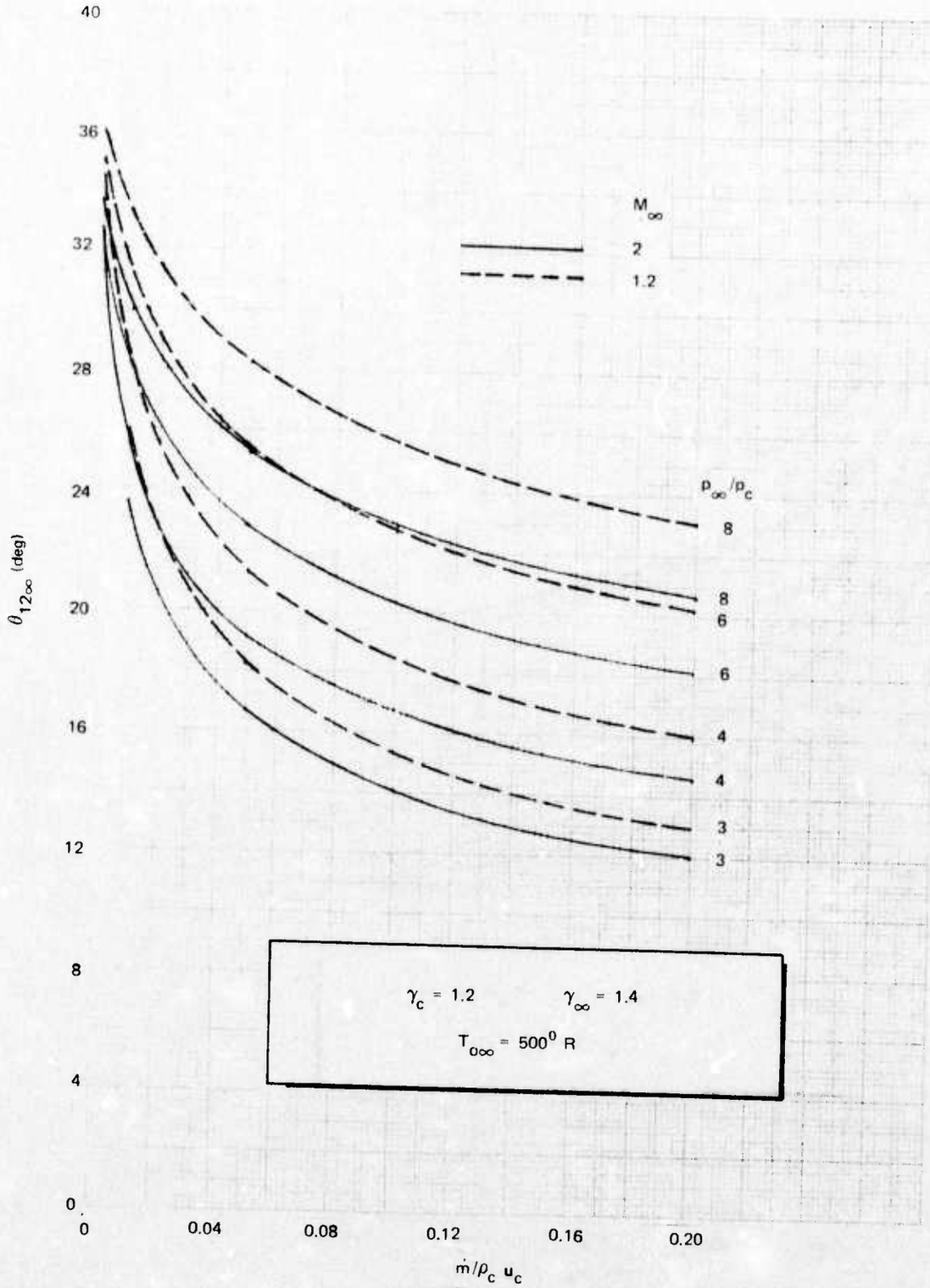

FIG. 81. θ_{12_∞} Versus $\dot{m}/\rho_c u_c$ for $M_c = 4$ With $T_{oc} = 5{,}500^0$ R.

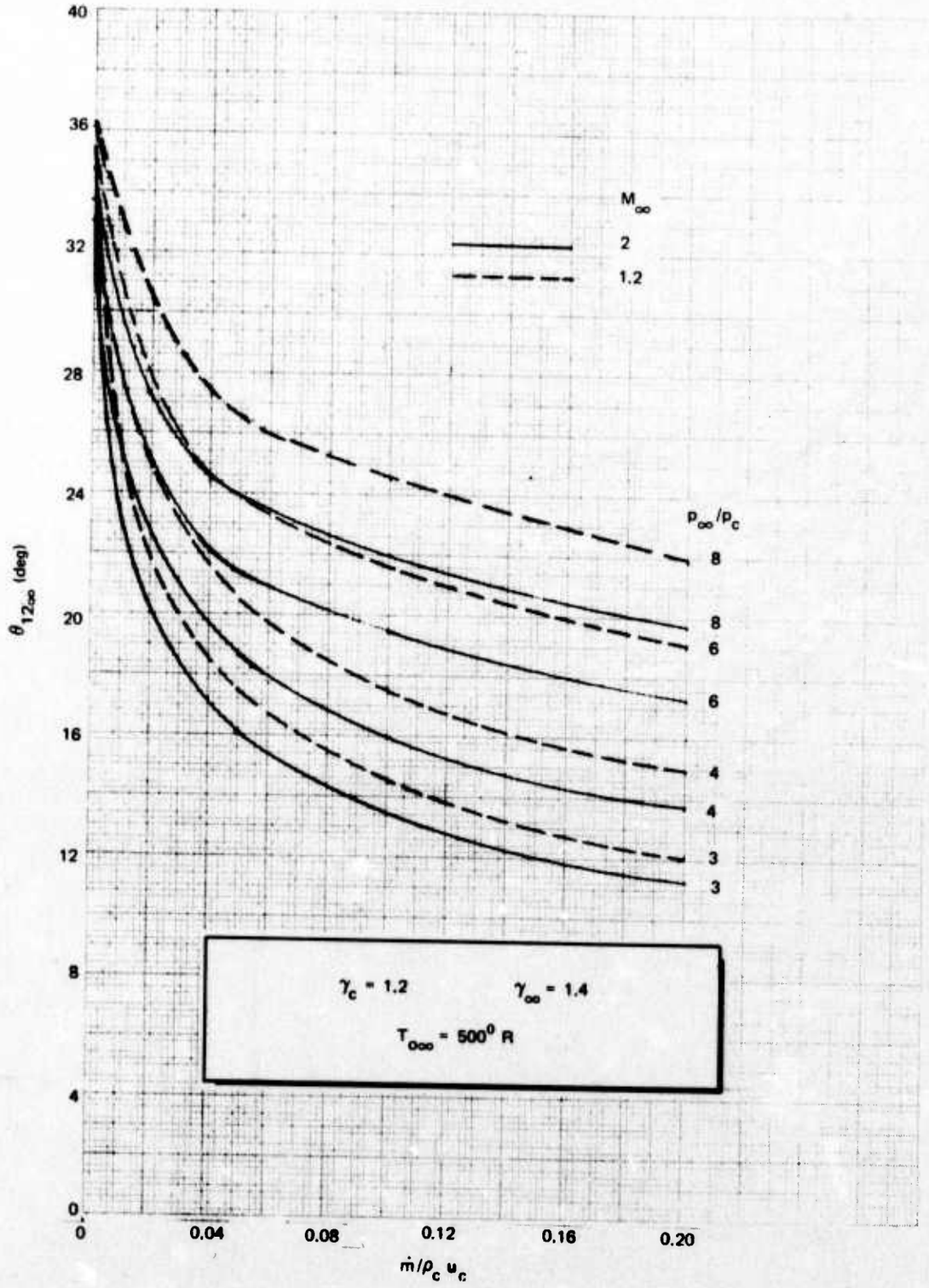

FIG. 82. θ_{12_∞} Versus $\dot{m}/\rho_c u_c$ for M_c = 4.5 With T_{0c} = 5,900° R.

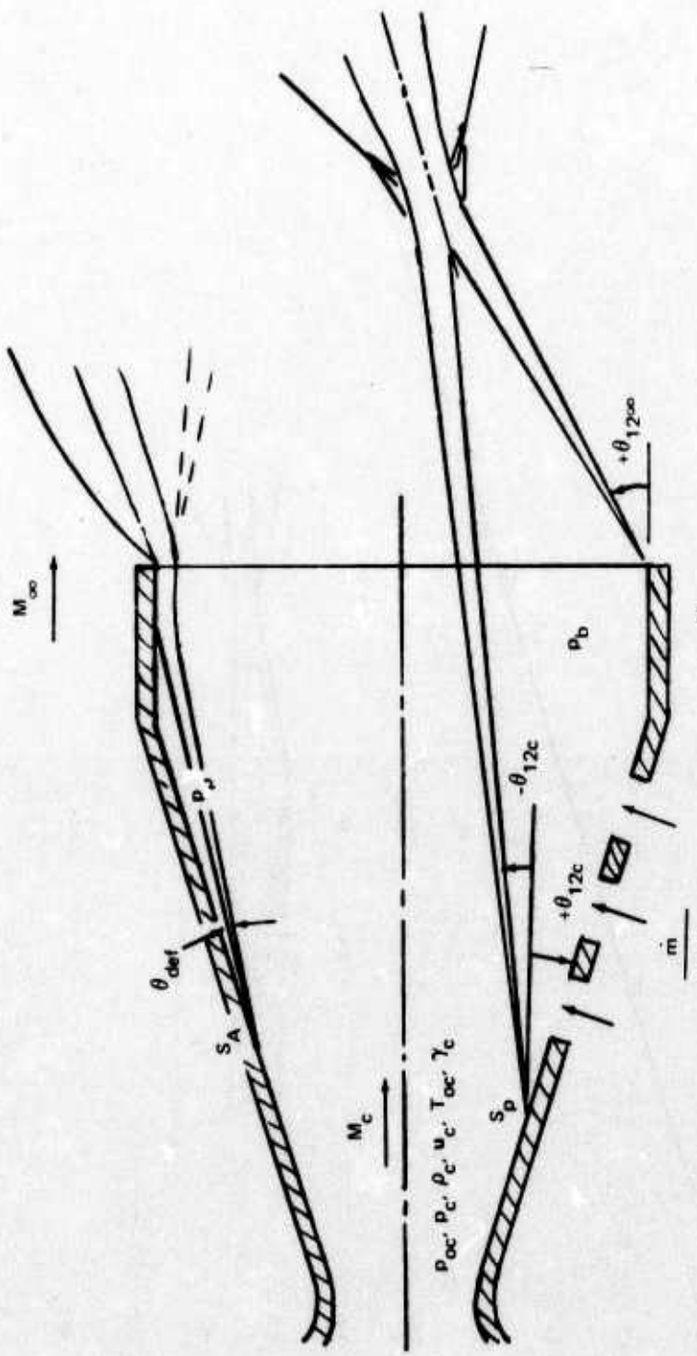

FIG. 83. BLTVC Flow Model With Ambient Flow.

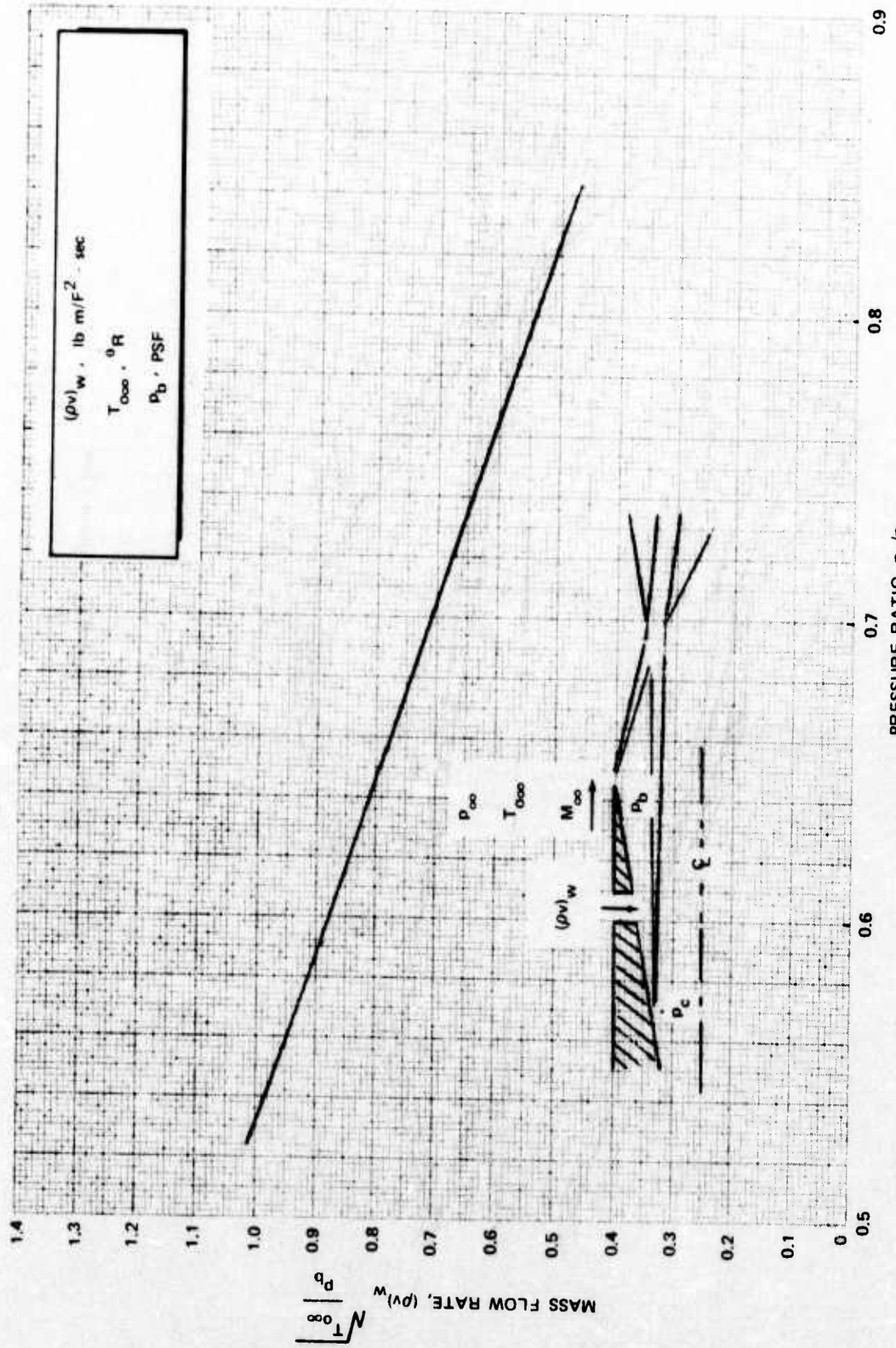

FIG. 84. TVC Mass Flow Rate Versus P_b/P_∞.

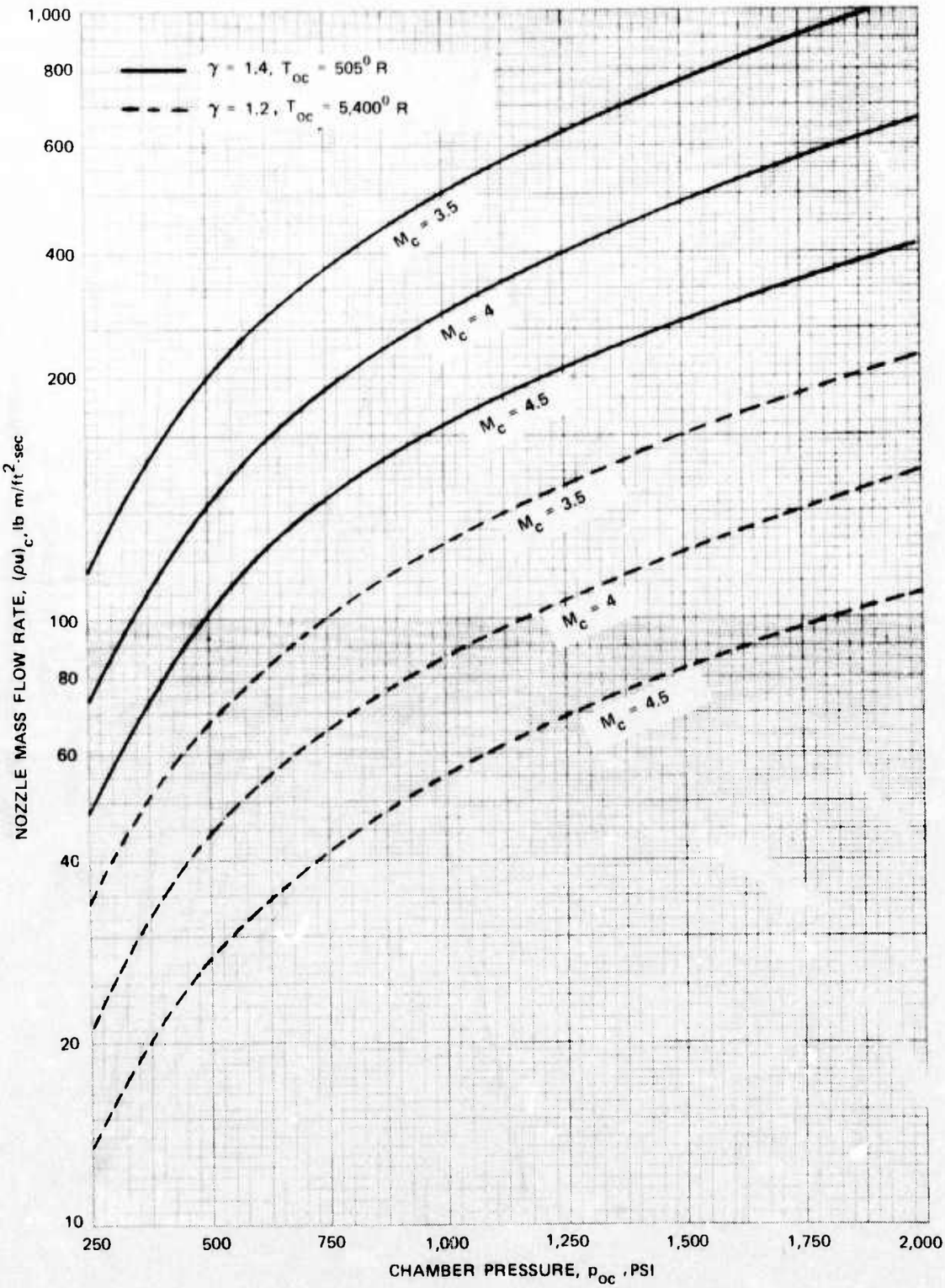

FIG. 85. Nozzle Mass Flow Rate Versus Chamber Pressure.

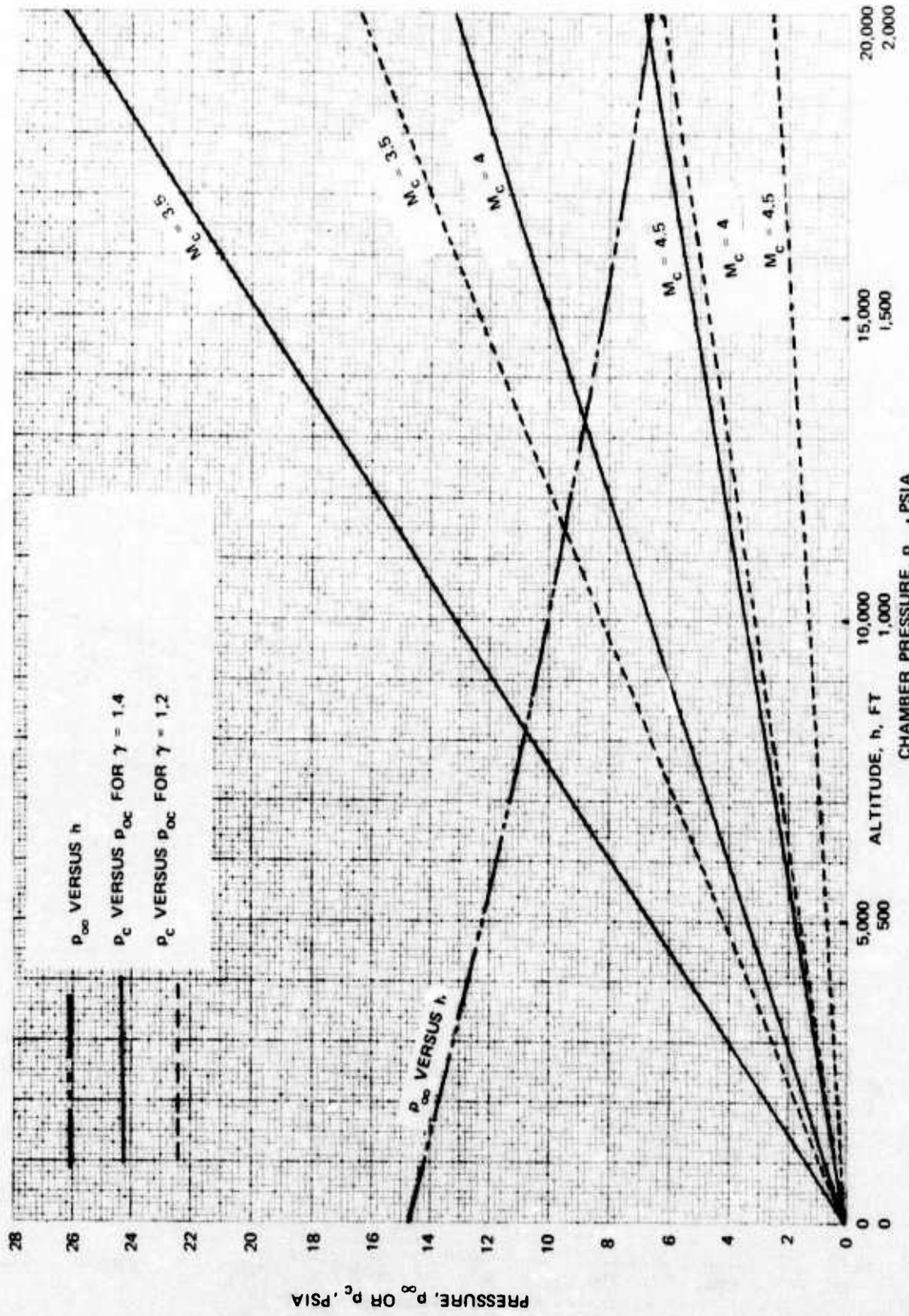

FIG. 86. Ambient and Nozzle Pressure Variations.

REFERENCES

1. Kampe, R. F. Low Cost Reaction Steering Device, Engineering Report R-781-1, Chandler Evans, Inc., January 1975.
2. Kampe, R. F., and R. E. Fitzgerald. Boundary Layer Control of Missile Thrust Vector (U), Report R-617, Chandler Evans, Inc., 4 May 1972 (Confidential).
3. Panzarella, Philip P. The Use of a Coanda Nozzle With Parallel Secondary Injection for the Thrust Vectoring of a Two-Dimensional Compressible Fluid. Thesis GAM 65A/ME/65-7, USAF Institute of Technology (AD 618025), March 1965.
4. Moore, E. F. The Use of a Coanda-Effect Nozzle for Multi-Directional Control of a Compressible Fluid Jet. Thesis GAM/ME/67-14 (AD 818403), USAF Institute of Technology, June 1967.
5. Baird, James. An Experimental Study of the Magnitude and Direction of Lateral Thrust Developed by a Three-Dimensional Coanda Nozzle. Thesis GAM/ME/69-1 (AD 851930), USAF Institute of Technology, March 1969.
6. Erdos, J. and A. Pallone. "Shock-Boundary Layer Interaction and Flow Separation," Proceedings of the 1962 Heat Transfer and Fluid Mechanics Institute, pp. 239-254.
7. Kalt, S. and D. L. Badal. "Conical Rocket Nozzle Performance Under Flow-Separated Conditions," Journal of Spacecraft, May-June 1965.
8. Thompson, R. V. Theoretical Determination of the Point of Separation in a Compressible, Turbulent, Supersonic Boundary Layer Subjected to an Adverse Pressure Gradient, ASME Paper 67-WA/FE-38, August 1967.
9. Kampe, R. F. Boundary Layer Control of Missile Thrust Vector, Report R-535-4, Chandler Evans, Inc., March 1971.
10. Kutateladze, S. S. and A. I. Leont'ev. Turbulent Boundary Layers in Compressible Gases, translated by D. B. Spalding, Academic Press, 1964.
11. Owczarek, J. A. Fundamentals of Gas Dynamics, International Text Book Co., 1964.
12. Chapman, D. R. Laminar Mixing of a Compressible Fluid, NACA Report 958, 1950.

13. Korst, H. H. "A Theory for Base Pressure in Transonic and Supersonic Flow," Journal of Applied Mechanics, Vol. 23, 1956, pp. 593-600.

14. Tang, H. H., C. P. Gardiner, and J. W. Barnes, Jr. Jet Mixing Theory Extensions and Applications in Separated Flow Problems, Report DAC-59181, Douglas Aircraft Company, Inc., February 1967.

15. Hill, W. G., Jr. and R. H. Page. "Initial Development of Turbulent Compressible Free Shear Layers," Journal of Basic Engineering, March 1969, pp. 67-73.

16. Tang, H. H., and J. W. Barnes. "A Combining Parameter for Base Pressure Evaluation," AIAA Journal, September 1967.

17. Korst, H. H., R. H. Page, and M. E. Childs. A Theory for Base Pressures in Transonic Flow, Report ME-TN-392-2, University of Illinois Engineering Experimental Station, March 1955.

18. Zumwalt, G. W. Analytical and Experimental Study of the Axially-Symmetric Supersonic Base Pressure Problem, doctoral dissertation, University of Illinois, 1959.

19. Kampe, R. F. Low Cost Reaction Steering Device – Wall Static Pressure Data, Report R-781-5, Chandler Evans, Inc., 10 June 1975.

20. Kampe, R. F. Low Cost Reaction Steering Device – Reconvergence Section Tests, Report R-781-4, Chandler Evans, Inc., 10 May 1975.

INITIAL DISTRIBUTION

15 Naval Air Systems Command
- AIR-03B (1)
- AIR-03P2 (1)
- AIR-320 (1)
- AIR-340B (1)
- AIR-503 (1)
- AIR-510B (1)
- AIR-5108 (1)
- AIR-5109 (1)
- AIR-5203 (1)
- AIR-52032C (1)
- AIR-5312 (1)
- AIR-53232 (1)
- AIR-5332 (1)
- AIR-5351 (1)
- AIR-5366 (1)

4 Chief of Naval Material
- MAT-030 (1)
- MAT-032 (1)
- NSP-27 (1)
- NSP-2731 (1)

8 Naval Sea Systems Command
- SEA-03 (1)
- SEA-031 (1)
- SEA-033 (1)
- SEA-09B4 (4)
- SEA-6531 (1)

3 Marine Corps Development and Education Command, Quantico (Marine Corps Landing Force Development Center)

1 Air Test & Evaluation Squadron 5 (LT Karl Kail)

1 Naval Air Development Center, Johnsville (SEVN)

1 Naval Ammunition Depot, Hawthorne (Code 05, Robert Dempsey)

1 Naval Explosives Ordnance Disposal Facility, Indian Head

1 Naval Intelligence Support Center (OOXA, CDR Jack Darnell)

1 Naval Ordnance Station, Indian Head (Code FS, A. T. Camp)

1 Naval Undersea Center, San Diego (Code 133)

3 Naval Surface Weapons Center, White Oak
- Code 33, H. Heller (1)
- Code G. C. W. Bernard (1)
- Code GW (1)

1 Naval Intelligence Support Center Liaison Officer (LNN)

4 Army Armament Command (AMSAR-SF)

4 Picatinny Arsenal (AMD, Concepts Branch)

4 Air Force Systems Command, Andrews Air Force Base
- DL (1)
- DLPI (1)
- DLW (1)
- SDW (1)

2 Air Force Aero-Propulsion Laboratory, Wright-Patterson Air Force Base
RJA (1)
STINSO (1)
5 Air Force Armament Laboratory, Eglin Air Force Base
DLD (1)
DLI (1)
DLO (1)
DLQ (1)
DLM, CAPT Aden (1)
1 Air Force Rocket Propulsion Laboratory, Edwards Air Force Base (Code MKP)
1 Foreign Technology Division, Wright-Patterson Air Force Base (Code PDXA, James Woodard)
1 Wright-Patterson Air Force Base (Code XRHP)
1 Defense Advanced Research Projects Agency, Arlington
2 Defense Documentation Center
1 Purdue University, School of Mechanical Engineering, Lafayette, Ind. (Cecil F. Warner)
101 Chemical Propulsion Mailing List No. 271 dated October 1975, including Categories 1,2,3,4,5

NWC 1364 805 (4/76) 200